PyroMEMS: Improved Fabrication Methods and Ignition Reliability

THÈSE N^{O} 5421 (2012)

PRÉSENTÉE LE 27 JUILLET 2012

À LA FACULTÉ DES SCIENCES ET TECHNIQUES DE L'INGÉNIEUR
LABORATOIRE DE CAPTEURS, ACTUATEURS ET MICROSYSTÈMES
PROGRAMME DOCTORAL EN MICROSYSTÈMES ET MICROÉLECTRONIQUE

ÉCOLE POLYTECHNIQUE FÉDÉRALE DE LAUSANNE

POUR L'OBTENTION DU GRADE DE DOCTEUR ÈS SCIENCES

PAR

David DE KONINCK

acceptée sur proposition du jury:

Prof. H. Shea, président du jury
Prof. N. de Rooij, Dr D. Briand, directeurs de thèse
Dr G. Ardila Rodriguez, rapporteur
Dr P. Leyland, rapporteur
Prof. C. Rossi, rapporteur

ÉCOLE POLYTECHNIQUE
FÉDÉRALE DE LAUSANNE
Suisse
2012

Abstract

Generating large force/displacement actuators at the millimeter and sub-millimeter scales remains an important challenge for microsystems engineers. One promising solution is to integrate high-energy density solid propellant fuels in microsystems (pyroMEMS) to generate high-pressure, high-temperature combustion gases. However, integrating combustible materials within microsystems is non-trivial: solid propellant fuels are generally integrated manually into the device during back-end processing leading to large variability in the device performance.

The goal of this thesis was to improve pyroMEMS reliability and performance. Reliability is particularly important for single-use devices—such as pyroMEMS—that cannot be tested before use. This was accomplished by simplifying their fabrication process and developing experimentally-validated models to improve device performance.

First, a solid propellant fuel—and associated deposition technique—was specifically formulated for use in pyroMEMS devices. The fuel used was a mixture of potassium 4,6-dinitrobenzofuroxan (K-DNBF) and binder. The propellant combustion was modeled using a chemical equilibrium code and validated experimentally by measuring the *in situ* pressure and temperature inside a pyroMEMS test device. We recorded combustion temperatures of 1300 ± 160 °C and overpressures of up to 60 ± 5 bar. These results were in good agreement with the values obtained from simulations. This represents the first such measurements ever carried out in pyroMEMS devices.

Two complementary pyroMEMS igniters were developed in this thesis: a drop-coated bottom-side igniter and a top-side shadow-mask evaporated igniter. The bottom-side igniter concept was based on the peripheral heating and ignition of fuel droplets to obtain smooth, steady combustion without fuel peeling or ejection. The overall fabrication process was highly simplified and extremely robust—over 350 igniters were successfully fabricated and tested. An investigation of igniter performance based on substrate material, igniter layout, fuel binder content and input power was performed. Semi-analytical models were developed and successfully predicted the ignition behavior of the igniters.

The top-side pyroMEMS igniter was fabricated by direct deposition of a metal igniter on the fuel surface via offset shadow mask evaporation. In this way, reliable ignition was ensured

by the intimate thermal contact between the fuel and igniter. The ignition concept was successfully demonstrated on fuel drops and over top full fuel chambers without fuel degradation or ignition.

Lastly, pyroMEMS balloon actuators for use in automated drug delivery systems and microfluidic actuators were designed, fabricated and tested. A foil-level fabrication technique using low-cost polymer materials and additive fabrication techniques was developed. The fabrication was compatible with cleanroom-free processing, thus facilitating solid propellant fuel integration. Balloon actuators were successfully inflated yielding membranes displacements of between 5 and 7.5 mm (for an initial membrane diameter of 5 mm). A semi-analytical model was developed that successfully predicted the balloon displacement.

This work represents an important step in developing simple, large-scale fabrication techniques that minimize manual back-end processing in order to improve device reliability.

Keywords: MEMS, powerMEMS, pyroMEMS, solid propellant, ignition, combustion, balloon actuator.

Résumé

Générer de forces et/ou déplacements à l'échelle (sub)millimétrique constitue un défit important dans le domaine des Microsystèmes. Une solution prometteuse est d'intégrer un propergol solide avec le microsystème. Par la suite, l'initiation du combustible génèrera une grande densité d'énergie, utilisable pour l'actionnement du composant (pyroMEMS). Cependant l'intégration du combustible dans le microsystème est non-triviale : généralement il est manuellement intégré après la fabrication principale—en dehors de la salle blanche—entraînant ainsi une large variance sur les performances des composants.

La fiabilité est un facteur particulièrement important pour les composants à usage unique tels que les pyroMEMS, qui plus est, ne peuvent être testées avant utilisation. Durant cette thèse, d'une part, des procédés de fabrication simples pour les pyroMEMS ont été développés, d'autre part, des modèles de simulation ont été réalisés et expérimentalement validés afin d'améliorer les performances ainsi que la fiabilité des pyroMEMS.

Dans un premier temps, nous avons développé le procédé de fabrication du pyroMEMS : un propergol solid ainsi que la technique de déposition associée a été définie. Le propergol fut composé de 4,6-dinitrobenzofuroxane de potassium (K-DNBF) et d'un liant. Ensuite le processus de combustion a été modélisé en se basant sur un code d'équilibre chimique, avant d'être validé expérimentalement par les mesures *in situ* des pressions et températures au sein du composant. Nous avons mesurés des températures de combustions de 1300 ± 160 °C et des pressions maximums de 60 ± 5 bar. Ces résultats concordaient bien avec les valeurs de simulations. Ces derniers représentent les premières mesures de temperatures et de pressions réalisées dans des dispositifs pyroMEMS.

Par la suite, deux concepts d'initiation du combustible, complémentaires, ont été étudiés pour le pyroMEMS fabriqué. Un premier initiateur a été conçu de façon à initier le propergol par dessous. Ce concept est basée su le chauffage de la partie périphérique entraînant l'initiation des gouttes de combustibles et produisant une combustion lisse et régulière, sans délamination ni éjection du propergol. Ce procédé de fabrication a été simplifié et le rendement amélioré : plus de 350 initiateurs ont été fabriqués et testés. Une étude sur la performance de l'initiateur a été menée, basée sur le substrat utilisé, la géométrie de l'initiateur, la teneur en liant du combustible ainsi que la puissance d'alimentation. Des modèles semi-analytiques ont été développés et ont pu prédire le comportement de l'initiateur.

Un deuxième concept d'initiation a été étudié : celui-ci a été fabriqué en déposant directement le métal initiateur sur la surface du combustible à travers un masque. De cette manière, un allumage fiable est induit par le contact thermique intime entre le propergol et le métal. Les initiateurs ont été démontrés sur des gouttes mais aussi sur des chambres pleines de propergol sans aucune dégradation ni initiation involontaire.

Egalement, des ballons de propulsion ont été réalisés et testés. Ces derniers trouvent plusieurs applications dans le domaine des bioMEMS, par exemple pour la distribution automatique de drogue ou encore l'actionnement de composant microfluidiques. Les procédés de fabrication développés ont l'avantage d'être à moindre coût : ils ne nécessitent pas obligatoirement de salle blanche, ce qui facilite l'intégration du combustible solide. De plus, des feuilles de polymère sont utilisées comme substrat. Ces ballons d'actionnement ont été testés, leur gonflage a entrainé des déplacements de 5 à 7,5 mm (pour un diamètre de membrane initial de 5 mm). Un modèle semi-analytique a également été développé afin de prédire les déplacements du ballon.

Ce travail constitue un important pas dans le développement de procédés de fabrications des pyroMEMS à grandes échelles. Une attention particulière a été portée à l'utilisation de techniques de fabrications simples tout en minimisant le nombre d'étapes manuelles de transformation en aval pour augmenter la fiabilité des dispositifs pyroMEMS.

Mots clés : MEMS, powerMEMS, pyroMEMS, propergols solides, initiateurs, combustion, ballon d'actionnement.

Acknowledgements

I would like to thank my thesis director Prof. Nico de Rooij for having given me the chance to carry out my doctoral research at the Sensors, Actuators and Microsystems Laboratory. I also gratefully acknowledge my thesis co-supervisor, Dr. Danick Briand for his constant support and feedback throughout the last four years.

I would like to thank the EPFL Space Center for funding this research project and the National Science and Engineering Research Council of Canada (NSERC) for a post-graduate scholarship.

Fabrication of the many devices presented in this thesis was only possible thanks to the many talented and friendly people at the CSEM and EPFL cleanrooms. A special thank you to Edith Milotte, Stephane Ischer, Pierre-André Clerc, Sylviane Pochon, Sébastien Lani and Laurent Guillot. At the EPFL cleanroom, I would like to thank particularly Philippe Flückiger, Georges-André Racine, Guy-François Clerc, Cyrille Hibert and Jean-Baptiste Bureau for all their help. Also, a special thank you to Laurent Thierry for his huge help with the temperature measurements.

The last four years have been a real challenge and I have been able to persevere through it all thanks to the loving support of family and friends. In particular I would like to thank Paco, Çaglar, Andres, Chris, Fabio, Philip, Franz, Jason, Simon, Dara, Sara, Yexian, Giorgio for helping me see the bigger picture when I was feeling down. I would also like to thank everyone at SAMLAB for creating a fun and interesting work environment and a special thank you to Karine and Claudio for your patience and help.

Lastly, I want to thank my parents for their constant support and encouragement throughout this time: I can honestly say that it would not have been possible without you.

Of course, more than anyone, you filled my life with laughter and turned the dark times to light: thank you, Rokhaya, for everything...

Neuchâtel, 11 July 2012 D. d. K.

Contents

Abstract iii

Résumé v

Acknowledgements vii

1 Introduction 1
- 1.1 PyroMEMS . . . 1
  - 1.1.1 Challenges . . . 1
  - 1.1.2 Motivation . . . 2
- 1.2 Thesis Goals . . . 2
- 1.3 Thesis Structure . . . 3

2 State of the Art 5
- 2.1 PyroMEMS . . . 5
  - 2.1.1 Brief Timeline . . . 5
  - 2.1.2 PyroMEMS Device Architectures . . . 7
  - 2.1.3 Igniter Placement . . . 8
  - 2.1.4 Fuels . . . 10
- 2.2 Applications . . . 12

3 Fuel 13
- 3.1 Introduction . . . 13
- 3.2 K-DNBF Fuel Mixture . . . 14
  - 3.2.1 Ignition Temperature . . . 14
  - 3.2.2 Combustion Products . . . 15
  - 3.2.3 Fuel Deposition . . . 15
- 3.3 Modeling . . . 19
  - 3.3.1 ICT Code . . . 19
- 3.4 Experimental Validation . . . 21
  - 3.4.1 Temperature . . . 21
  - 3.4.2 Pressure . . . 24
- 3.5 Discussion . . . 27
  - 3.5.1 Fuel Selection and Deposition Method . . . 27

3.5.2 Experimental Validation . . . 28
3.6 Conclusion . . . 30

4 Bottom-side Igniters **31**
4.1 Introduction . . . 31
4.1.1 Igniter Concept . . . 31
4.1.2 Layouts . . . 32
4.2 Fabrication . . . 35
4.2.1 Igniters . . . 35
4.2.2 Chambers . . . 35
4.2.3 Fuel Deposition . . . 36
4.3 Theory . . . 36
4.3.1 Assumptions . . . 36
4.3.2 Meander Model . . . 37
4.3.3 Annular Model . . . 41
4.3.4 Hot Spot Model . . . 44
4.4 Experimental Methodology . . . 44
4.4.1 Experimental Setup . . . 44
4.4.2 Statistical Analysis . . . 46
4.5 Ignition Results . . . 47
4.5.1 Borosilicate Glass Substrate . . . 48
4.5.2 Polyimide Substrate . . . 56
4.5.3 Closed Chambers . . . 56
4.6 Combustion Results . . . 58
4.6.1 Meander and Annular Layouts: Peeling and Fuel Ejection . . . 58
4.6.2 Hot Spot Layout: Steady Combustion . . . 61
4.6.3 Closed Chambers . . . 64
4.7 Discussion . . . 64
4.7.1 Ignition . . . 64
4.7.2 Combustion . . . 66
4.7.3 Fuel/Igniter Alignment . . . 67
4.7.4 Summary . . . 68
4.8 Conclusion . . . 68

5 Top-side Igniters **71**
5.1 Introduction . . . 71
5.2 Concept and Fabrication . . . 72
5.2.1 Shadow Mask Layout . . . 72
5.2.2 Fuel . . . 73
5.2.3 Choice of Metal . . . 74
5.3 1^{st} Generation: Igniters on Fuel Drops . . . 75
5.3.1 Deposition Parameters . . . 75
5.3.2 Igniter Characterization . . . 76

5.3.3 Experimental Methodology . . . 79
5.3.4 Results . . . 79
5.4 2^{nd} Generation: Igniters on Full Chambers . . . 85
5.4.1 Igniter Design . . . 85
5.4.2 Igniter Characterization . . . 86
5.4.3 Results . . . 87
5.5 Discussion . . . 88
5.6 Conclusion . . . 90

6 PyroMEMS Balloon Actuator 93
6.1 Introduction . . . 93
6.2 Fabrication . . . 95
6.2.1 Igniters . . . 95
6.2.2 Combustion Chambers . . . 97
6.2.3 PDMS Membranes . . . 99
6.2.4 Lamination . . . 99
6.3 Characterization . . . 99
6.3.1 Inkjet-Printed Igniters . . . 99
6.4 Modeling . . . 103
6.4.1 Assumptions . . . 103
6.4.2 Modeling Strategy . . . 104
6.4.3 Membrane Stress Distribution . . . 104
6.4.4 Algorithm Implementation . . . 110
6.4.5 Modeling Results . . . 112
6.5 Results . . . 116
6.5.1 Experimental Setup . . . 116
6.5.2 Fuel Ignition and Combustion . . . 117
6.5.3 Balloon Inflation . . . 119
6.6 Discussion . . . 124
6.6.1 Igniters . . . 124
6.6.2 Epoxy Chambers . . . 124
6.6.3 PDMS Membranes . . . 125
6.6.4 Inflation Results . . . 125
6.6.5 Balloon Actuator Model . . . 127
6.7 Conclusion . . . 127

7 Conclusion 129
7.1 Summary . . . 129
7.2 Main Contributions . . . 130
7.3 Future Work . . . 131

A ICT Thermodynamics code: sample output 133

B Balloon Actuator MATLAB code **137**

C Bisection Algorithm **141**

Bibliography **148**

Curriculum Vitae **149**

List of Figures

2.1 Sketch of the first pyroMEMS device 5
2.2 Sketch of the suspended pyroMEMS igniter 6
2.3 Sketch of an out-of-plane pyroMEMS device 7
2.4 Sketch of an in-plane pyroMEMS device 8
2.5 Sketch of a bottom-side pyroMEMS igniter 9
2.6 Sketch of a top-side pyroMEMS igniter 10

3.1 K-DNBF chemical structure 14
3.2 K-DNBF combustion temperature 15
3.3 K-DNBF combustion products 16
3.4 Fuel mixture dispenser 16
3.5 K-DNBF grain size distributions 17
3.6 Fuel mass distribution 18
3.7 PyroMEMS temperature measurement setup 22
3.8 K-DNBF combustion temperature 24
3.9 PyroMEMS pressure measurement setup 26
3.10 K-DNBF combustion pressure 28

4.1 Meander igniter layout 33
4.2 Annular igniter layout 34
4.3 Hot spot igniter layout 34
4.4 Sketch of meander model based on a semi-infinite plane heater 38
4.5 Cross-section sketch of the meander igniter 39
4.6 Sketch of the annular model based on a semi-infinite line heater 41
4.7 Cross-section sketch of the annular igniter 43
4.8 Cross-section sketch of the hot spot model 45
4.9 Bottom-side igniter power profile 47
4.10 Meander igniter ignition results (glass substrate) 49
4.11 Meander residual vs. fuel mass (glass substrate) 50
4.12 Annular ignition results (glass substrate) 50
4.13 Annular residual vs. fuel mass (glass substrate) 52
4.14 Hot spot ignition results (glass substrate) 52
4.15 Hot spot residual vs. fuel mass (glass substrate) 54

4.16 Mean hot spot residual vs. binder mass fraction (glass substrate) 54
4.17 Iteration convergence for the thermal conductivity 55
4.18 Effect of substrate material on ignition delay time (Meander layout) 57
4.19 Effect of substrate material on ignition delay time (Hot spot layout) 57
4.20 Effect of encapsulation on ignition delay time (glass substrate, hot spot layout) 59
4.21 Pictures of fuel peeling (glass substrate, meander layout) 60
4.22 Pictures of stable combustion (glass substrate, meander layout) 60
4.23 Fuel peeling vs. input power and binder content (glass substrate, meander layout) 61
4.24 Pictures of hot spot layout ignition (glass substrate, $a = 90$ μm fit region) 62
4.25 Pictures of hot spot layout ignition (glass substrate, $a = 5$ μm fit region) 62
4.26 Burning rate vs. input power (hot spot layout) 63
4.27 Pictures of closed chamber combustion (glass substrate, hot spot layout) 64

5.1 Sketch of a shadow-mask evaporated top-side igniter 72
5.2 Sketch of offset shadow mask evaporation 73
5.3 Shadow mask evaporation jig 73
5.4 Fuel drop surface topography 74
5.5 Sketch of offset shadow mask under-evaporation 75
5.6 Photograph of shadow mask igniters (1^{st} gen.) 76
5.7 Shadow mask igniter topography (1^{st} gen.) 77
5.8 Distribution of shadow mask igniter resistances (1^{st} gen.) 78
5.9 Pictures of the Joule ignition regime (1^{st} gen.) 80
5.10 Pictures of the spark-induced ignition regime (1^{st} gen.) 81
5.11 Typical current and voltage ignition traces (1^{st} gen.) 82
5.12 Shadow mask ignition results (1500 nm, 1^{st} gen.) 82
5.13 Effect of fuel thickness on combustion failure (1500 nm, 1^{st} gen.) 83
5.14 Spark-induced ignition failure: no combustion (800 nm, 1^{st} gen.) 83
5.15 Spark-induced ignition failure: explosion (800 nm, 1^{st} gen.) 84
5.16 Igniter failure vs. initial resistance (800 nm, 1^{st} gen.) 84
5.17 Sketch of shadow mask igniter edge coverage problem 85
5.18 Shadow mask igniter line profiles (2^{nd} gen.) 86
5.19 Shadow mask igniter resistances (2^{nd} gen.) 87
5.20 Picture of a shadow mask igniter after combustion (2^{nd} gen.) 87
5.21 Pictures of failed shadow mask igniter combustion (2^{nd} gen) 88
5.22 Shadow mask igniter ignition results (2^{nd} gen.) 89

6.1 Sketch of pyroMEMS balloon actuator 94
6.2 Sketch of balloon actuator drug injection application 94
6.3 Picture of inkjet-printed and electroplated igniters on PET 96
6.4 Picture of an array of igniters with deposited fuel drops 98
6.5 Picture of SUEX chambers 98
6.6 Picture of a pyroMEMS balloon actuator 100
6.7 Picture of a 3-layer chamber pyroMEMS balloon actuator 100

6.8 Inkjet-printed igniter power dissipation with and without nickel plating 101
6.9 Nickel-plated igniter current density stress test 102
6.10 SEM of a failed nickel-plated igniter 103
6.11 Sketch of pyroMEMS balloon model 105
6.12 Sketch of spherical cap membrane geometry 106
6.13 Picture of deflected membrane fitted with a circle 108
6.14 Picture of deflected membrane fitted with an ellipse 109
6.15 Picture of deflected membrane without fit 109
6.16 Stress-Stretch curves with Yeoh model fits (PDMS and parylene-C coated PDMS) 110
6.17 Balloon height vs. chamber volume (model, 10 % binder) 115
6.18 Effect of combustion temperature on the amount of gas generated by the combustion and the adiabatic constant 115
6.19 Picture of experimental setup for pyroMEMS balloon actuator tests 117
6.20 Ignition power vs. time (20 % binder) 118
6.21 Pictures of smooth fuel combustion using the nickel-plated igniters (20 % binder) 118
6.22 SEM of nickel-plated igniter after fuel combustion 119
6.23 Pictures of successful balloon actuation 120
6.24 Pictures of balloon actuation with leaking membrane 120
6.25 Pictures of balloon actuation bursting membrane 121
6.26 Picture of PET substrate after fuel combustion (epoxy layer removed) 122
6.27 Effect of binder content on balloon inflation dynamics 122
6.28 Pictures of the effect of binder content on balloon actuator combustion 123
6.29 Balloon height vs. chamber height 124

List of Tables

1.1 Comparison of MEMS actuators as a function of energy density 1

2.1 List of fuel mixtures used in pyroMEMS devices 11

3.1 Fuel mass distribution descriptive statistics 18
3.2 Simulated combustion temperatures and pressures 20
3.3 Matrix of test device parameters (Temperature) 23
3.4 Matrix of test device parameters (Pressure) 26
3.5 Summary of the temperature and pressure experiments 28

4.1 Bottom-side igniter resistance values 35
4.2 Bottom-side igniter fuel masses 36
4.3 Bottom-side igniter parameter summary table 45
4.4 Bottom-side igniter input power range 46
4.5 Meander igniter regression analysis (glass substrate) 48
4.6 Annular igniter regression analysis (glass substrate, $a = 125$ μm) 51
4.7 Annular igniter regression analysis (glass substrate, $a = 25$ μm) 51
4.8 Hot spot igniter regression analysis (glass substrate, $a = 90$ μm) 53
4.9 Hot spot igniter regression analysis (glass substrate, $a = 5$ μm) 53
4.10 Estimated thermal properties of the fuel mixture 56
4.11 Summary of closed chamber results (glass substrate, hot spot igniter) 58
4.12 Effect of fuel mass on combustion quenching (Hot spot layout) 63
4.13 Comparison of bottom-side ignition behavior with literature 68

5.1 List of e-beam evaporation targets 74
5.2 Shadow mask igniter evaporation parameters (1^{st} gen.) 75
5.3 Shadow mask igniter resistance values (1^{st} gen.) 79
5.4 Summary of the shadow mask ignition and combustion results (1^{st} gen.) 80
5.5 Comparison of the shadow mask igniter performance with the literature 90

6.1 List of inkjet printing process parameters 97
6.2 750 μm-thick SUEX combustion chamber process flow 98
6.3 Yeoh model fit parameters (PDMS and parylene-C coated PDMS) 109
6.4 Summary of the balloon actuator design parameters 112

6.5 Balloon actuator model sensitivity analysis (Maximum inflation) 113
6.6 Balloon actuator model sensitivity analysis (Room Temperature) 114
6.7 Summary of balloon inflation results 126
6.8 PyroMEMS balloon actuators: comparison with the literature 126

1 Introduction

1.1 PyroMEMS

Pyrotechnical microelectromechanical systems (pyroMEMS) are microsystems that incorporate solid propellant charges as functional materials. They have gained interest recently as simple low-cost sources of on-chip thermal energy and/or pressurized gas. A basic pyroMEMS device is composed of a combustion chamber, a fuel charge and an ignition source. The vast majority of pyroMEMS igniters are resistive heaters that ignite the fuel by heating it above its ignition temperature. Interest in pyroMEMS is due to the large energy densities stored inside solid propellant materials compared to the smaller energy densities that are achievable with existing MEMS actuators (see table 1.1). Even with poor energy conversion efficiencies, pyroMEMS actuators promise to deliver high force actuation at small scales.

Table 1.1: Comparison of MEMS actuators as a function of energy density [1].

Actuation Mechanism	Energy Density (J/m^3)
Piezoelectric (PZT)	10^5
Electrostatic	10^3
Electromagnetic	10^5
Thermomechanical	$\sim 10^5$
Thermopneumatic	10^6
Shape Memory Alloys	10^7
Phase Change (solid-liquid)	10^6 (acetimine)
	10^7 (paraffin wax)
Solid propellants	$10^7 - 10^8$

1.1.1 Challenges

Integration of combustible materials in microsystems is far from trivial. Solid propellants are not generally permitted in cleanroom environments, which complicates their fabrication process and places severe restrictions on the device layout. For most pyroMEMS devices, the

fuel is added after the main fabrication process—during the back-end processing outside the cleanroom (e.g., [2, 3]). As such, process variability is relatively large for existing pyroMEMS devices.

Furthermore, many solid propellant fuels themselves are not compatible with ignition and combustion in millimeter or sub-millimeter scale pyroMEMS devices. Ignition failure and combustion quenching due to tight confinement (thermal losses) are common problems faced in pyroMEMS devices [4–9]. Many groups have attempted to circumvent the quenching issue by making use of high explosives—such as zirconium potassium perchlorate (ZPP)—however, these materials are highly sensitive, making them difficult to handle and deposit in to the pyroMEMS [5]. Furthermore, combustion of ZPP generates mostly hot particles rather than large amounts of gas, making it ill-suited for pyroMEMS applications. Therefore, there exist a need to develop a solid propellant fuel that can easily be integrated with pyroMEMS devices. One strategy is to fabricate nanoenergetic materials in the cleanroom directly on the pyroMEMS devices [10]. However, their performances and stability still do not match those of "traditional" energetic materials. Recently, a consortium consisting of SAMLAB and RUAG Ammotec developed a fuel mixture that demonstrated reliable ignition at small scales [11].

1.1.2 Motivation

This project was initiated by the EPFL Space Center as a collaboration between the Sensors, Actuators and Microsystems Laboratory (SAMLAB) and the Laboratory of Computational Engineering (LIN). The initial aim of the project was to develop analytical and numerical modeling tools to predict the behavior of pyroMEMS devices, including micro-thrusters and micro-actuators. These models were to be validated experimentally by measuring the temperature, pressure and force generated by the combustion of solid propellants in pyroMEMS devices. Due to the single-use nature of pyroMEMS devices, proper validation of the models requires a large number of devices with similar performance levels. Unfortunately, pyroMEMS fabrication methods are not particularly reliable, as such, a major effort was undertaken to increase the reliability of pyroMEMS in order carry out these property measurements.

The starting point for this work was a previous joint SAMLAB/RUAG GmbH pyroMEMS project, in which a solid propellant fuel and its associated fuel deposition method were developed specifically for pyroMEMS applications (see chapter 3). As such, these two elements remained fixed throughout this work.

1.2 Thesis Goals

The single overarching theme of this work was to develop tools improve the reliability of pyroMEMS devices. This was accomplished in two ways:

1. *Improved fabrication methodology.* As mentioned above, the main problem with py-

roMEMS devices today is that their design and fabrication process are complex and require extensive manual back-end processing—primarily due to fuel deposition prior to complete device assembly. Simplifying the fabrication process will greatly improve the reliability and performance of pyroMEMS devices. Three different strategies were developed to achieve this goal:

- A drop-coated bottom-side pyroMEMS igniter was developed that was simple to fabricate and highly reliable.
- Top-side igniters were fabricated by direct deposition of the metal igniter on the solid fuel via offset shadow mask evaporation. By integrating the fuel into the fabrication process—rather than adding in at the end—the overall fabrication process was greatly simplified.
- A cleanroom-free (compatible) fabrication process was demonstrated to produce pyroMEMS balloon actuators. In this way, cleanroom compatibility issues with the fuel were avoided altogether. The process leveraged low-cost polymer materials, additive fabrication techniques—such as inkjet printing and electrodeposition—and assembled using foil-level lamination.

2. *Experimentally-validated pyroMEMS models.* We developed experimentally-validated semi-analytical predictive models of the ignition and combustion of solid propellants at small scales. The predictive models served as benchmarks with which the reliability and performance of our devices was compared.

1.3 Thesis Structure

After a short review of the pyroMEMS literature (chapter 2), the main goals of the thesis will be presented. Then, the mixture fuel used in this work will be presented in chapter 3. The deposition method will be explained and validated. The fuel decomposition was modeled using a chemical equilibrium code to extract the combustion products thermodynamic state after constant volume combustion. The extracted values of pressure and temperature for the combustion products were validated experimentally *in situ* using microfabricated temperature and pressure sensors.

In chapter 4, a simple and reliable drop-coated, bottom-side ignition concept will be presented that successfully mitigated the onset of fuel peeling and ejection. An in-depth study of fuel ignition and combustion characteristics of the igniter was carried out by varying the igniter layout, substrate material, fuel mixture composition, input power. The experimental results were modeled using semi-analytical thermal models of the igniter.

In chapter 5, a top-side igniter concept is demonstrated based on direct deposition of a metal igniter on the fuel mixture by offset shadow mask evaporation. A process-parameter study was carried out to improve the igniter fabrication yield.

Finally in chapter 6, a pyroMEMS balloon actuator was designed and fabricated using clean-room-free (compatible) processing with low-cost polymer materials. The metal igniters—the same bottom-side igniters demonstrated in chapter 4—were fabricated using inkjet-printing and electroplating on plastic foils and the combustion chambers were made using a photodefinable thick epoxy dry film. A semi-analytical model—leveraging the chemical equilibrium code presented in chapter 3—was constructed to predict the membrane deflection as a function of device geometry and fuel loading. Inflation tests were carried out using a high-speed camera to capture the balloon dynamics.

2 State of the Art

2.1 PyroMEMS

2.1.1 Brief Timeline

The first pyroMEMS devices were developed in the mid-90s by the CNRS-LAAS for use as an on-chip gas generator for transdermal drug delivery applications [12]. The device consisted of a micromachined polysilicon igniter fabricated on a suspended membrane to reduce thermal losses (see figure 2.1). The fuel was an energetic mixture containing the energetic binder glycidyl azide polymer (GAP) [13] that was deposited on top of the igniter by screen-printing and ignited by passing a current through the igniter.

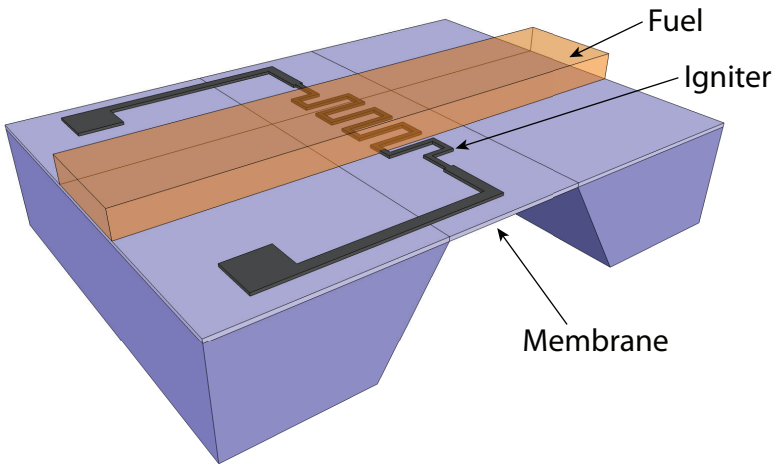

Figure 2.1: Sketch of the first CNRS-LAAS pyroMEMS device.

Shortly afterwards, a collaboration between TRW, The Aerospace Corporation and Caltech started developing so-called “digital micropropulsion”—basically arrays of pyroMEMS thrusters [14]. The devices consisted of three layers: a bottom silicon igniter layer, a middle glass cham-

ber filled with fuel and a top silicon layer containing burst diaphrams (i.e., figure 2.3). The different layers were assembled using cyanoacrylate. The fuel was ignited from the bottom and the high-pressure combustion products ruptured the burst diaphrams and imparted a thrust to the device.

In the early 2000s, the european project "Micropyros" was initiated to develop pyroMEMS thrusters for small satellites [2, 4, 15]. The team consisted of the CNRS-LAAS in France, SAM-LAB at EPFL—then part of the University of Neuchâtel—in Switzerland, IMTEK in Germany, ASTC in Sweden, SIC in Spain and the pyrotechnics company Etienne Lacroix in France. During this time, they developed what is considered the baseline architecture for pyroMEMS devices that served as inspiration to others [7, 16–18]—the different device architectures will be explained below. The devices consisted of the same suspended igniters developed at the CNRS-LAAS and a fuel filled chamber. Upon ignition of the fuel, the membrane would burst releasing the expanding combustion products.

Following on that work, the group of Dr. D. Briand first developed surface micromachined igniters suspended over a bulk wafer, rather than fabricated on a thin membrane (see figure 2.2) [16]. Afterwards, they began developing a new simplified igniter architecture based on drop-coated igniters—which served as the basis for the work presented in chapter 4 [11, 19].

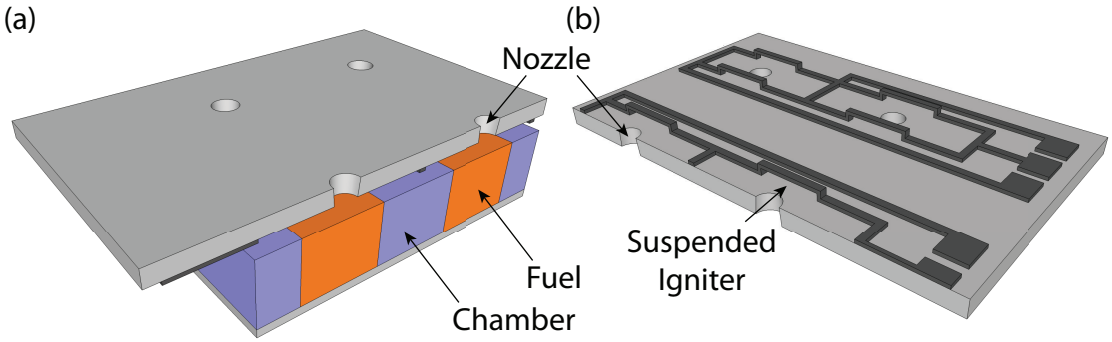

Figure 2.2: (a) Sketch of the suspended-igniter pyroMEMS device (top-side view). (b) Sketch of the suspended igniter (opposite side; without chamber and fuel).

Recently, work at the CNRS-LAAS has been focused on developing nanoenergetic materials specifically tailored for use in pyroMEMS devices [10]. They have also worked developed pyroMEMS safe, arm and fire devices for military ordinance [20–22] and pyroMEMS balloon actuators [23].

The main research groups working or having worked on pyroMEMS devices are the group of Dr. C. Rossi at the CNRS-LAAS in Toulouse [1, 2, 4, 5, 10, 12, 13, 15, 20–26], France, the group of Prof. S. K. Chou at NUS [3, 27–30] and the group of Dr. D. Briand at EPFL [2, 11, 15, 16, 19, 31–34]—part of the micropyros consortium. Recently, the group of Prof. S. Kwon at KAIST in South Korea have started developing pyroMEMS rockets for small satellites [17]. Other groups have

also contributed to the field of pyroMEMS, such as the TRW/Aerospace/Caltech consortium [14], the Honeywell/Princeton consortium [35], UC Berkeley [18], Tohoku University [7, 8], Kyushu University [6] and Georgia Tech [9].

2.1.2 PyroMEMS Device Architectures

There exist two different device architectures for pyroMEMS devices: out-of-plane and in-plane devices [2].

Out-of-Plane Device Architecture

In out-of-plane devices, each thruster component—the igniter, combustion chamber and nozzle—is fabricated separately and assembled together, one on top of the other, at the end (see figure 2.3). This allows high-density arrays of devices to be fabricated in parallel. This architecture is called "out-of-plane" because the combustion products are ejected vertically—perpendicular to the surface of the substrate. Most pyroMEMS devices are fabricated in this way.

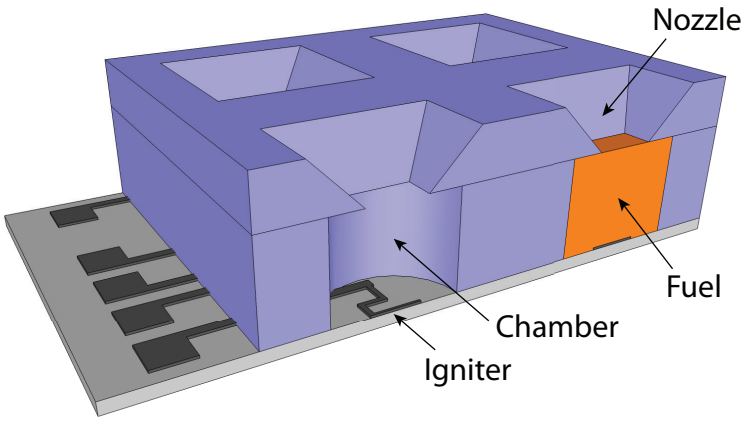

Figure 2.3: Sketch of an out-of-plane pyroMEMS device.

In-Plane Device Architecture

Alternatively, for the "in-plane" pyroMEMS architecture—developed by NUS—the different components are fabricated in the plane of the substrate (see figure 2.4). This allows much more flexibility in the size of the combustion chamber as well as the shape of the nozzle. In addition, the igniter fabrication is greatly simplified. However, fabricating high-density arrays is more difficult. Using their method, the complete thruster structure is fabricated at the wafer scale in a cleanroom environment—no manual epoxy gluing of components is required.

However, by sealing the combustion chambers before incorporating the fuel, the fuel needed to be inserted through the nozzle—an opening measuring only 400 μm × 500 μm. Chaalane *et al.* avoided this problem by integrating the fuel pellet manually before sealing the chamber with epoxy glue [26]. Both methods have their advantages and drawbacks.

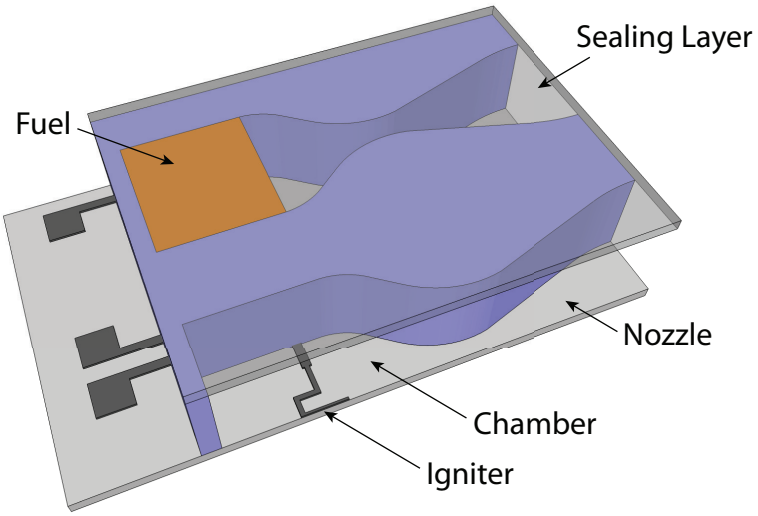

Figure 2.4: Sketch of an in-plane pyroMEMS device.

2.1.3 Igniter Placement

There are two different igniter architectures that are used in pyroMEMS: bottom-side or top-side igniters. The location of the igniter vis-à-vis the fuel charge and the nozzle is important in order to achieve steady, complete combustion of the fuel.

Bottom-side Igniters

Historically, bottom-side igniters were used in the first pyroMEMS devices [13, 14, 35] as they are simple to fabricate and assemble, and give good fuel/igniter contact; however, igniting the fuel on a buried surface—from underneath the fuel charge—will cause the unburned fuel to be ejected from the device (see figure 2.5). As such, the device performances were rather poor—Lewis Jr. *et al.* [14] reported only ~ 10 % of the fuel produced thrust.

Recently, the group of Dr. Briand revisited the bottom-side igniter architecture. They developed bottom-side igniters coupled with fuel drops, where the drops are ignited along their periphery to prevent fuel ejection [11, 19]. In this way, complete fuel combustion was obtained while leveraging the simplified fabrication methodology enabled using the bottom-side igniter geometry. This is the strategy followed for the igniters presented in chapter 4.

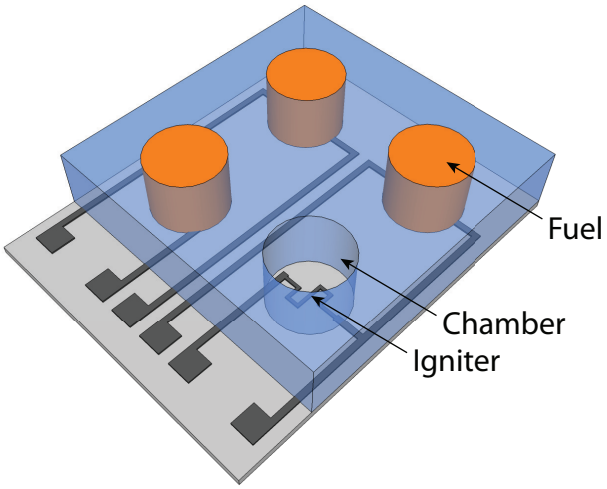

Figure 2.5: Sketch of a bottom-side pyroMEMS igniter.

Top-side Igniters

Top-side pyroMEMS igniters—originally developed during the micropyros project—attempted to alleviate this fuel-ejection problem by placing the igniters on top of the fuel charge, thus yielding steady, top-down combustion. The group at CNRS-LAAS accomplished by this suspending their igniters on thin SiO_2/SiN_x membranes, filling the hollowed out backside with fuel—without damaging the membrane—and closing the fuel cavity with a blank sealing wafer (see figure 2.6) [2, 4, 5, 12, 15, 20, 21, 24, 25]. During ignition, the membrane would burst under the pressure, releasing the expanding combustion gases. They speculated that their repeatability problems stemmed from poor contact between the fuel and the igniter due to air bubbles trapped between the fuel and the igniter or premature bursting of the membranes causing the combustion reaction to quench [1, 15].

The group at KAIST is developing a variant of the membrane suspended igniters pioneered by CNRS-LAAS, using thick (35 μm) glass membranes rather than the thin ($\sim$ 1.5 μm) SiO_2/SiN_x membranes proposed by CNRS-LAAS [17]. This helped increase their structural integrity and prevent premature failure of the membranes.

Alternatively, Briand et al. developed a surface-micromachined polysilicon igniter that is suspended by $\sim$ 1 μm above the silicon wafer [16]. The suspended igniters surrounded a micromachined nozzle, which allowed the gases to escape.

Lastly, for the in-plane pyroMEMS devices developed at NUS, they placed the igniter on the sidewall near the top of the fuel chamber [3, 27–30]. However, their devices were sensitive to the exact height of the fuel charge—i.e., whether or not the fuel was in direct contact with the igniter. Due to the imprecision in the fuel deposition method and variations in the fuel grain, the ignition delay time varied considerably [28].

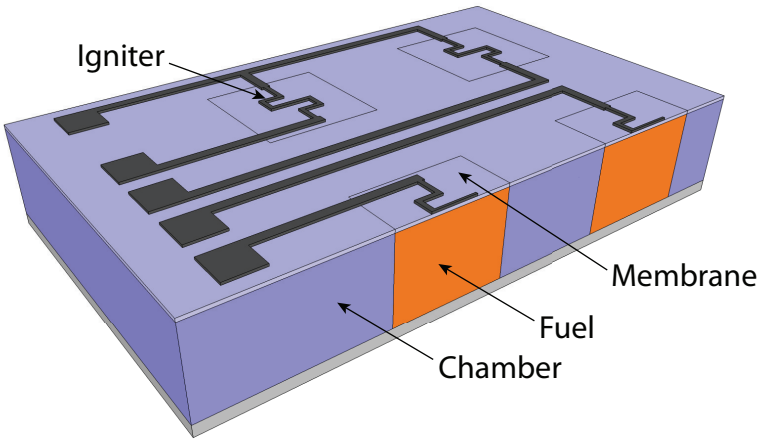

Figure 2.6: Sketch of a top-side pyroMEMS igniter.

2.1.4 Fuels

So-called "classical" solid propellant fuels—used in macroscale rockets—are generally composed four main ingredients:

- *Binder.* The binder is basically the glue that holds everything together. They are generally some sort of elastomeric polymer, such as hydroxyl-terminated polybutadiene (HTPB).
- *Oxidizer.* Solid propellant oxidizers are generally perchlorates or nitrates. The most commonly used solid oxidizer is ammonium perchlorate (AP), although ammonium nitrate (AN) is also used in lower temperature or gas generating applications.
- *Fuel.* Powdered metals are used as solid propellant fuels. The most common metal is aluminum, although boron and zirconium are also used.
- *Plasticizer.* Plasticizers are liquids that improve the physical properties of the fuel grain, increase the pot-life of the uncured mixture and reduce its viscosity to facilitate casting or extruding the solid propellant into its final shape.

In order to further increase the energy density of the fuel, energetic binders and plasticizers are commonly used. Alternatively, one can add solid explosives to the mixture, such as lead styphnate or zirconium potassium perchlorate (ZPP). Not all solid propellants contain all four main ingredients—i.e., powdered explosives, such as gun powder, are composed of a mixture of powdered fuel (sulfur and charcoal) and oxidizer (potassium nitrate), without any polymer binder or plasticizer.

A wide range of fuels have been tested in pyroMEMS devices by different groups (see table 2.1).

Table 2.1: List of fuel mixtures used in pyroMEMS devices.

Group	Fuel Mixture	Reference
CNRS-LAAS	Glycidyl Azide Polymer (GAP) / Zirconium / AP	[4]
	Zirconium / Potassium Perchlorate (ZPP)	
	Double-Base + Gun Powder	[26]
	(Mn-Co) Werner Complex	[23]
NUS	Gun Powder / Al / AP / Fe_2O_3 (Combustion catalyst)	[3]
SAMLAB (EPFL)	Potassium Dinitrobenzofuroxan / Adhesin®	This work
Caltech	Lead Styphnate	[14]
Princeton	Double-Base	[35]
	Lead Styphnate	
KAIST	Lead Styphnate	[17]
Kyushu University	HMX and RDX	[6]
Berkeley	HTPB / AP (with & without Al)	[18]
Tohoku	Boron / Potassium Nitrate	[7]
Georgia Tech	GAP / Al / AP / Graphite (to make it conductive)	[9]
U Cincinnati	Paraffin wax / H_2O_2 / MnO_2 (H_2O_2 Catalyst)	[36]

The group at CNRS-LAAS, in France, have mainly used 2 different fuels over the years. The first one was a mixture of the energetic binder glycidyl azide polymer (GAP), with ammonium perchlorate oxidizer and zirconium powder fuel. They had poor ignition success (at most 75 %) with this fuel without using a zirconium / potassium perchlorate (ZPP) ignition charge [15, 20]. ZPP is highly sensitive—therefore increasing the success rate of the pyroMEMS devices—however, it is not well adapted to pyroMEMS devices because it generates unsteady thrust curves as well as releasing hot oxidized zirconium particles that can damage nearby components [15]. Recently, they have been developing nanoenergetic materials specifically tailored for microsystems integration [10].

The collaboration between TRW, The Aerospace Corporation and Caltech, and the group at KAIST used lead styphnate for their “digital micropropulsion” devices. Lead styphnate is a solid explosive commonly used as an initiator for less sensitive secondary explosives. It is a highly energetic material that can sustain combustion even under very tight confinement; however, it is not well adapted for pyroMEMS devices due to its high toxicity. The collaboration between Honeywell and Princeton used a two-stage fueling solution: they made use of a small ignition charge of lead styphnate in order to ignite a less sensitive mixture of nitrocellulose and nitroglycerine—commonly called a double-base propellant. Tohoku University also made use of a two-stage solution of lead thiocyanate / potassium chlorate initiator and a boron / potassium nitrate fuel. Again, the use of fuels with heavy metals such as lead is not ideal.

Teasdale et al. [18] at UC Berkeley made use of a standard propellant mixture of hydroxyl-terminated polybutadiene (HTPB) binder, ammonium perchlorate oxidizer and aluminum powder fuel. They evaluated the impact of the aluminum powder and found that it increased

the burn rate, but that the aluminum particles tended to clog the sub-millimeter nozzles and were ejected from the combustion chamber without fully burning.

The group from NUS used a mixture of gun powder, oxidizer, fuel and combustion catalyst—without any binder—to fuel their pyroMEMS thrusters. Using a powder-based fuel is not ideal because the fuel can easily move around inside the device and their resulting devices could only be used upright.

The group at Georgia Tech developed electrically conductive fuel mixtures by adding to it ~ 20 % graphite by volume. By making the mixture electrically conductive, the fuel itself became the igniter, thereby removing any problems with poor fuel/igniter contact.

2.2 Applications

PyroMEMS have been developed for a range of military and civilian applications. The most common application for pyroMEMS devices is micro-thrusters for small satellites [2–8, 11, 14–17, 19, 24–30, 33, 35]. The thrusters are intended to be used for stationkeeping and course correction for small satellites weighting less than 10 kg.

In addition, pyroMEMS gas generators have been proposed for various applications, such as balloon actuators and fluid ejectors [9, 12, 13, 23, 31, 34, 36–39]. A pyroMEMS balloon actuator is composed of a solid propellant charge and an igniter inside a microfabricated combustion chamber covered by an elastic membrane. Combustion of fuel generates high pressure gas that inflate the membrane to do work. For fluid actuators, the pyroMEMS outlet is attached to a microfluidic inlet port and the expanding combustion products directly push the fluid through the channels of the device [36].

Other applications include initiation and/or safing of pyrotechnics or military ordinance [20–22], gas generators for material synthesis [40, 41] and welding [42].

3 Fuel

3.1 Introduction

PyroMEMS present unique challenge for the efficient combustion of solid propellant fuels due to their small size—on the order of 1 mm^3:

1. *Quenching.* The large surface to volume ratio increases the thermal losses to the environment, which can lead to quenching of the combustion wave, therefore more energetic fuels—such as primary explosives—are commonly used in pyroMEMS.
2. *Particle size.* The particle size of the different fuel constituents play an important role in burning rate, fuel viscosity and explosion hazard:
    - *Burning rate.* Decreasing the particle size increases the burning rate of the fuel mixture by increasing the packing density and surface area for chemical reactions. Higher burning rates are key for pyroMEMS devices because of their small fuel chambers—since fuel burning outside the device does not do any work. High burning rates also help prevent quenching by injecting more thermal energy into the system at a faster rate than is lost to the environment.
    - *Viscosity.* Decreasing the particle size decreases the viscosity of the fuel mixture. A well adapted, automated, fuel deposition method is key to producing reliable pyroMEMS devices. In this work, the fuel was deposited into the small fuel chamber using a syringe, requiring relatively low viscosities.
    - *Explosion hazard.* Increased burning rates make the propellant inherently more hazardous and prone to inadvertent ignition. Increased burning rates can also lead to detonation, causing catastrophic failure and potential injuries. Safety requirements are a primary concern for pyroMEMS, as they are targeted for commercial applications, rather than military applications.

Based on the above requirements, the solid propellant used was a solid explosive powder mixed with a non-energetic binder.

3.2 K-DNBF Fuel Mixture

The solid propellant used in this work was a mixture of potassium salt of 4,6-dinitrobenzofuroxan (K-DNBF; provided by RUAG Ammotec GmbH) and a water-based binder (polyacrylate emulsion; Adhesin® by Henkel). Three different binder mass fractions were tested in this work: 5, 10 and 20 %. The uncured mixture was mixed with water (2 parts fuel mixture, 1 part water) for safe handling during fuel deposition. The water evaporated after deposition yielding a solid fuel mass.

K-DNBF is a crystalline solid explosive that decomposes directly from the solid phase (figure 3.1). It is a monopropellant that does not require an external oxidizer to react. K-DNBF is commonly used as a primary explosive and initiator in small arms munitions and airbags, and is a so-called "green propellant"—i.e., it does not contain heavy metals such as lead or barium [43]. It was chosen due to its commercial availability, relative safety and stability against unwanted ignition, high gas output after combustion (~ 810 cm^3/g) and low ignition temperature (~ 200 °C) [11].

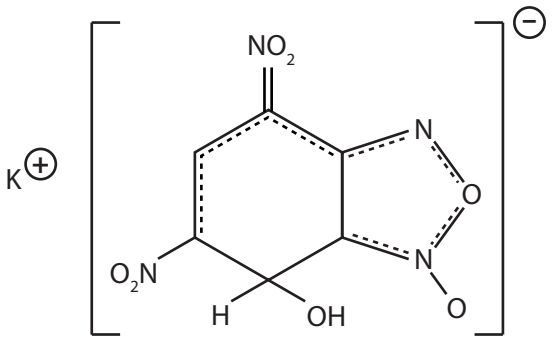

Figure 3.1: K-DNBF chemical structure.

Adhesin® was selected as the binder in the fuel mixture due to its chemical compatibility with the propellant, good thermal stability, high adhesion strength and handling ease [11]. In addition, using a water-soluble binder avoided the use of flammable solvents and reduced the danger of accidental explosion during fuel processing.

3.2.1 Ignition Temperature

The fuel ignition temperature was estimated using differential scanning calorimetry (DSC; figure 3.2). The measurements were carried out by the RUAG Ammotec GmbH. DSC functions by measuring the heat released by the sample under a constant heating rate. By convention, exothermic processes are negative on the y-axis. It is commonly used to determine temperature and enthalpies associated with phase transitions, crystallization and decomposition reactions. Both pure K-DNBF and K-DNBF mixed with 20 % binder were studied to determine the effect of the binder on the thermal sensitivity of the fuel. The "ignition temperature" was defined as the temperature at maximum heat release rate—i.e., the exothermic peak of the

DSC thermogram. Addition of binder to the solid explosive had a negligible effect on the ignition temperature, decreasing from ~ 206 °C to ~ 202 °C. Both the pure and 20 % binder mixture exhibited sharp peaks, with very little energy release below the ignition temperature. The magnitude of the heat flows measured were not representative or reproducible for two reasons: (1) the fuel mass was not only approximate, and (2) the sampling rate of the DSC was much slower than the chemical kinetics of the fuel mixture.

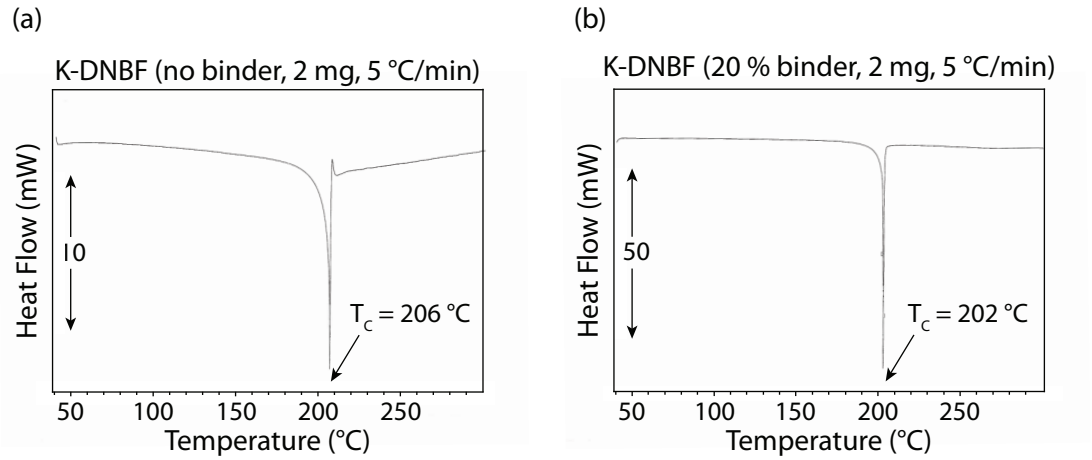

Figure 3.2: Differential scanning calorimeter measurements for (a) pure K-DNBF and (b) K-DNBF mixed with 20 % binder mass fraction. The sample sizes and temperature ramp are indicated above each figure.

3.2.2 Combustion Products

The primary combustion product of the fuel mixture was carbon monoxide (see figure 3.3). Pure K-DNBF also produces small amounts of potassium cyanide (< 3 % mole fraction), which is highly toxic—as such, all experiments were conducted under a fume hood. In addition, incorporating large amounts of polymer binder significantly decreased the oxygen balance of the fuel mixture, thus generating a large amount of soot (solid carbon) at 20 % binder mass fractions.

3.2.3 Fuel Deposition

A reliable and repeatable fuel deposition system is crucial to the reliability of the associated pyroMEMS devices. If the mass of fuel in each device is not tightly controlled, the force generated by the propellant combustion will not be predictable. For the devices presented in this work, a manual liquid dispenser was used (LSD 9000 by Fishman Corporation; see figure 3.4). The fuel deposition was performed at RUAG Ammotec. A total of 3 deposition runs were carried out during this work. Each run consisted of over 100 pyroMEMS devices.

In order to enable dispensing of the fuel paste, the viscosity—particle size—is important.

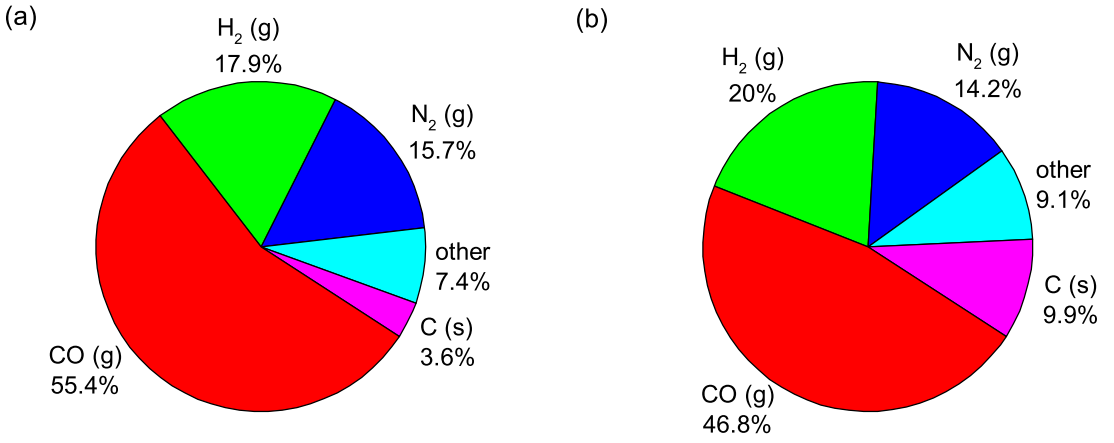

Figure 3.3: Principal fuel mixture products of combustion (ICT code simulations; constant volume combustion): (a) 10 % binder (b) 20 % binder.

Figure 3.4: Picture of the Fishman LDS9000 dispenser used for fuel deposition in the pyroMEMS devices.

The median crystal size of the standard K-DNBF produced by RUAG is ~ 100 μm (figure 3.5a), whereas paste dispensing required particle sizes on the order of 10 μm. As such, the production was changed from a one step synthesis to a two step process with Na-DNBF as an intermediate product. The modified synthesis yielded a smaller particle size distribution compatible with dispensing (figure 3.5b).

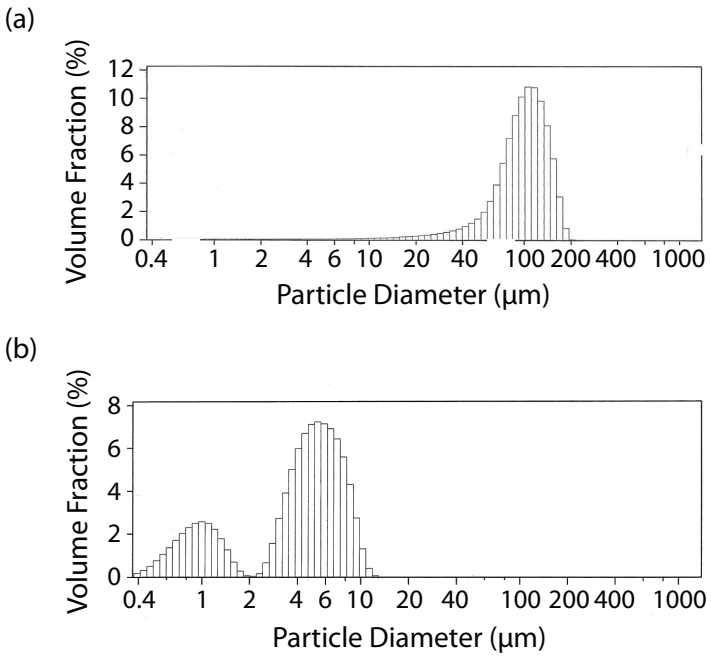

Figure 3.5: Particle size distributions for K-DNBF synthesized (a) using the standard RUAG method and (b) using a modified recipe to obtain smaller crystals [11].

Fuel Mass

The fuel drop mass was determined by weighing the chips with a microbalance (Mettler-Toledo XP56) before and after the combustion experiments, and taking the difference between the two. The microbalance had a precision of 1 μg. Fuel mass distributions for the 2^{nd} deposition run as a function of binder content are shown in fIgure 3.6. A summary table containing the distribution statistics for the first and second fuel deposition runs are given in table 3.1—the fuel mass for the last run (used for the full chamber tests in chapter 5) were not measured.

For this run, a total of 160 pyroMEMS devices were weighed for each binder mass fraction mixture. The 10 % binder fuel drops were on average ~ 100 μg smaller than the 20 % binder drops—based on the distribution modes. This is believed to be due to the lower viscosity of the higher binder fuel mixtures. The fuel mass distributions were highly skewed to the right and leptokurtic, i.e., they have a large kurtosis—meaning there are relatively many outlying data points in the distribution compared with a standard normal distribution. The spread of the distributions was estimated by taking the middle 50 % of the fuel mass distribution—from

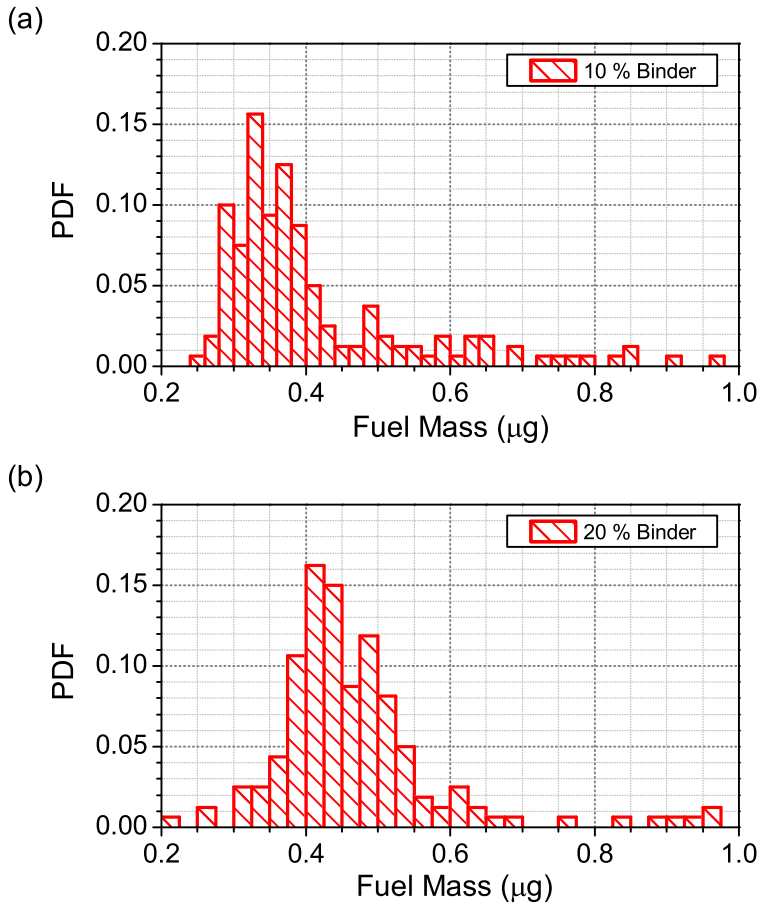

Figure 3.6: Fuel mass distribution for the (a) 10 % binder and (b) 20 % binder fuel drops.

Table 3.1: Fuel mass distribution descriptive statistics for different binder mass fractions.

		Distribution Quantiles (μg)						
Binder (%)	Mode (μg)	2.5 %	25 %	50 %	75 %	97.5 %	Skewness	Kurtosis
1^{st} deposition run								
5	65	24	52	128	200	428	0.96	2.97
10	60	20	59	104	164	454	1.94	7.03
20	104	31	103	149	252	542	1.53	5.01
2^{nd} deposition run								
10	312	279	325	365	435	843	1.79	5.85
20	418	314	404	447	504	920	2.26	9.94

the 25 % to 75 % quantiles. The spread for the 10 % and 20 % binder drops was 110 μg and 100 μg, respectively. The fuel masses obtained in the second run were roughly 4× larger than those in the first one, leading to some design problems in chapter 6.

Dispensing of paste-like materials in an repeatable, tightly-controlled manner is non-trivial. A large number of parameters can effect the distribution of drop masses, including plunger displacement and speed, hold time, and plunger retraction distance and speed. One of the main challenges with obtaining tightly controlled fuel mass distributions was that the fuel paste would slowly creep under the stress of the plugger, resulting in a sudden increase in the volume of fuel deposited. In addition, the water in the fuel mixture would slowly separate from the mixture over the course of the dispensing process—which lasted several hours—leading slow changes in mixture viscosity and deposited fuel mass. As such the deposition parameters had to be periodically adjusted in order to maintain a constant drop mass. However, an in-depth optimization study of the dispensing parameters was beyond the scope of this work.

3.3 Modeling

Predicting the final thermodynamic state of solid propellant combustion products is a difficult endeavor. Solid propellant mixtures are composed of large molecules with complex reaction mechanisms. In addition, the combustion products can exist in as solids, liquids or gases, depending on their temperature and pressure. Nevertheless, there exist chemical equilibrium codes used to predict the final state of solid propellant products undergoing constant volume or constant pressure combustion.

Chemical equilibrium calculations are of interest in this work for two reasons:

1. To evaluate the applicability of the codes to small scale devices, such as pyroMEMS;
2. To build models incorporating fuel combustion to predict the behavior of pyroMEMS devices. In particular, the chemical equilibrium code will be used to determine the parameters such as the combustion pressure, amount of gas generated and input into a semi-analytical model to predict the deflection of a pyroMEMS balloon actuator (see chapter 6).

3.3.1 ICT Code

In this work, we made use of a commercially-available chemical equilibrium code developed by the Fraunhofer Institute for Chemical Technology (ICT). The ICT Thermodynamic code (ICT code) was specifically designed for calculating the performance of rocket and gun propellants. It is the code used by our partners RUAG Ammotec GmbH, who manufacture the solid propellant fuel used in this work.

The code is based on solving the equations of conservation of mass—all the atoms in the

reactants must exist in the products—and the mass action expressions—related to the reaction rates—iteratively. The method was pioneered by the National Aeronautics and Space Administration (NASA). For more details on the method see [44–46]. It is capable of calculating the equilibrium thermodynamic state of the products for solid propellants undergoing constant volume or constant pressure combustion. It can also calculate the parameters for Chapman-Jouget detonation waves for gaseous reactants.

In practice, the ICT code requires the chemical formulae of the reactants, their densities and enthalpies of formation as inputs. In appendix A, we give a representative ICT code program output. Based on advice from RUAG Ammotec, the binder was simulated as acetylcellulose.

One potential problem with the ICT code is that the fuel mass used for computations is fixed at 1 g; therefore, the simulated chamber volume is made larger in order to obtain the same loading densities—ratio of fuel mass to chamber volume—as in the real pyroMEMS devices.

Simulated Combustion Temperature and pressure

Two output parameters of particular interest to us are the constant volume combustion temperature and pressure—as these are the parameters that will be measured experimentally to validate the simulations. The chemical equilibrium code assumes the combustion chamber is isolated from the environment—i.e., no heat losses. Two different sets of experiments were conducted to validate the ICT code. In the first, the combustion chamber temperature was measured inside 3 different chamber volumes—2.2, 4.4 and 6.6 mm^3—and using two different binder mass fractions—10 and 20 % (see below for details). The modeled combustion pressure and temperature for these 6 test devices are given in table 3.2. However, it is important to keep in mind that the fuel masses for the 10 and 20 % binder are not equal, but were chosen based on the fuel mass distributions for the 1^{st} deposition run given in table 3.1.

Table 3.2: Simulated combustion temperatures and pressures (1^{st} round, see text for details).

	Temperature (°C)		Pressure (bar)	
Chamber Height (μm)	10 % Binder	20 % Binder	10 % Binder	20 % Binder
525	1270 ± 40	1300 ± 40	230 ± 120	390 ± 170
1050	1230 ± 50	1240 ± 40	110 ± 60	180 ± 80
1575	1190 ± 30	1210 ± 40	70 ± 40	120 ± 50

The simulated combustion temperatures were between 1200 and 1300 °C. The ICT code predicted a drop in temperature with increasing chamber volume and with increasing binder content. The combustion pressures varied to a much larger extent than the combustion temperatures. Pressures between 70 and 390 bar were obtained—they decreased with increasing chamber volume, but increased with binder content. This is due to the larger fuel mass of the 20 % binder drops. For equal fuel masses, the combustion pressure of a 20 % binder fuel mixture was ~ 20 % lower than for the 10 % binder mixture. As we will show below, these high

pressures caused most of the combustion chambers to rupture.

3.4 Experimental Validation

The results obtained from the ICT code were validated experimentally by measuring the temperature and pressure during combustion inside pyroMEMS test structures. Thermodynamic property measurements inside pyroMEMS devices is challenging due to the short combustion times (~ 100 ms), the small amount of thermal energy released by the fuel (~ 1 J) and the small dimensions of the combustion chamber (~ 1 mm^3). The following sections describe the initial temperature and pressure results obtained to date.

3.4.1 Temperature

Introduction

In order to measure the combustion products temperature inside the pyroMEMS device, we require a temperature sensor with a fast response time and a small thermal mass. There exist two different categories of temperature transducers: contact and non-contact.

There are many types of contact sensors, such as thermocouples, resistance temperature detectors, thermistors, etc. Contact temperature sensors function by measuring their own temperature and assuming that they are in thermal equilibrium with the combustion gases. This becomes a serious limitation when the amount of thermal energy we wish to measure is very small, because the thermal mass of the sensor can completely change the final equilibrium temperature of the system. Alternatively, non-contact temperature sensors operate by measuring the radiated energy of the body at one or more wavelengths—generally in the infrared spectrum. For flame temperature measurements, the radiative body in question is generally incandescent soot formed during the combustion process. Based on the intensity of the radiation and the emissivity of the soot, the temperature can be calculated. Non-contact flame temperature measurements are expensive and difficult to carry out. Commercial off-the-shelf solutions are not readily available.

Choice of Temperature Sensors

Two different temperature transducers were used to measure the temperature inside the closed combustion chambers. The first was a platinum resistance temperature detector (RTD) that was co-fabricated with the bottom-side platinum igniters (figure 3.7b). RTDs infer temperature changes by measuring the resistance change in a resistor. RTDs are made using materials, like platinum, with a large and strongly linear temperature coefficient of resistance (TCR)—which represents the relative change in resistance with temperature. The RTD resistance was measured using a 4-wire method to eliminate the effect of the interconnects. The RTD was calibrated in an oven by measuring its resistance versus temperature.

The RTD was fabricated on a 500-μm thick glass substrate via a lift-off process and consisted of a 15-nm-Ta/235-nm-Pt film deposited via electron-beam evaporation (see chapter 4). The RTD used to measure the combustion temperature was located in the center of the ring-shaped igniter in order to measure the combustion temperature near the mid-point of the combustion process (see figure 3.7b, where the RTD is colored red). The RTD resistance at room temperature was $23.0 \pm 0.5\ \Omega$ and its TCR was 296.1 ppm/°C.

The advantages of the thin-film platinum RTDs are its ease of fabrication and direct integration with the pyroMEMS device. The major disadvantage of the RTD is that it is in direct thermal contact with the igniter substrate, which adds substantial thermal inertia to the sensor.

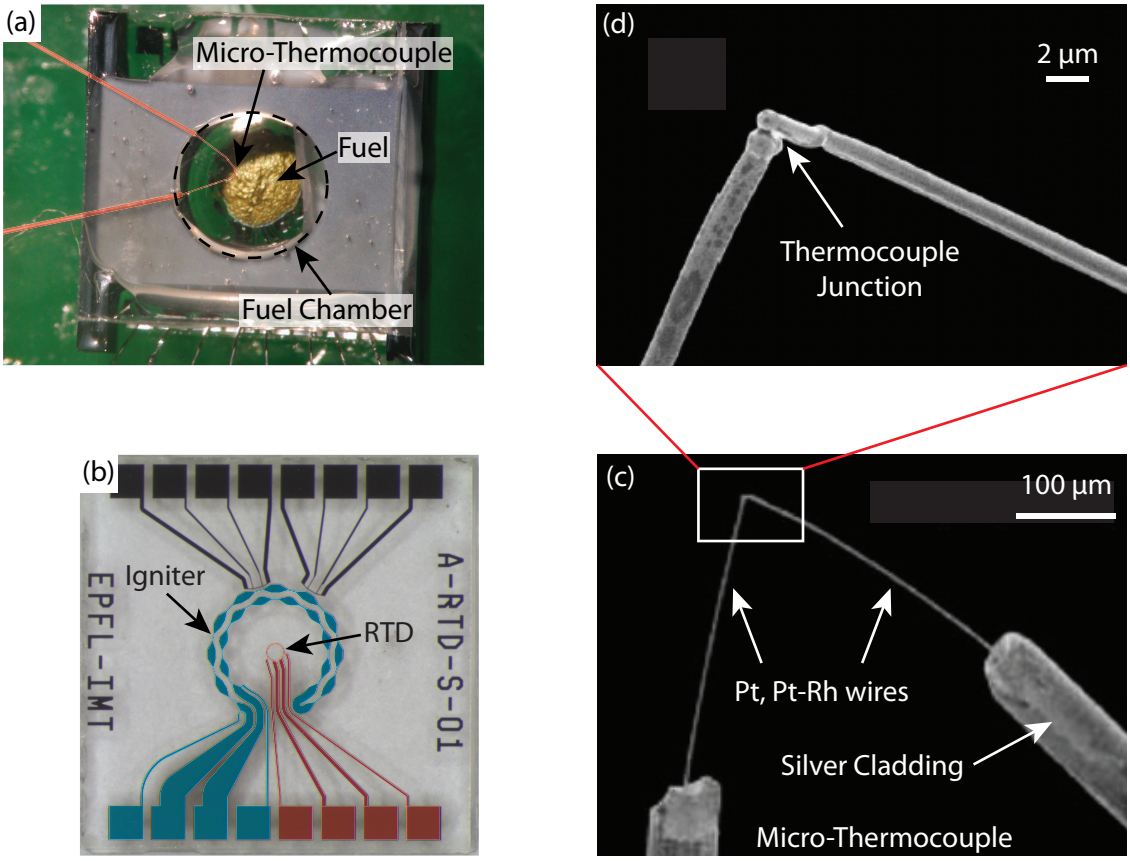

Figure 3.7: (a) Picture of a closed-chamber pyroMEMS chip used for temperature measurements. (b) Picture of the igniter chip showing the hot spot igniter (blue) and the RTD (red). (c) Picture of the micro-thermocouple with (d) a close-up of the thermocouple junction [47].

The second was a custom-made S-type micro-thermocouple fabricated by our project partners at FEMTO-ST, in Belfort, France (figure 3.7c and d) [48]. The thermocouple consisted of two 1.3 μm diameter platinum and platinum-rhodium (10 %) wollaston wires. The silver cladding (~ 75 μm in diameter) near the end of the wires was etched away electrochemically using nitric acid. The tips of the two wires were welded together by capacitive discharge resistance welding to create the thermocouple junction. The volume of the junction was less than 10

μm^3.

The advantage of the FEMTO-ST micro-thermocouple is its small size—yielding a small thermal inertia and fast response time—and large temperature range (up to 1600 °C). The response time of the thermocouples was less than 1 ms [48]. The disadvantage of the thermocouple is its extreme fragility and non-trivial integration with the pyroMEMS device.

Experimental Setup

The temperature measurements were made inside closed pyroMEMS chambers. The fuel was ignited using drop-coated, bottom-side, hot spot igniters (see the closed chamber section of chapter 4 for more details). A picture of the device is shown in figure 3.7a. A total of 23 devices were tested (see table 3.3). Both 10 % and 20 % binder mass fraction fuel drops were tested. The 10 % and 20 % binder drops weighed 60^{+104}_{-1} μg and 104^{+148}_{-1} μg, respectively. The fuel drops were enclosed in a silicon chamber chip measuring 2.3 mm in diameter and 525 μm tall. Three different chamber sizes were tested using 1, 2 or 3 chamber chips stacked on top of each other, such that the largest chamber measured 1.575 mm tall and had an internal volume of 6.5 mm^3. The silicon chamber was closed using a glass cap. The devices were assembled individually using 2-part epoxy glue (araldite® by Huntsman Advanced Materials). The fuel was ignited using a 23.5 V pulse (input power = 1.4 W) lasting between 1 and 2 s.

Table 3.3: Matrix of test device parameters (Temperature).

	Binder Content		
Chamber Height (μm)	10 %	20 %	Total
525	8	0	8
1050	6	4	10
1575	4	0	4
Total	18	4	22

Results

All but the largest chambers—1.575 mm tall—ruptured under the large pressures produced inside the closed chambers. Typical temperature traces are shown in figure 3.8. The RTD temperature trace shows parasitic heating from the igniter—which was turned on at ~ 0.51 s—as well as a small temperature pulse at the onset of fuel combustion at 1.115 s (ignition delay time of 0.6 s). The small decrease in temperature—i.e., resistance—measured at the onset of ignition was due to the free radicals as the combustion wave passed over the RTD. The free radicals were captured by the RTD and artificially increasing the current entering the circuit. The small increase in current was registered as a decrease in resistance—i.e., temperature. The maximum recorded temperature was 280 ± 2 °C. The effect of the combustion event decayed away after roughly 200 ms. This peak temperature is a far cry from the adiabatic flame

temperature of 1190 ± 30 °C given by the ICT code. Due to the RTD's intimate contact with the chamber wall, the temperature it saw was representative of the wall surface temperature, rather than the combustion gas temperature inside the chamber.

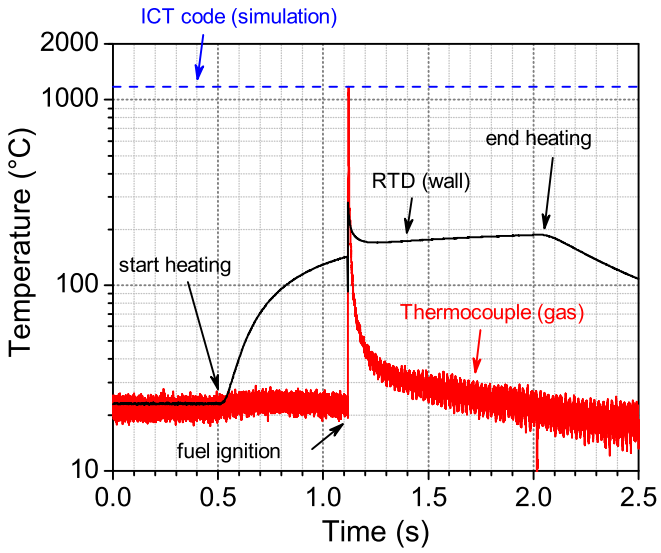

Figure 3.8: Temperature vs. time of the K-DNBF combustion (20 % binder) as measured by the micro-thermocouple (red line) and the resistance temperature detector (black line). The ICT code simulation

The micro-thermocouple registered a very small increase of 1.5 ± 1.4 °C after the onset of the voltage pulse. The temperature pulse due to combustion began at 1.118 s and decayed below 1 % of the maximum temperature after ~ 350 ms. The maximum temperature recorded was 1180 ± 10 °C after a rise time of 1.8 ms—which is about the same order of magnitude as the thermocouple time constant. Due to its small thermal mass and location—suspended inside the combustion chamber—the micro-thermocouple temperature was representative of the combustion products temperature. The average peak gas temperature—for the 4 successful 10 % binder, 1575 μm high chambers—was 1300 ± 160 °C, which is in excellent agreement with the ICT results of 1190 ± 30 °C.

3.4.2 Pressure

Introduction

Accurate pressure measurements inside the millimeter-scale pyroMEMS combustion chambers are difficult to obtain for two reasons:

1. *Small Volume.* The combustion chambers are quite small; therefore, regular commercial pressure sensors cannot be used due to the relatively large dead space within these

sensors.

2. *High Combustion Temperature.* Pressure transducers are generally temperature-sensitive devices, as such, the >1000 °C temperature pulse accompanying the fuel combustion can potentially degrade the performance of the pressure sensor.

Rather than develop a custom-made pressure sensor—which needs to be calibrated and validated—we chose to use commercial off-the-shelf MEMS piezoresistive pressure sensors provided by Measurement Specialties, Bevaix, CH.

Choice of Pressure Sensor

In order to minimize the amount of sensor dead space, unpackaged, MEMS pressure sensors were directly glued onto the combustion chamber (see figure 3.9). As such, the pressure inlet port needed to be on the backside of the pressure sensor—i.e., on the opposite side of the bond pads. So-called harsh environment pressure sensors—designed to operate in corrosive environments—are configured this way. The highest pressure harsh MEMS pressure sensors available from Measurement Specialties have a range of 0 to 36 bar. Based on the ICT simulations, the equilibrium constant volume combustion pressure was predicted to be between 70 bar and 340 bar—assuming no heat losses. Nevertheless, the burst pressure for the sensor is rated at 170 bar, therefore, the sensor should survive the combustion process using the smallest drops.

Since the pressure sensor was directly glued onto the closed pyroMEMS combustion chamber, the pressure sensor full-scale span—i.e., the voltage signal at 36 bar—could not be individually calibrated before firing. Instead, span calibration data from chips from the same wafer was obtained from Measurement Specialties and was 145 ± 8 mV. Assuming this data is normally distributed and representative of our pressure sensors, the error induced by not individually calibrating the sensors was 8.5 %, based on a 99 % confidence interval.

Experimental Setup

The pressure measurement setup was similar to that of the temperature measurements: the device consisted of a borosilicate glass igniter chip, a silicon chamber and a silicon nozzle, on top of which the pressure inlet port will be placed (see figure 3.9). However, design changes were made to the chamber geometry to increase the chamber volume to lower the combustion pressures. The silicon chamber diameter was increased to 5 mm and the silicon thicknesses of 525 μm and 1 mm were tested, leading to chamber volumes of 10.3 mm^3 and 19.6 mm^3, respectively—versus 6.5 mm^3 for the temperature measurements. In addition, the gluing area was increased from 12.6 mm^2 to 38.4 mm^2 to increase the bond strength and help prevent gas leakage at the interface. The different elements were assembled together with epoxy adhesive. Since the combustion pressure was so sensitive to fuel mass loading density, each device as individually weighed to determine its exact fuel mass.

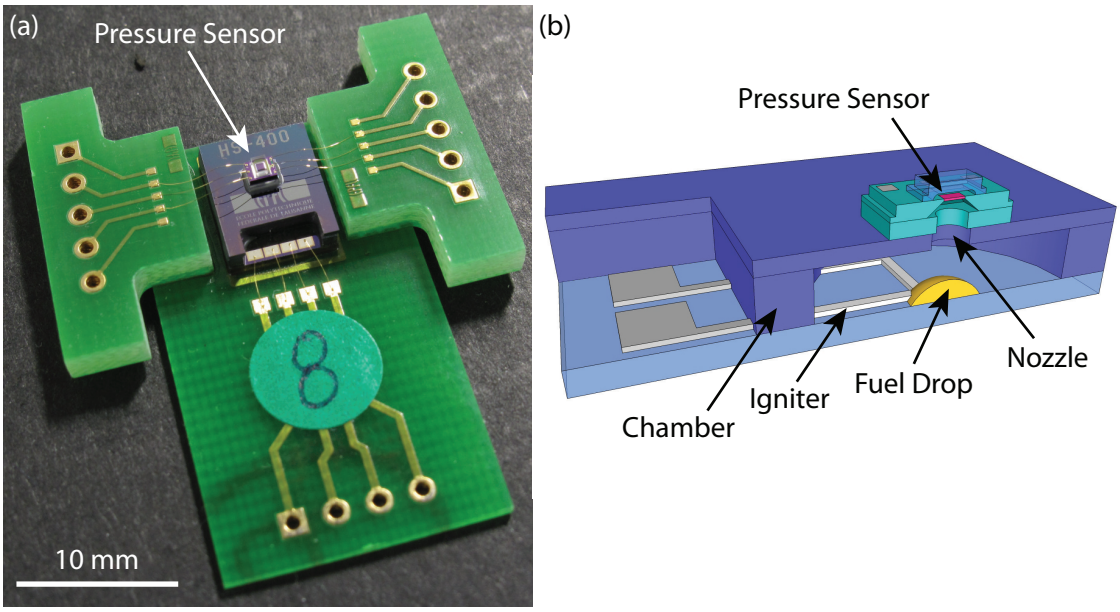

Figure 3.9: (a) Picture of a closed-chamber pyroMEMS chip used for pressure measurements. (b) Sketch showing the cross-section of the device.

Table 3.4: Matrix of test device parameters (Pressure).

	Binder Content		
Chamber Height (μm)	10 %	20 %	Total
525	2	2	4
1000	3	3	6
Total	5	5	10

The pressure sensor was powered with a DC supply voltage of 5 V and the output voltage was recorded with a digital multimeter (Agilent 34410A) at a sampling rate of 10 kHz. The pyroMEMS chip was ignited by a 1 s, square voltage pulse of 23 V using a function generator (HP33120A) coupled to a high-speed power amplifier (NF Electronic Instruments 4015). Both instruments were controlled and triggered using a custom MATLAB script.

Results

Only 2 devices were successfully tested out of a total of 10—due to failure of the bonding between the igniter and the chamber layers. This was partially due to the larger fuel masses obtained in the 2^{nd} deposition run. One success for each of the 10 % and 20 % binder mass fractions was obtained—the two successful tests were both using the larger chamber volume. A successful pressure trace is shown in figure 3.10. Fuel ignition was detected by the pressure sensor at 700.6 ms and a peak overpressure of 60 ± 5 bar was measured 0.9 ms later. The fuel mass for this drop contained 10 % binder and weighed 263 μg, resulting in a simulated combustion pressure of 58 bar—which is excellent agreement with our experimental result, within the uncertainty of the experiment. The pressure pulse lasted 93.4 ms—the time for the pressure to drop below 0.67 % (5 time constants) of its maximum value. The chamber pressure decayed exponentially to ~ 10 bar after 300 ms before suddenly dropping off again (see figure 3.10 inset). This transition occurred at the same time as the ignition pulse ended—after 1 s. The remaining pressure decay was fitted to an exponential decay function and the final asymptotic chamber pressure was found to be 9.2 ± 0.8 bar. That the final pressure was so large indicated that the combustion chamber did not have any significant leaks or failures due to the high pressure combustion event.

The second successful test was carried out in a 1000-μm thick chamber with a 20 % binder fuel drop weighing 238 μg. The recorded a peak overpressure of 38 ± 3 bar—compared with a simulated overpressure of 51 bar. The simulated pressure was 34 % larger than the experimental result.

3.5 Discussion

3.5.1 Fuel Selection and Deposition Method

In this chapter, we presented the K-DNBF fuel mixture that will be used throughout this thesis. The fuel was selected due to its handling safety, its relatively low ignition temperature and large amount of gaseous combustion products generated. The propellant was mixed with a water soluble binder to improve its adhesion strength and tailor its chemical reaction kinetics. The fuel was specially formulated to yield small particles sizes to allow it to be dispensed onto the pyroMEMS devices. By adding a large amount of solvent—water—to the propellant/binder mixture and turning it into a paste, the fuel was easily drop-coated onto the pyroMEMS devices using a liquid dispenser. This greatly simplified the task of integrating the solid propellant fuel

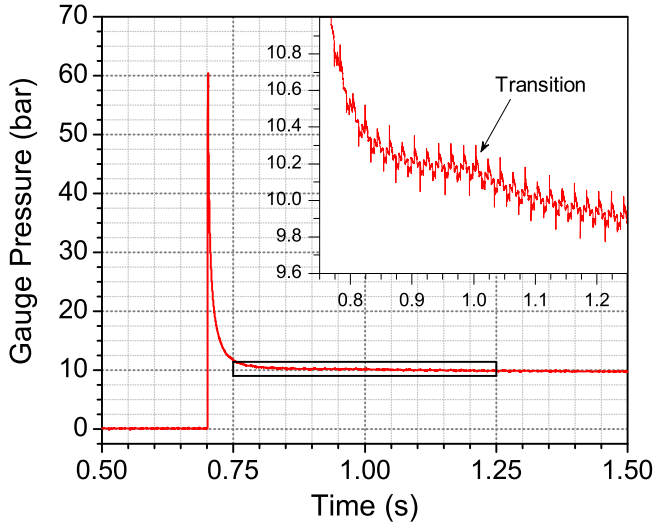

Figure 3.10: Gauge pressure vs. time of the K-DNBF combustion (10 % binder).Inset: The decay transition in the pressure trace when the ignition pulse ended.

into the device in a safe manner. Still, the deposition parameters still need to be optimized to obtain reliable and well-controled drop sizes.

3.5.2 Experimental Validation

Although very few successful validation experiments were carried out, the temperature and pressure data obtained to date are in excellent agreement with the ICT code simulation results (see table 3.5). This gives us some degree of confidence that the ICT code simulations are in good agreement. Also, combustion of solid propellant fuels in pyroMEMS do not differ drastically from macroscale devices with several grams or more of fuel.

Table 3.5: Summary of the temperature and pressure experiments.

Parameter	Sensor Type	# success	Binder (%)	ICT Prediction	Experiment
Temperature (°C)	RTD	4	10	1190 ± 30	280 ± 2
	μ-TC	4	10	1190 ± 30	1300 ± 160
Pressure (bar)	piezoresist.	1	10	58	60 ± 5
	piezoresist.	1	20	51	38 ± 3

As mentioned previously, thermodynamic property measurements within pyroMEMS devices are challenging because commercial off-the-shelf sensors adapted for such measurements do not exist. These measurements required highly miniaturized sensors—so as to not disturb the system—with sub-millisecond response times.

The main cause of device failure was the violent rupture of the combustion chambers at the bonded interface between the chamber layer and the glass cap. Gluing the different components together manually was highly unreliable and time consuming. For this reasons such as this, a wafer-level assembly techniques are needed to obtain large numbers of identical pyroMEMS devices. One such technique will be presented in chapter 6 for fabricating pyroMEMS balloon actuators.

Temperature

The combustion gas temperature measurements were carried out using thin-film platinum RTDs and custom-made S-type micro-thermocouples. The enormous difference ($\sim$ 1000 °C) between the two temperature sensors indicate the importance of using well adapted sensors for measurements in pyroMEMS devices. The rise time of the temperature pulse as on the same order of magnitude as the micro-thermocouple response time, indicating that the dynamics of the temperature rise may not be well resolved. The sensors were not damaged by the explosion and continued to operate long after the combustion event. The integration of the micro-thermocouples into the combust chambers was very delicate and required specialized micro-positioning equipment.

Pressure

The combustion chamber pressure measurements were made using commercially-available MEMS pressure sensors. The harsh-environment type sensors were used, because they allowed the pressure sensor to be mounted directly on top of the combustion chamber, thus minimizing the sensor dead space. However, the highest pressure range available from the MEMS pressure sensor supplier was 36 bar—whereas combustion pressures of up to 60 bar were recorded. This introduced additional sources of measurement error, due to the nonlinearity of the sensor beyond its measurement range.

Furthermore, piezoresistive pressure sensors are sensitive to temperature variations. This temperature sensitivity is given by the temperature coefficient of span (TCS), which represents the effect of a temperature increase on the voltage level at full span (36 bar). For our sensors, it was -2040 ± 5 ppm/°C over a temperature range of -40 °C to $+125$ °C. Although the gas temperature was found to peak around 1200 °C, the increase in glass wall temperature due to the fuel combustion—as measured by the platinum RTD—was only $\sim$ 180 °C. Assuming the piezoresistive element was heated to the same extent as the glass wall—and the TCS is valid at this temperature—this temperature induced error was less than 1 %. However, it is unclear to what temperature the MEMS pressure sensor was heated during the experiments.

3.6 Conclusion

In this chapter, we presented the fuel that will be used throughout this thesis. The fuel combustion was simulated using a chemical equilibrium code developed by the Fraunhofer Institute for Chemical Technology (ICT). Initial experiments conducted were carried out to validate the ICT code for use in pyroMEMS devices. Although more tests need to be carried out, this initial validation gives us some degree of confidence that we can successfully predict the combustion of our solid propellant mixture in pyroMEMS devices. The ICT code will integrated into a larger model that will be used for the design and the performance characterization of the pyroMEMS balloon actuators presented in chapter 6.

4 Bottom-side Igniters

4.1 Introduction

As mentioned in chapter 2, the reliability and performance of pyroMEMS devices requires a fuel well adapted to pyroMEMS—both in terms of combustion performance and deposition method—and proper igniter architecture to achieve complete combustion of the fuel.

In this section we will investigate the ignition and combustion behavior of drop-coated, bottom-side igniters while varying the igniter layout, propellant formulation (i.e., binder content), substrate material (borosilicate glass and polyimide) and input power level. The goals are to better understand fuel ignition and combustion at the microscale as well as evaluate different techniques to mitigate fuel peeling and ejection using bottom-side igniters. Finally, closed-chamber pyroMEMS devices were tested to investigate the effect of confinement on the fuel's ignition and combustion behavior.

4.1.1 Igniter Concept

Bottom-side Igniters

By fabricating the Joule-heating igniters on a bulk substrate and depositing the fuel directly on top via drop coating, one ensures intimate thermal and mechanical contact between the two. In this way, highly reliable *ignition* behavior is expected. However, igniting the fuel from beneath ostensibly leads to combustion of a thin layer of fuel in contact with the igniter and ejection of the remaining—unburned—propellant [14, 19].

Fuel Peeling

Fuel peeling and ejection occur when the gas and energy released by the fuel combustion overcomes the adhesion strength of the fuel to the substrate. There are many factors that can induce or mitigate fuel peeling:

1. *Surface Adhesion.* Increasing the surface adhesion of the fuel can help mitigate the onset of fuel ejection. Increasing the binder content of the fuel can increase its adhesion to the substrate. Also, extensive pre-heating the fuel decreases the structural integrity of the binder, lowering its adhesion strength.

2. *Fuel Kinetics.* Increasing the energy density of the fuel, or increasing its burning rate increases the risk of fuel ejection. Increasing the binder content decreases the energy density of the fuel, while decreasing the amount of pre-heating of the fuel charge decreases the its burning rate.

Fuel Drops on Annular Igniters

In order to prevent fuel peeling, the igniter was designed as an annular ring in order to concentrate the heat flux along the periphery of the fuel drop [32]. In this way, fuel ignition occurs at the edge of the drop and propagates smoothly around the periphery towards the center. The fuel drop remains anchored to the substrate due to the adhesion provided by binder in the fuel mixture. This ignition concept is made possible due to the controlled deposition of small fuel drops enabled by (1) the dispensing method chosen, and (2) the small particle size of the explosive material. The "droplet" shape of the fuel is key because the heating profile of the propellant depends on its local heat capacity, which is a function of fuel thickness—the larger the thickness above the igniter, the slower it heats up.

4.1.2 Layouts

Three different layouts were tested in this study: meander, annular and hot spot. The meander layout—used by almost all other pyroMEMS devices—served as the baseline against which the other two layouts will be compared. Next, the annular layout represented a "nominal" annular igniter and consisted of three concentric heating rings. Lastly, the "hot spot" igniter consisted of two concentric heating rings containing short, thin segments designed to increase the local heat flux.

Meander Layout

First, the meander igniter (see figure 4.1) consisted of a meandering or serpentine line heater, 50 μm wide, with a 50 μm inter-line spacing. It was designed to generate an uniform heat flux to the fuel drop. The total heated area was 1.75 mm X 1.75 mm—which is larger than the average fuel drop—to ensure the complete drop is heated relatively uniformly. It represented our "control group", i.e., the standard igniter layout that has been used in the literature. Each subsequent layout incorporated features designed to mitigate fuel peeling.

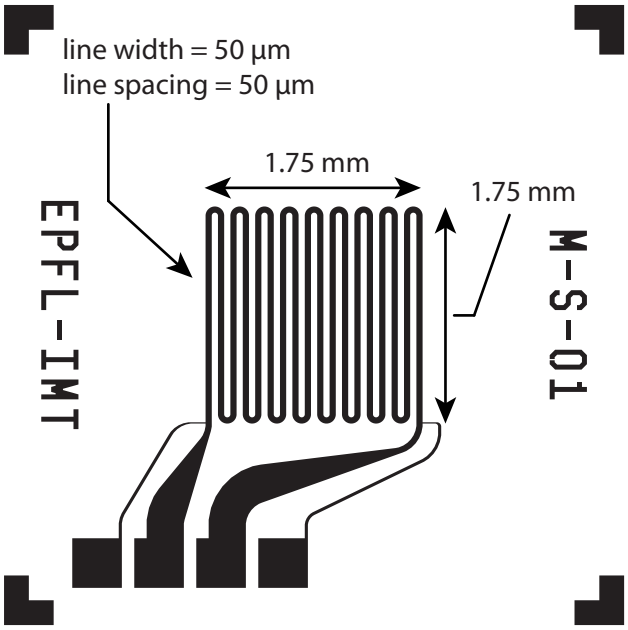

Figure 4.1: Meander igniter layout.

Annular Layout

Second, the annular heater (see figure 4.2) was designed to limit the heated zone to the periphery of the fuel drop. In this way, fuel ignition is stimulated near the edge of the fuel in order to prevent fuel peeling. It was composed of three concentric rings also measuring 50 μm wide, with a 50 μm inter-line spacing. The outermost diameter of the rings measured 1.5 mm—close to the average fuel drop diameter. Three rings rather than a single one were used due to the limited precision of the manual fuel deposition method—both in terms of drop position and dispensed mass.

Hot Spot Layout

Lastly, the hot spot igniter (see figure 4.3) was a modified annular igniter with 2 concentric rings containing short, thin line segments. These so-called “hot spots” are designed to localize fuel heating to prevent fuel ejection and reduce the input power needed for ignition. They measured 10 μm in width and 100 μm in length. The hot spots were evenly interspersed with wider line segments measuring 100 μm in width. The gap between the concentric rings was kept constant at 70 μm, making the combined width of the heater 180 μm. The outer diameter of the wide line segments measured 1.6 mm.

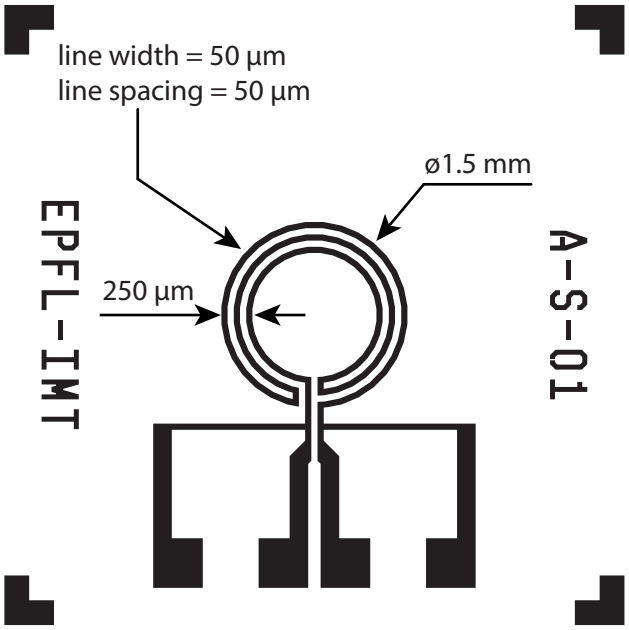

Figure 4.2: Annular igniter layout.

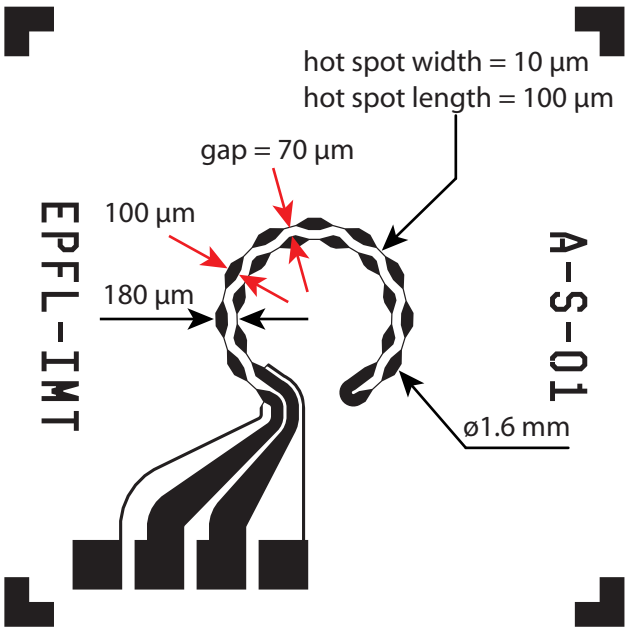

Figure 4.3: Hot spot igniter layout.

4.2 Fabrication

4.2.1 Igniters

The pyroMEMS igniters were fabricated on 500-μm thick glass substrates and 50-μm thick polyimide foils via a lift-off process and consisted of a 15-nm-Ta/235-nm-Pt film deposited via electron-beam evaporation. For the devices fabricated on polyimide foil, the foil was cut to the size of a 4 inch wafer, bonded to a carrier wafer using an adhesive (waferBOND® CR-200 by Brewer Science) and processed in the same way as the glass wafer. At the end, the foil was separated from the carrier wafer in a heated bath of waferBOND® remover at 120 °C. The resulting igniter resistances are given in table 4.1. As expected, the resistances of the photolithographically-defined igniters have relatively small errors (~ 2 %)—these values will serve as benchmarks for the shadow-mask-evaporated igniters (in chapter 5) and inkjet-printed igniters (in chapter 6).

Table 4.1: Bottom-side igniter resistance values.

Layout	Resistance (Ω)
Meander	446 ± 7
Annular	197 ± 3
Hot spot	210 ± 5

Some hot spot igniters were also processed with 3 resistance temperature detectors (as shown in figure 3.7): one in the center, one near a hot spot (offset = 25 μm) and a third near the wide segment of the igniter (offset = 25 μm). The central RTD was used to estimate the combustion temperature, while the two others were used to estimate the igniter temperature at the hot spot and wide segments, respectively. The temperature coefficient of resistance of the Ta/Pt heaters was measured in a temperature controlled oven and found to be 2960 ppm/°C (based on a reference temperature of 23 °C).

4.2.2 Chambers

A small number of igniters were tested inside closed combustion chambers—the same chambers used for the temperature measurements in chapter 3. The 2.3 mm diameter, cylindrical combustion chambers were made by deep reactive ion etching through the entire thickness of a 525 μm silicon wafer. The chambers consisted of 1, 2 or 3 wafers tall (525 – 1575 μm) bonded together on the igniters using 2-part epoxy (araldite® by Huntsman Advanced Materials). The chambers were sealed on top using a 500 μm-thick glass chip to allow optical access to the combustion event.

4.2.3 Fuel Deposition

The fuel was deposited on the igniters using the dispenser, as described in chapter 3. The devices were drop-coated in two separate runs. In the first run, 3 different binder mass fractions were used (5,10 and 20 %), whereas in the second run only 10 % and 20 % binder was used—since there was no significant difference between the results for 5 % and 10 % binder. The first run was carried out on hot spot and meander igniters, while hot spot and annular igniters were coated in the second one. The range of fuel masses deposited during the second run was much higher than for the first run. This meant that only "large fuel masses" were tested with the annular layout, while only "small fuel masses" were tested with the meander layout (see table 4.2). Since the fuel mass distribution is not normal—but rather heavily skewed towards the positive values—the results are given in terms of mode with the 25 % and 75 % percentiles as the error range. If the 25 % percentile was larger than the modal value, then the error bar was set to zero.

Table 4.2: Bottom-side igniter fuel masses.

Run #	Binder (%)	# igniters	Fuel Mass (μg)
1	5	52	65^{+135}_{-13}
	10	58	60^{+104}_{-1}
	20	58	104^{+148}_{-1}
2	10	94	312^{+123}_{-0}
	20	96	418^{+86}_{-0}

4.3 Theory

4.3.1 Assumptions

Rather than simply limit ourselves to assuming that the ignition delay times decayed exponentially with input power, analytical models were constructed based on the igniter layouts in order to gain deeper insight into the ignition phenomenon of pyrotechnics at the microscale. However, due to the complex geometry of the igniters and that the thermal properties of the fuel are unknown, many simplifications and assumptions were needed. Nevertheless, the goal of the models was to capture the general behavior of the igniters. The following approximations were taken to obtain closed-form solutions:

1. The fuel and substrate were modeled as two semi-infinite domains with the igniter placed at the boundary between the two. The igniter is not directly modeled, but treated as a boundary condition. This assumption ignores any effect of the finite thickness of both the fuel drop and the substrate on the models;

2. The igniter was assumed to behave as a constant heat flux boundary condition. Although this assumption is not strictly valid, it is a necessary simplification to obtain closed-form

solutions. In reality, a constant voltage was applied to the igniters causing the input power to decay exponentially over time due to the increasing igniter resistance with temperature (see figure 4.9). The error induced by this approximation increased with decreasing ignition delay time, as the power curve asymptotes over time;

3. Ignition occurred immediately when any portion of the fuel reached the propellant's ignition temperature. This implies that the fuel's induction period—the time required for the chemical reactions to occur—was negligible compared to the ignition delay time.

Furthermore, the following property values were used in this study:

1. The fuel mixture's ignition temperature was 204 °C and independent of binder content (see chapter 3);

2. The ambient temperature T_0 was 24 °C;

3. The energetic component of the fuel mixture was taken to be an isotropic organic compound with constant properties. As a gross estimate, the thermal properties of the fuel were assumed to be independent of binder content and on the order of the organic compounds found in appendix 2 of [49]:

   - Thermal conductivity: $k_f \sim 0.1$ W/(m·K);
   - Thermal diffusivity: $\alpha_f \sim 0.1$ mm^2/s.

4. The borosilicate glass substrate has the following thermal properties [50]:

   - Thermal conductivity: $k_{glass} \sim 1.2$ W/(m·K);
   - Thermal diffusivity: $\alpha_{glass} \sim 0.65$ mm^2/s.

5. The polyimide polymer substrate has the following thermal properties [51]:

   - Thermal conductivity: $k_{pi} \sim 0.29$ W/(m·K);
   - Thermal diffusivity: $\alpha_{pi} \sim 0.174$ mm^2/s.

4.3.2 Meander Model

Theoretical Basis

For the meander layout, the igniter is modeled as a constant heat flux boundary condition (B.C.) sandwiched between two semi-infinite solids—the fuel and the glass substrate (see

figure 4.4). The temperature field as a function of time t and distance from the heater x in each semi-infinite solid is given by [52] as

$$\Delta T_M(x,t) = \frac{Q}{Sk}\left[\sqrt{\frac{\alpha t}{\pi}}\exp\left(-\frac{x^2}{4\alpha t}\right) - \frac{x}{2}\mathrm{erfc}\left(\frac{x}{2\sqrt{\alpha t}}\right)\right] \tag{4.1}$$

where $\Delta T_M(x,t) = T_M(x,t) - T_0$ is the temperature increase in the solid due to the meandering igniter, x is the height of the solid—with the origin at the constant heat flux boundary—t is the time, Q is the input power, S is the heater surface area, and k and α are the thermal conductivity and thermal diffusivity of the solid, respectively. The maximum temperature in the solid occurs at the heated boundary (i.e., $x = 0$) and is equal to

$$\Delta T_M(x=0,t) = \frac{Q}{Sk}\sqrt{\frac{\alpha t}{\pi}} \tag{4.2}$$

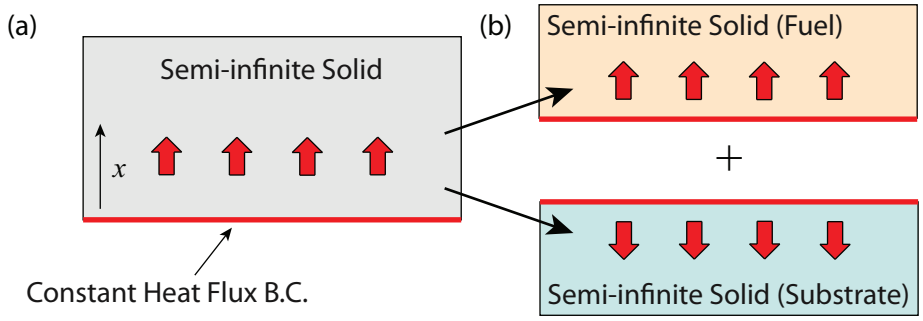

Figure 4.4: Sketch of (a) the semi-infinite plane heater model and (b) the meander igniter model.

Ratio of Power Dissipated by the Fuel

The power dissipated by each solid—Q_f and Q_s for the fuel and substrate, respectively—is not the same and depends on the thermal properties of each solid (see figure 4.5). In order to determine the two input powers we require two equations. First, we require that the interfacial temperature in each solid to be the same, i.e.,

$$\Delta T_{M,f}(x=0,t) = \frac{Q_f}{Sk_f}\sqrt{\frac{\alpha_f t}{\pi}} = \frac{Q_s}{Sk_s}\sqrt{\frac{\alpha_s t}{\pi}} = \Delta T_{M,s}(x=0,t) \tag{4.3}$$

where $\Delta T_{M,f}$ and $\Delta T_{M,s}$ are the temperature increases in the fuel and substrate, respectively.

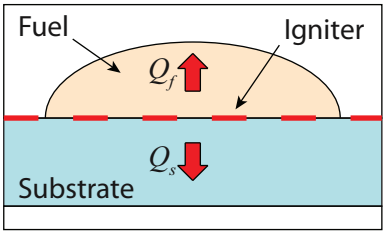

Figure 4.5: Cross-section sketch of the meander igniter.

The subscripts f and s represent the properties and variables associated with the fuel and substrate, respectively. Second, the total input power must equal the power dissipated by the fuel and the substrate:

$$Q_{total} = Q_f + Q_s \tag{4.4}$$

The total input power is calculated in the usual way as

$$Q_{total} = \frac{1}{\Delta t_I}\int_0^{\Delta t_I} I(t)V(t)\mathrm{d}t \tag{4.5}$$

where I, V and Δt_I are the current, voltage and ignition delay time, respectively. Substituting equation (4.4) into (4.3), one obtains the ratio of the total igniter power dissipated by the fuel

$$\eta_M \equiv \left(Q_f/Q_{total}\right)_M = \left(1 + \frac{k_s}{k_f}\sqrt{\frac{\alpha_f}{\alpha_s}}\right)^{-1} \tag{4.6}$$

Model

At ignition, the maximum temperature in the fuel grain $\Delta T_{M,f}$ is equal to the ignition temperature ΔT_I and the time t is equal to the ignition delay time Δt_I. Substituting these relations as well as equations (4.5) and (4.6) into (4.2) gives

$$\Delta T_I = \frac{Q_{total}\eta_M}{S_M k_f}\sqrt{\frac{\alpha_f \Delta t_I}{\pi}} \tag{4.7}$$

Rearranging yields a power relation of the form

$$\Delta t_I = K_1 Q_{total}^{K_2} \tag{4.8}$$

where

$$K_1 = \frac{\pi}{\alpha_f}\left(\frac{k_f S_M \Delta T_I}{\eta_M}\right)^2 \tag{4.9}$$

$$K_2 = -2 \tag{4.10}$$

This equation can easily be linearized by taking the logarithm of both sides:

$$\log_{10}(\Delta t_I) = \log_{10}(K_1) + K_2 \cdot Q_{total} \tag{4.11}$$

Limits

The above analytical solution applies for a limited range of ignition delay times based on the thermal penetration depth ($\delta \sim \sqrt{\alpha_f t}$) of the heat. The lower limit requires that the thermal penetration depth be much larger than the igniter's interline spacing, i.e.,

$$\delta \sim \sqrt{\alpha_f t} > l_{gap} \tag{4.12}$$

where $l_{gap} = 50\ \mu$m. Rearranging:

$$t_{min} > t_{gap}^2/\alpha_f \sim 6.25\ \text{ms} \tag{4.13}$$

The upper limit is dictated by the thickness of our "semi-infinite solids"—the fuel and the substrate. Given the hemispherical shape of the fuel drops, it is not obvious what thickness value to assign to them; therefore, for the sake of simplicity, the thickness of the fuel will be ignored for the moment. The thickness of the substrate h_s is approximately 500μm for the glass substrates and 50μm for the polyimide foil. In order to maintain thermal penetration

depths below this thickness one requires

$$\delta_{max} \sim \sqrt{\alpha_s t_{max}} < h_s \tag{4.14}$$

or,

$$t_{max} < h_s^2/\alpha_s = \begin{cases} \sim 0.4 \text{ s} & \text{for the glass substrate,} \\ \sim 14 \text{ ms} & \text{for the polyimide foil,} \end{cases} \tag{4.15}$$

4.3.3 Annular Model

Theoretical Basis

The annular igniter consisted of three long, concentric line heaters in close proximity. The annular model is based on the analytical solution of a semi-infinite line heater heating a semi-infinite solid (see figure 4.6) given by [52].

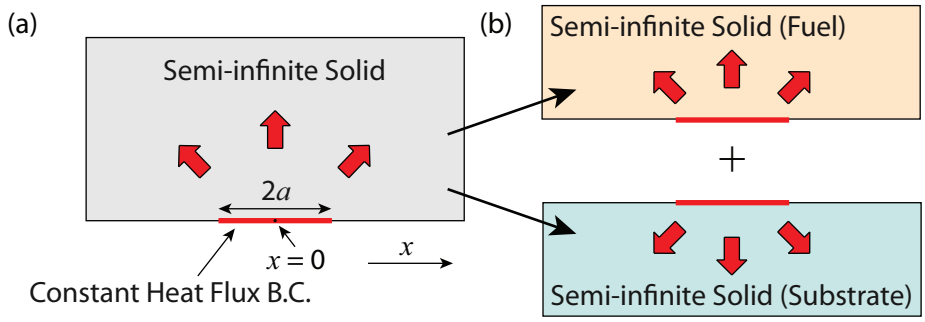

Figure 4.6: Sketch of (a) the semi-infinite line heater model (line width $2a$) and (b) the annular igniter model.

The maximum temperature—at the heater centerline, i.e., $x = 0$—is equal to

$$\Delta T_A(x=0,t) = T_A(x=0,t) - T_0 = \frac{2Qa}{Sk}\sqrt{\frac{\tau}{\pi}}\left\{\text{erf}\left(\frac{1}{2\sqrt{\tau}}\right) - \frac{1}{2\sqrt{\pi\tau}}\text{Ei}\left(-\frac{1}{4\tau}\right)\right\} \tag{4.16}$$

where the error function $\text{erf}(x)$ is given as

$$\text{erf}(x) = \frac{2}{\sqrt{\pi}}\int_0^x \exp(-u^2)\,\text{d}u \tag{4.17}$$

the exponential integral $\mathrm{Ei}(-x)$ is defined as

$$\mathrm{Ei}(-x) = -\int_x^\infty \frac{\exp(-u)}{u}\mathrm{d}u \tag{4.18}$$

and τ is the non-dimensionalized time, $\tau = \alpha t/a^2$. A compact solution—i.e., one that can be inverted into the form $\Delta t_I = f(Q)$—exists for long ignition delay times, such that the thermal penetration depth ($\delta \sim \sqrt{\alpha_f t}$) is much larger than the igniter half-width a, i.e., $t \gg a^2/\alpha$—in practice, $t \geq 5a^2/\alpha$ is used. Therefore,

$$\lim_{\tau \gg 1}\left\{\mathrm{erf}\left(\frac{1}{2\sqrt{\tau}}\right)\right\} = \frac{1}{\sqrt{\pi\tau}} \tag{4.19}$$

$$\lim_{\tau \gg 1}\left\{\mathrm{Ei}\left(-\frac{1}{4\tau}\right)\right\} = -\gamma - \ln\left(-\frac{1}{4\tau}\right) \tag{4.20}$$

This solution is given by [52] as

$$\Delta T_A(x=0,t) = T_A(x=0,t) - T_0 \approx \frac{Qa}{S\pi k}\left(2 + \ln\left(\frac{4\alpha t}{Ca^2}\right)\right) \tag{4.21}$$

where $\ln C = \gamma \approx 0.57722$ is the Euler-Mascheroni constant.

Choice of Half-Width 'a'

For the annular igniter geometry tested, the igniter can be seen to behave in two different ways, depending on the thermal penetration depth of the heat before ignition:

1. *Large thermal penetration depth.* If the thermal penetration depth is much larger than the spacing between the annular rings, then the three rings at as one and a value of $a = 125$ μm is used— half of the 3×50 μm lines + 2×50 μm interline spacing (figure 4.7b).
2. *Short thermal penetration depth.* If the ignition delay time thermal penetration depth is smaller than the spacing between the annular rings, then the rings are independent of each other and a value of $a = 25$ μm is used (figure 4.7c).

In order to determine in which regime the igniter is operating, the inequality $t \geq 5a^2/\alpha$ is used:

Case 1: $a = 25$ μm $\Rightarrow$ $t \geq 31.25$ ms.

Case 2: $a = 125$ μm $\Rightarrow$ $t \geq 781.25$ ms.

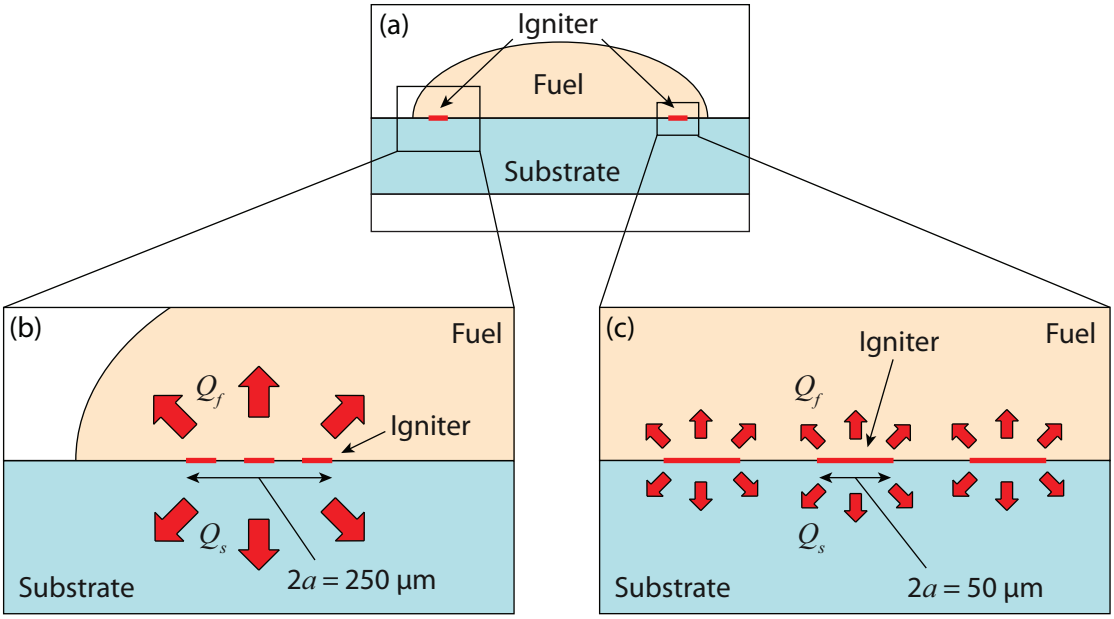

Figure 4.7: Cross-section sketch of (a) the annular igniter consisting of three concentric rings (50 μm wide and 50 μ spacing) showing the two different thermal behaviors depending on the ignition delay time: (b) the situation where the thermal penetration depth δ is much larger than the spacing between the heaters and (c) the case where the thermal penetration depth is smaller than the spacing.

Ratio of Power Dissipated by the Fuel

The ratio of total power dissipated by the fuel for the annular layout is determined in the same manner as the meandering igniter, yielding:

$$\eta_A \equiv (Q_f/Q_{total})_A = \left[1 + \frac{k_s}{k_f}\frac{\left[2+\ln\left(4\alpha_f t/Ca^2\right)\right]}{\left[2+\ln\left(4\alpha_s t/Ca^2\right)\right]}\right]^{-1} \tag{4.22}$$

Model

Inverting equation (4.21), and substituting in the propellant's ignition temperature and ignition delay time yields

$$\Delta t_I = K_3 \exp\left(K_4 Q_{total}^{-1}\right) \tag{4.23}$$

where

$$K_3 = \frac{Ca^2}{4\alpha_f \exp(2)} \tag{4.24}$$

$$K_4 = \frac{\pi k_f S_A \Delta T_I}{\eta_A a} \tag{4.25}$$

This expression can be linearized by taking the natural logarithm of both sides:

$$\ln(\Delta t_I) = \ln(K_3) + \left(K_4 \hat{Q}_{total}\right) \tag{4.26}$$

where $\hat{Q}_{total} = Q_{total}^{-1}$.

4.3.4 Hot Spot Model

For the hot spot igniters, we make use of the same line-heater model as for the annular model. However, the choice of line width is not so obvious for the hot spot igniter. For the large thermal penetration depth case, we ignore the details of the igniter and treat it as a single line of total width of 180 μm—i.e., $a = 90$ μm (see figures 4.3 and 4.8b). For small thermal penetration depths, only the hot spots are important, because the heating contribution of wide portions is negligible. As such, the line half-width $a = 5$ μm. These igniter half-widths are valid for the following ignition delay times:

Case 1: $a = 5$ μm $\Rightarrow$ $t \geq 1.25$ ms.

Case 2: $a = 90$ μm $\Rightarrow$ $t \geq 405$ ms.

Although this represents a gross simplification of the actual thermal behavior of the device, it is useful in describing its overall behavior.

4.4 Experimental Methodology

A total of 383 drop-coated, bottom-side pyroMEMS igniters were tested in this study. A summary table breaking down the different layouts, substrate materials and binder contents is given in table 4.3.

4.4.1 Experimental Setup

A square voltage pulse was applied to the igniter chip using a function generator (HP33120A) coupled to a high-speed power amplifier (NF Electronic Instruments 4015). The range of input

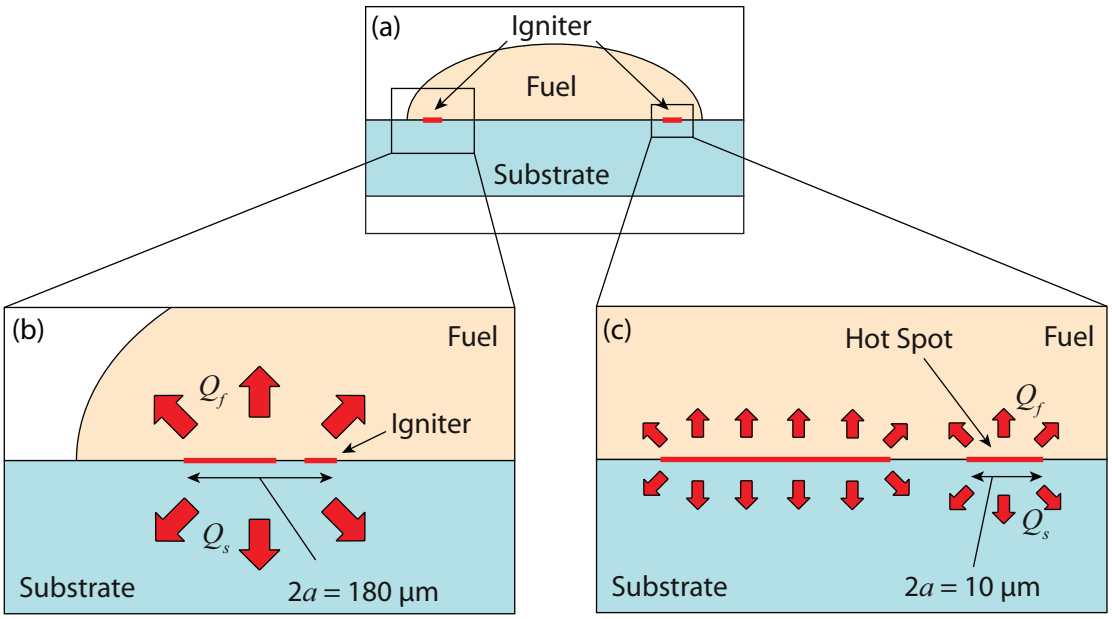

Figure 4.8: Cross-section sketch of the (a) hot spot igniter consisting of two concentric rings (line widths: wide portion = 100 μm, hot spot = 10 μm and gap size = 70 μm), showing the two different thermal behaviors depending on the ignition delay time: (b) the situation where the thermal penetration depth δ is much larger than the spacing between the heaters and (c) the case where the thermal penetration depth is smaller than the spacing.

Table 4.3: Bottom-side igniter parameter summary table.

Substrate	Layout	Binder (%)	# of devices
Borosilicate Glass	Meander	5	27
		10	23
		20	25
	Annular	10	47
		20	48
	Hot Spot	5	25
		10	82
		20	81
Polyimide Foil	Meander	5	11
	Hot Spot	5	14
		10	19
Borosilicate Glass (Closed Chamber)	Hot Spot	5	15
		10	10

voltages used were limited by the devices themselves: if the voltages were too low, the fuel did not ignite and if they were too high, the igniters themselves failed (see table 4.4).

Table 4.4: Bottom-side igniter input power range.

		Voltage (V)		Power (W)	
Layout	Substrate	min	max	min	max
Meander	Borosilicate Glass	32.0	86.0	1.39	12.58
	Polyimide Foil	16.0	61.0	0.24	4.08
Annular	Borosilicate Glass	15.0	85.0	0.78	18.00
	Polyimide Foil	Not Fabricated			
Hot spot	Borosilicate Glass	16.0	35.0	0.85	2.67
	Polyimide Foil	12.0	18.0	0.28	0.58

Two high-speed digital multimeters (Agilent 34410A) measured the voltage and current passing though the igniter to determine the input power (figure 4.9). Simultaneously, a high-speed framing camera (Vision Research Phantom v210) mounted onto a stereomicroscope (Leica MZ8) acquired a video of the combustion process at up to 10,000 frames per second. All of the measurement devices were computer controlled and triggered via GPIB using a custom MATLAB script. The trigger timing was verified by comparing the ignition delay times obtained from the sharp drops in input power—spike in temperature/resistance due to ignition—observed in the power traces (e.g., 535.8 ± 0.5 ms in figure 4.9) with the high-speed videos (535.4 ± 0.1 ms). All the experiments were performed in air.

A randomized block experimental design was used to remove any experimental bias due to uncontrolled factors (i.e., fuel coverage and propellant mass). The experiments were blocked by binder mass fraction to ensure that each fuel mixture spanned the full range of input power levels. The burning rate was approximated by averaging the minimum and maximum flame path lengths from the combustion videos and dividing by the combustion duration.

4.4.2 Statistical Analysis

Goodness of Fit

The experimental results for each igniter layout were fitted to the regression models developed in previously. The goodness of fit of the regression curves was estimated two different ways [53]:

1. The regression residual should be normally distributed. The “normality” of the residual was estimated using the Lilliefors normality test [54], which is available in MATLAB.

2. The residual plot is visually inspected to see if the functional form of the regression curve is accurate. The regression residual ϵ_i is taken as the difference between the random

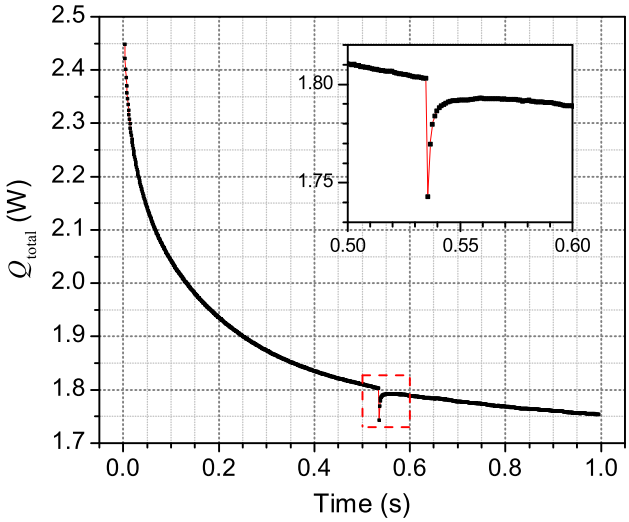

Figure 4.9: Typical input power profile with magnification of fuel ignition at 535.8 ± 0.5 ms (inset). The sharp drop in power was the result of a spike in igniter resistance due to the fuel ignition.

variable—the measured ignition delay time Δt_I—and its fitted value. The residual should be completely independent of the independent variable—in our case, the total input power Q_{total}.

Analysis of Covariance

Further statistical analysis of the regression results involve analysis of covariance of the residual against the other independent variables, such as fuel mass and binder mass fraction. In an analysis of covariance, the data is slit into a number of groups based on a qualitative variable—in our case, binder mass fraction—and individual linear regression fits are performed on each data set against a new independent variable—fuel mass. Then the means and intercepts of the different levels of binder content are compared to one another, starting with the most general situation where the slopes and mean values are all non-zero. Then, one at a time, we eliminate degrees of freedom—i.e., assume that the slopes are all the same, or the means are all the same—and determine if these changes are statistically significant. For more details, see [53].

4.5 Ignition Results

In this section, the effect of the different experimental variables—input power, layout, substrate, binder content and fuel mass—on the ignition delay time will be presented. The results are organized as follows: first the results for igniters on borosilicate glass will be presented for each igniter, then polyimide and finally for the closed chambers. The regression analysis first

took into account the effect of input power and then the effects of binder and fuel mass were investigated by analysis of covariance of the regression residual.

4.5.1 Borosilicate Glass Substrate

Meander Layout

Ignition delay times Δt_I versus input power Q_{total} for the meander igniters are shown in figure 4.10. Based on equation (4.11), the experimental data was fitted to a linear regression model of the form

$$y_i = b + m \cdot x_i + \epsilon_i \tag{4.27}$$

where $y_i = \log_{10}(\Delta t_I)$, $x_i = \log_{10}(Q_{total})$, $b = \log_{10}(K_1)$, $m = K_2$ and ϵ_i is the linearized regression residual. Only data with ignition delay times less than 0.4 s were used to fit the regression line—as required by 4.15. The resultant fit was in good agreement with the predicted coefficients, given that the thermal properties of the fuel were order of magnitude estimates (see Table 4.5). The regression residual was normally distributed and independent of input power for ignition delay times less than 0.4 s—i.e., $Q_{total} > 2$ W (see figure 4.10 inset). For lower input powers, the ignition delay times diverged from the fit due to the finite thickness of the glass substrate—as predicted by the model. The regression—taking into account only input power—explained nearly 99 % (R^2) of the total variance in the fit region. The standard error of the residual (s_ϵ) gives a prediction of the unexplained scatter in ignition delay time one can expect using the meandering igniter, which was less than 10 %. No estimation of the thermal conductivity or thermal diffusivity was possible, since there are two unknowns (k_f and α_f) and only one equation, (4.9).

Table 4.5: Meander igniter regression analysis (glass substrate)

		Regression		
Parameter	Prediction	Degrees of Freedom	Mean	Standard Error
$b = \log_{10}(K_1)$	~ 0.1	1	0.38	0.02
$m = K_2$	-2	1	-2.13	0.03
ϵ_i	N/A	73	0	0.04
$R^2 = 98.84$ %				
$s_\epsilon = +9.8$ %, -8.9 %				

An analysis of covariance on the linearized residual ϵ_i versus fuel mass and binder content indicated a statistically significant effect due to fuel mass, indicating the finite thickness of the fuel drop did have an effect—albeit small—on the ignition delay time. This effect was

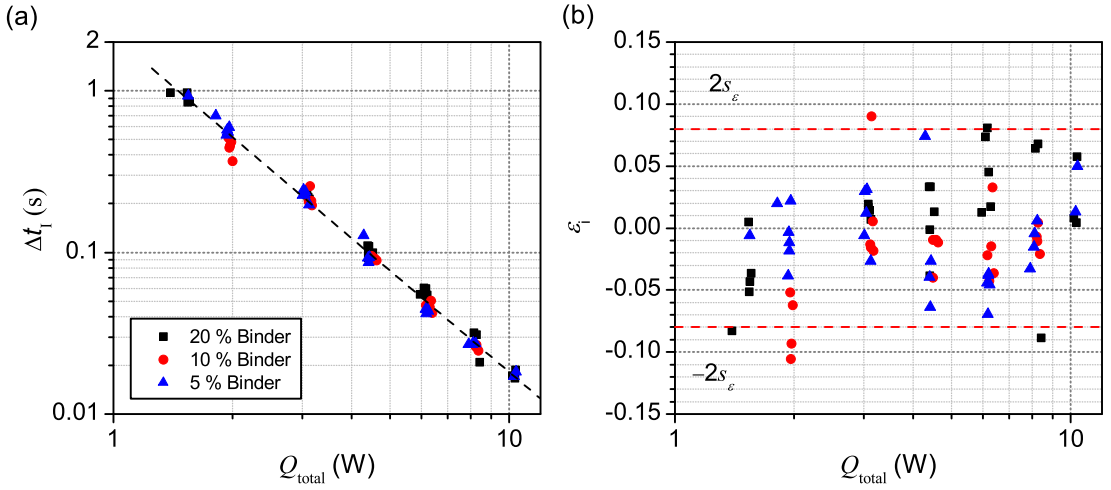

Figure 4.10: (a) Ignition delay vs. input power (glass substrate, meander igniter). (b) Linearized regression residual over the fit region.

investigated by plotting the linearized residual against fuel mass (see figure 4.11). For small fuel drops (to the left of the red dotted line), the residual increased with increasing fuel, while for larger fuel drops, there was less of an effect. This is consistent with the premise that the smaller fuel drops have thicknesses less than the thermal penetration depths during the ignition process, while the larger drops can be considered infinitely thick. The cut-off appeared to be around 300 μg of fuel. The fuel mass accounted for 20 % percent of the unexplained variance, or ~ 0.1 % of the total variance, and therefore relatively minor compared to the effect of input power. Binder content had no statistically significant effect on the ignition delay time (P-value > 1 %).

Annular Layout

Ignition delay times Δt_I versus the inverse total input power Q_{total}^{-1} for the annular igniter are shown in figure 4.12. Based on equation (4.23), the experimental data was fitted to a linear regression model of the form

$$y_i = b + m \cdot \hat{x}_i + \epsilon_i \tag{4.28}$$

where $y_i = \ln(\Delta t_I)$, $\hat{x}_i = Q_{total}^{-1}$, $b = \ln(K_3)$, $m = K_4$ and ϵ_i is the linearized regression residual. Two different linear fit regions—indicated with dashed black lines—were found near the ignition delay times predicted by the model. The first occurred for ignition delays between 0.5 and 5 s, with associated thermal penetration depths between 200 and 700 μm. As such, it was linked with the case where the three lines acted as a single line of half-width $a = 125$ μm. The second linear region occurred between 8 and 100 ms—or for thermal penetration depths

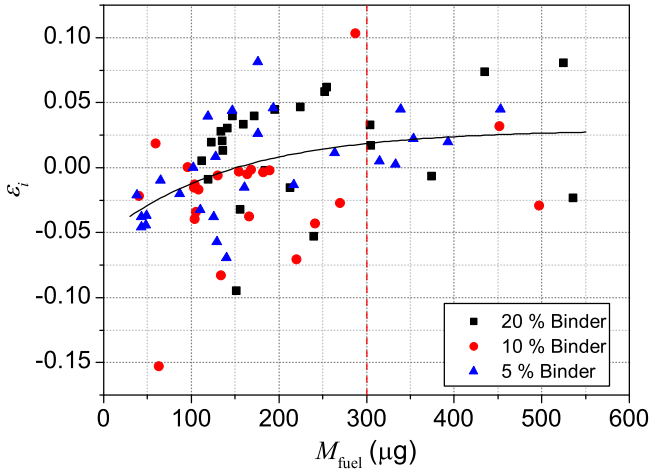

Figure 4.11: Meander regression residual vs. fuel mass (glass substrate). To the left of the red dotted line, the residual slowly increased, while to the right, it stabilized.

between 30 and 100 μm—which is in good agreement with the situation where each line is acting independently (for a half-width $a = 25$ μm).

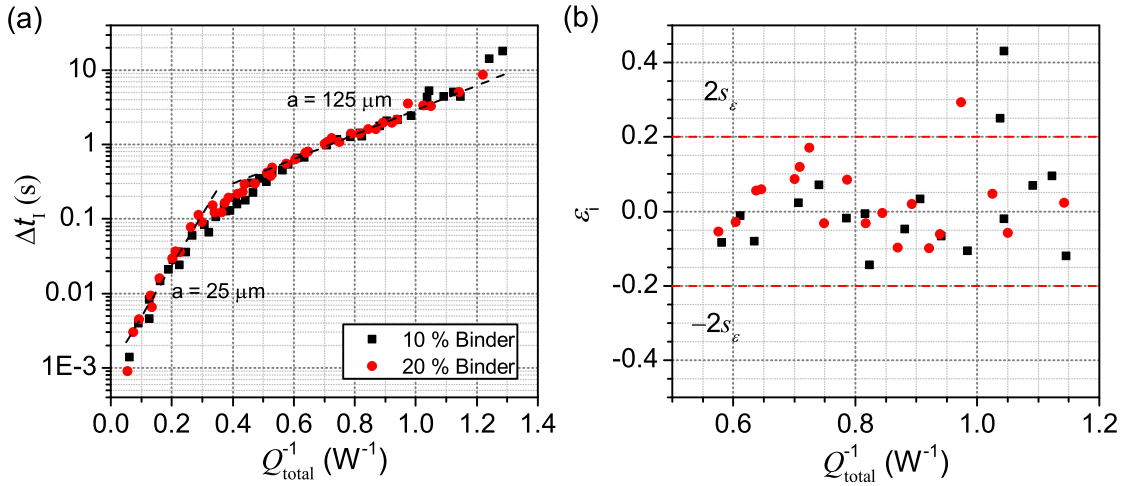

Figure 4.12: (a) Ignition delay vs. the reciprocal of the input power (glass substrate, annular igniter). (b) Linearized regression residual over the fit region ($a = 125$ μm).

The fitted coefficients K_3 and K_4 for both fit regions were of the same order of magnitude as the predicted values (see Tables 4.6 and 4.7). The resultant fit for $a = 125$ μm—$R^2 = 97.19$ %—in slightly better agreement than the $a = 25$ μm fit—$R^2 = 91.64$ %, although the difference is relatively small. The estimated uncertainty in the ignition delay times s_ϵ for both fits was ~ 10 % for $a = 125$ μm and ~ 25 % for $a = 25$ μm. The larger uncertainty in the $a = 25$ μm fit

region may be due to its smaller extent in terms of inverse input power levels—from 0.13 to 0.3 W^{-1}—vs. the $a = 125$ μm fit region—from 0.6 to 1 W^{-1}.

Table 4.6: Annular igniter regression analysis (glass substrate, $a = 125$ μm).

		Regression		
Parameter	Prediction	Degrees of Freedom	Mean	Standard Error
$\ln(K_3)$	~ -4.7	1	-2.59	0.11
K_4	~ 3.9	1	3.65	0.12
$\ln(\epsilon_i)$	N/A	30	0	0.10
$R^2 = 97.19$ %				
$s_\epsilon = +10.4$ %, -9.4 %				

Table 4.7: Annular igniter regression analysis (glass substrate, $a = 25$ μm).

		Regression		
Parameter	Prediction	Degrees of Freedom	Mean	Standard Error
$\ln(K_3)$	~ -7.9	1	-6.3	0.2
K_4	~ 10.6	1	12.7	1.0
$\ln(\epsilon_i)$	N/A	14	0	0.2
$R^2 = 91.64$ %				
$s_\epsilon = +25.3$ %, -20.2 %				

Analysis of covariance found that the regression residuals for both fit regions were independent of binder content and fuel mass (see figures 4.13a and b). There was no correlation between the residual and the fuel mass for the annular igniters because all the fuel drops tested laid in the “large drop” category—i.e., above 300 μg.

Hot Spot Layout

Lastly, the same annular regression fit was applied to the hot spot ignition data (see figure 4.14). Again, the multiplicative residual in equation (4.23) was justified a posteriori by the constant, normally-distributed residual (see Figure 4.14 inset).

Two different linear fit regions were found. The first occurred for ignition delays between 0.4 and 4 s, with associated thermal penetration depths between 200 and 630 μm. As such we associated it with the case where the two lines acted as a single line of half-width, $a = 90$ μm. The second linear region occurred between 0.0001 and 0.03 s—or for thermal penetration depths between 3 and 50 μm—which is in good agreement with the situation where the hot spots are acting independently (for a half-width, $a = 5$ μm). The resultant fit for the $a = 90$ μm region was very good ($R^2 = 92.81$ %), while that of the $a = 5$ μm region ($R^2 = 77.08$ %) was less so due to large uncertainty in the y-intercept (K_3) for the $a = 5$ μm fit region (see Tables 4.8

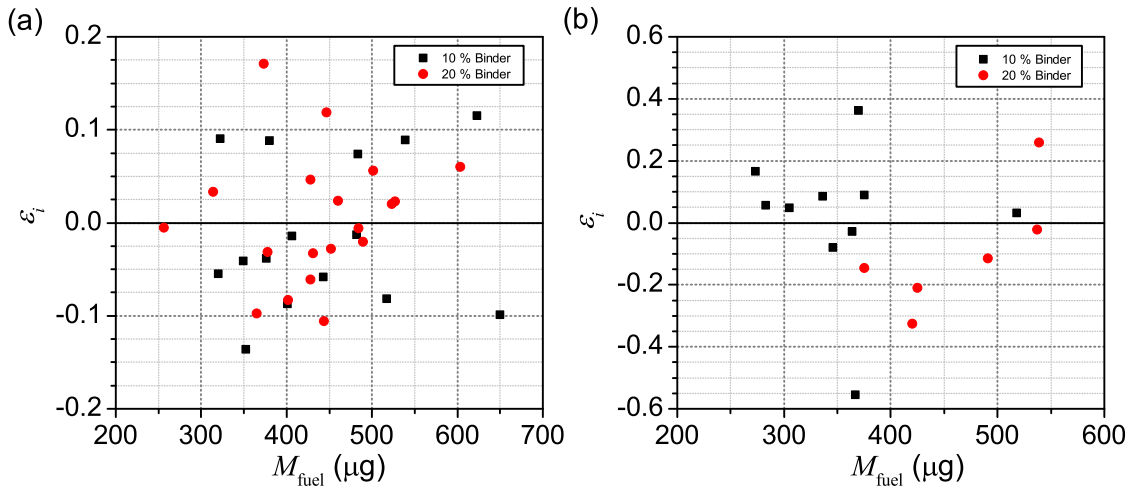

Figure 4.13: Annular regression residual vs. fuel mass for the (a) $a = 125$ μm and (b) $a = 25$ μm fit regions (glass substrate).

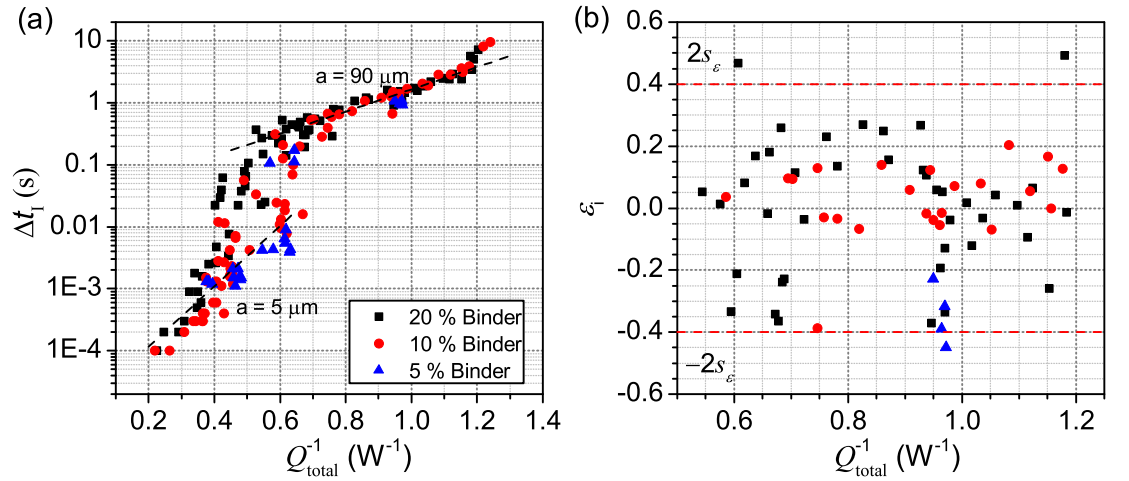

Figure 4.14: (a) Ignition delay vs. the reciprocal of the input power (glass substrate, hot spot igniter). (b) Linearized regression residual over the fit region ($a = 90$ μm).

and 4.9).

Table 4.8: Hot spot igniter regression analysis (glass substrate, $a = 90$ μm).

		Regression		
Parameter	Prediction	Degrees of Freedom	Mean	Standard Error
$\ln(K_3)$	~ -5.3	1	-3.60	0.13
K_4	~ 3.8	1	4.10	0.14
$\ln(\epsilon_i)$	N/A	66	0	0.2
$R^2 = 92.81$ %				
$s_\epsilon = +23.2$ %, -18.8 %				

Table 4.9: Hot spot igniter regression analysis (glass substrate, $a = 5$ μm).

		Regression		
Parameter	Prediction	Degrees of Freedom	Mean	Standard Error
$\ln(K_3)$	~ -11.1	1	-13.1	0.6
K_4	~ 7.8	1	16.2	1.5
$\ln(\epsilon_i)$	N/A	32	0	0.7
$R^2 = 77.08$ %				
$s_\epsilon = +105.3$ %, -51.3 %				

The analysis of covariance on the regression residuals found that the residual for the $a = 90$ μm fit region showed no effect of binder content and an asymptotically increasing small positive correlation with fuel mass—as with the meander layout (see figure 4.15a). The $a = 5$ μm fit region showed no effect of fuel mass, but a linearly increasing dependence due to binder mass fraction (see figure 4.15b and 4.16). No other igniters exhibited this behavior. This is believed to be due to the very fast ignition delay times—from 0.1 to 10 ms—encountered in this regime: at these small delay times, the chemical reaction induction period may play a non-negligible role in the overall ignition delay time.

Estimation of the Fuel Thermal Properties

Using the annular and hot spot regression coefficients, it was possible to estimate the thermal conductivity and thermal diffusivity of the fuel. The thermal diffusivity was obtained simply by inverting equation (4.24):

$$\alpha_f = \frac{Ca^2}{4K_3 \exp(2)} \tag{4.29}$$

whereas the thermal conductivity was obtained following an iterative process, whereby, (1) the

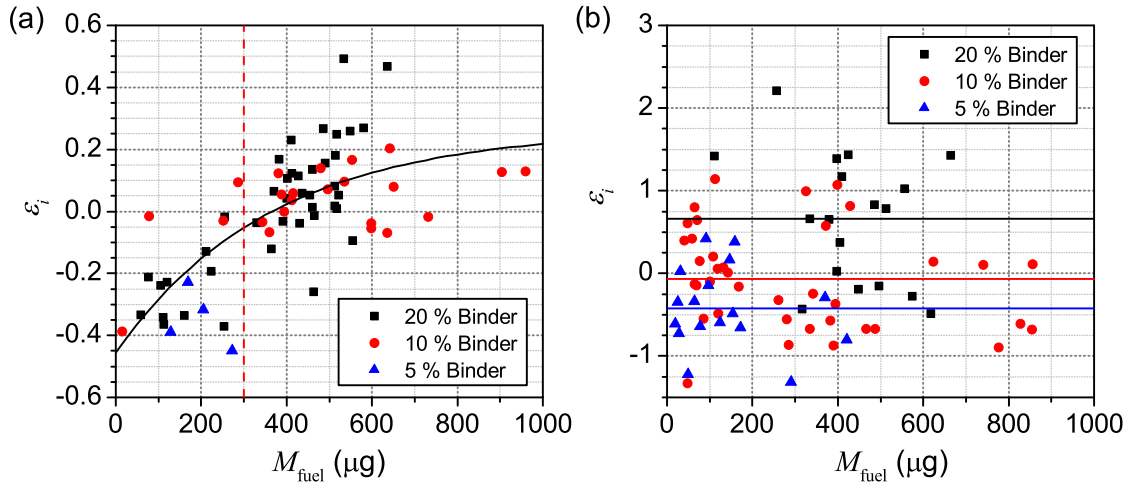

Figure 4.15: Hot spot regression residual vs. fuel mass for the (a) $a = 90$ μm and (b) $a = 5$ μm fit regions (glass substrate).

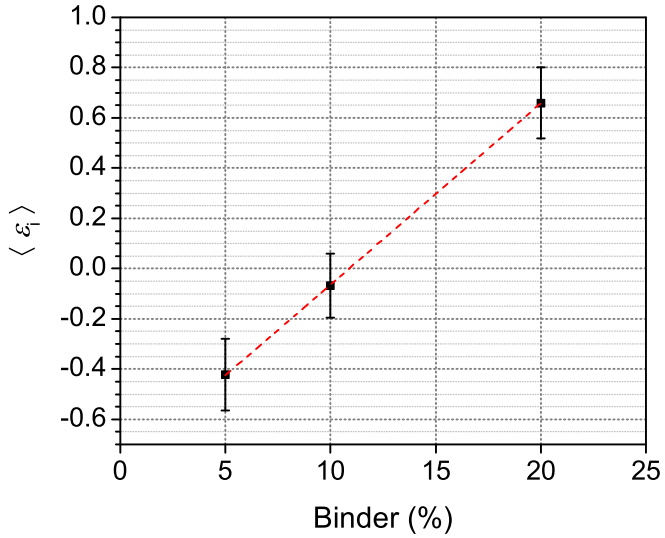

Figure 4.16: Mean hot spot regression residual vs. binder mass fraction (glass substrate, $a = 5$ μm fit region).

input power ratio η_A is calculated from the initial guesses of α_f and k_f (see equation (4.22)); and, (2) k_f is calculated from η_A (4.25), and the process is repeated until convergence:

$$\eta_A = \left[1 + \frac{k_s}{k_f}\frac{\left[2+\ln\left(4\alpha_f t/Ca^2\right)\right]}{\left[2+\ln\left(4\alpha_s t/Ca^2\right)\right]}\right]^{-1} \tag{4.30}$$

$$k_f = \frac{K_4 \eta_A a}{\pi S_A \Delta T_I} \tag{4.31}$$

The iterative process was found to converge to the same final value for any reasonable initial guess of k_f (see figure 4.17). The estimated thermal conductivity and thermal diffusivity of the fuel, based on the four fit regions is given in table 4.10. The values of thermal conductivity—based on the slope of the regression fits—were in very good agreement with each other and with the theoretical, order of magnitude estimate used based on organic compounds. However, the estimated thermal diffusivity—based on the y-intercept—was about an order of magnitude smaller than expected. The value obtained for the $a = 5$ μm fit region was not representative because of the effect of binder content on the y-intercept. Nevertheless, the theoretical order-of-magnitude values were very rough estimates of the thermal properties of the fuel, as such, the values obtained from the regression residuals were relatively good.

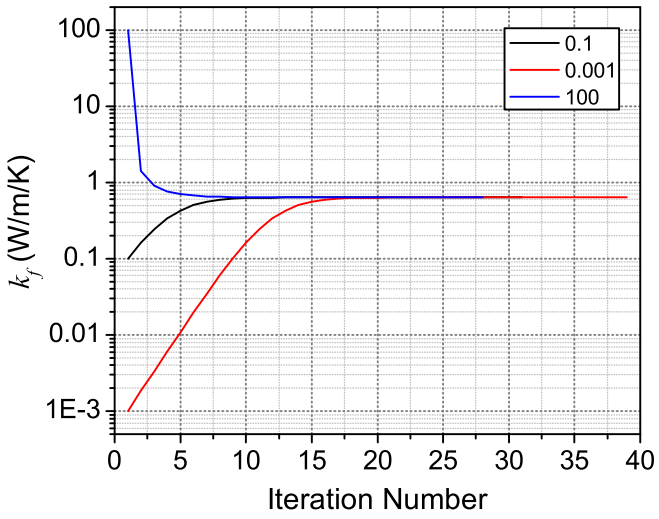

Figure 4.17: Iteration convergence of the fuel thermal conductivity k_f for different initial guesses ($a = 125$ μm fit region).

Table 4.10: Estimated thermal properties of the fuel mixture.

Layout	Fit region	k_f (W/(m · K))	α_f (mm^2/s)
Annular	$a = 125\ \mu$m	0.267 ± 0.009	0.012 ± 0.001
	$a = 25\ \mu$m	0.40 ± 0.03	0.020 ± 0.005
Hot spot	$a = 90\ \mu$m	0.338 ± 0.012	0.018 ± 0.002
	$a = 5\ \mu$m	0.38 ± 0.04	5 ± 4
Mean		0.35 ± 0.06	0.017 ± 0.004
Theoretical Prediction		~ 0.1	~ 0.1

4.5.2 Polyimide Substrate

In this section, we will present the ignition results for the igniters patterned on polyimide substrates. The motivation behind using the polymer substrate was to lower the fraction of input power dissipated by the substrate and therefore reduce the overall power consumption of the pyroMEMS igniters.

Meander Layout

We also investigated the effect of the substrate material on the ignition delay times for the meander layout (figure 4.18). Based on the theoretical model—i.e., equation (4.6)—decreasing the thermal conductivity and thermal diffusivity of the substrate will decrease the power required for ignition by a factor of 3.2. Experimentally, substituting the substrate material reduced the required input power for ignition by a factor of 3.8, yielding a minimum input power of ~ 250 mW. This is in relatively good agreement with the theoretical prediction given that the uncertainty in the thermal properties of the fuel.

Hot Spot Layout

For the hot spot layout, the effect of the substrate on the ignition power is different, although the overall effect was a decrease in ignition power (figure 4.19). Based on the annular model (see equations (4.24) and (4.25)), changing the substrate material—i.e., η_A—decreases the fit region slope K_3 by a factor of 2.8. The slope of the $a = 90\ \mu$m fit region was found to decrease from 4.10 to 0.93—or by a factor of 4.4. Again, the theoretical prediction underestimated the change—due to the uncertainty in the thermal properties of the fuel. The y-intercept did not change by a statistically significant margin—as expected.

4.5.3 Closed Chambers

A total of 25 hot spot igniters fabricated on borosilicate glass were encapsulated with silicon combustion chambers and tested. Three different chamber heights were tested: 525, 1050 and

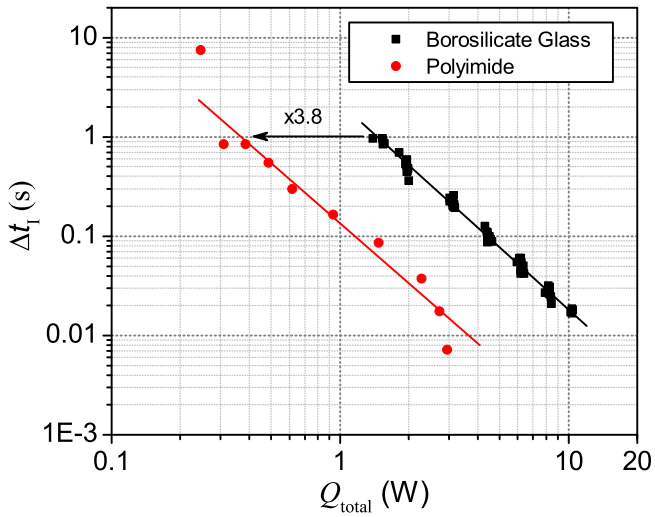

Figure 4.18: Ignition delay vs. input power on borosilicate glass and polyimide substrates (Meander layout).

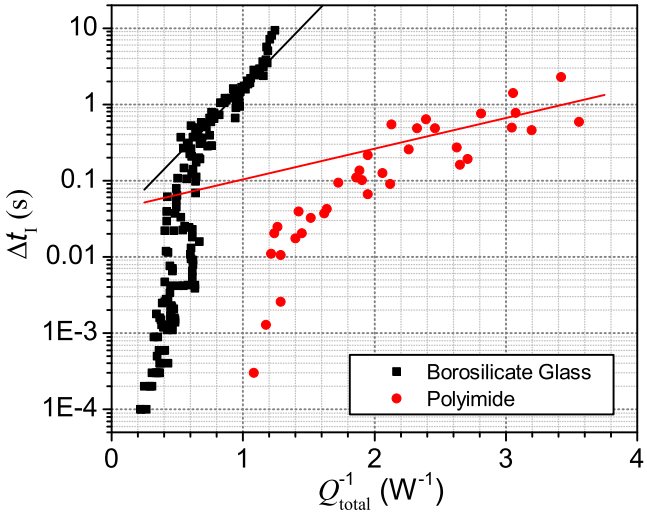

Figure 4.19: Ignition delay vs. input power on borosilicate glass and polyimide substrates (Hot spot layout). The dotted lines represent the fit regions for $a = 90$ μm.

1575 μm—all with the same diameter of 2.3 mm. A summary table of the results is given in table 4.11) breaking down the results in terms of successful ignition and combustion (success), failed ignition (smoldering) and devices where the combustion chamber ruptured (chamber failure).

Table 4.11: Summary of closed chamber results (glass substrate, hot spot igniter, 2.3 mm chamber diameter).

		Result				
Chamber Height (μm)	Binder (%)	success	/	smoldering	/	chamber failure
525	5	2	/	3	/	0
	10	0	/	1	/	2
1050	5	3	/	2	/	0
	10	3	/	0	/	0
1575	5	4	/	1	/	0
	10	5	/	0	/	0

The goal of these tests was to determine if there was a difference in ignition or combustion behavior when the fuel underwent constant pressure (no chamber) or constant volume (closed chamber) combustion. The ignition delay time vs. the reciprocal of the input power is plotted in figure 4.20—with the unencapsulated igniters for reference. Encapsulating the igniters within closed combustion chambers did not significantly affect the ignition delay time; however, adding the silicon chambers increased the minimum power required for fuel ignition to occur—~ 1.3 W vs. ~ 0.85 W without the silicon chambers. Below this input power level, the fuel is slowly consumed by smoldering. This is because the silicon chambers act as heat sinks, requiring higher input power levels to achieve fuel ignition. Unfortunately, the simple analytical models developed in this chapter do not take this effect into account.

4.6 Combustion Results

The combustion results are presented as follows: first the base case where fuel peeling and ejection occurs will be presented. The effect of binder content and input power level on the incidence and severity of the peeling failure are presented. Next, the hot spot layout is presented exhibiting little to no fuel ejection. The minimum fuel mass required for self-sustained combustion is determined as well as the average burning rate. Finally, the effect of confinement—adding a closed chamber—on the burning rate will be analyzed.

4.6.1 Meander and Annular Layouts: Peeling and Fuel Ejection

The combustion behavior of the different igniter layouts was investigated in order to better understand fuel peeling and ejection in bottom-side pyroMEMS igniters.

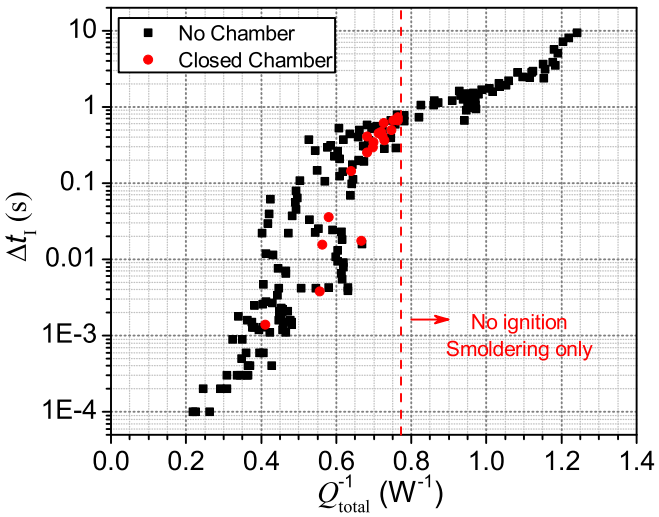

Figure 4.20: Ignition delay vs. input power with and without a closed combustion chamber (glass substrates, hot spot layout). The dotted line represents the cut-off power below which no combustion was observed for the closed chamber devices.

For the meander layout, at lower input power levels and binder content, ignition of the fuel caused explosive ejection of the propellant drop within less than 1 ms (figure 4.21). However, when the heat flux and/or binder mass fraction were increased, stable deflagration waves were observed (figure 4.22). Nevertheless, a small amount of peeling in the center of the drop could not be eliminated. This was because the meandering igniter also generated a vertical thermal gradient, which caused the expanding flame front to undercut the central fuel mound.

Fuel peeling was quantified by measuring the time delay between fuel ignition and ejection—which was taken as the time when a majority of the fuel drop leaves the surface of the igniter (i.e., Figure 4.21b). Figure 4.23 clearly shows that binder and input power—within the ranges tested—had comparable effects in mitigating fuel ejection. Increasing the input power level by roughly an order of magnitude—from 1.5 to 10 W—delayed fuel ejection by a factor of 10, while doubling the fuel mixture's binder mass fraction—from 5 to 10 and from 10 to 20—delayed fuel ejection by a factor of 3. However, the best results obtained with 5 % binder were comparable to the worst ones using 20 % binder. An analysis of covariance found negligible interaction effects between input power and binder content—resulting parallel fits for all binder mass fractions. Similar results were obtained using the annular igniters.

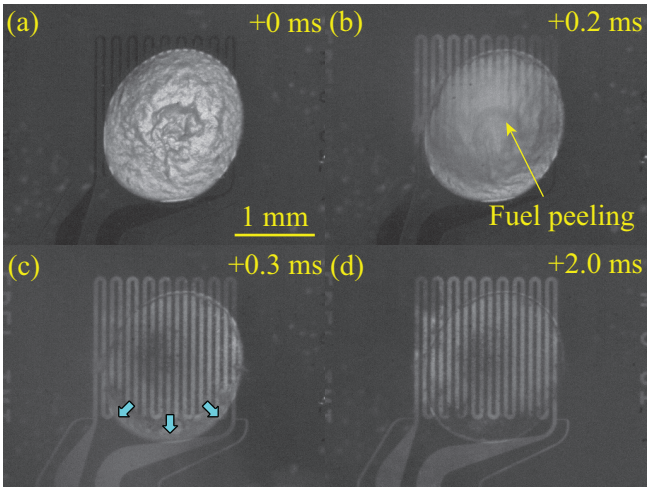

Figure 4.21: High-speed video frames of a “failed” combustion event (glass substrate, meander igniter, Q_{total} = 1.5 W, 5 % binder): (a) before ignition, (b) ignition and rapid fuel ejection, (c) combustion of residual fuel and (d) post-combustion (note: minimal combustion residue on igniter). A time stamp is given in the top right corner of each frame.

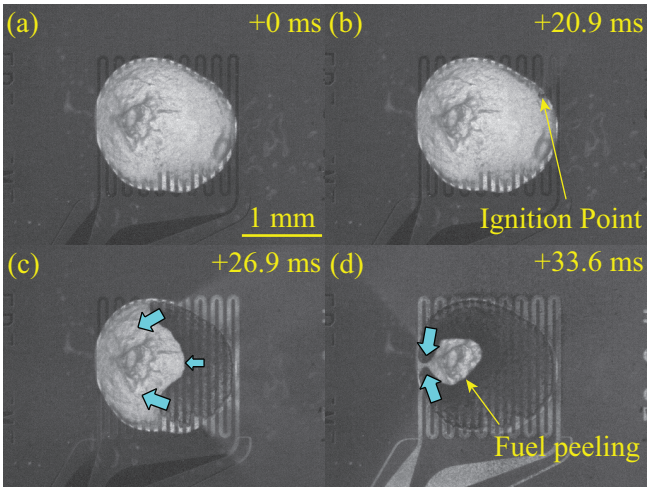

Figure 4.22: High-speed video frames of a “successful” combustion event (glass substrate, meander igniter, Q_{total} = 8.4 W, 20 % binder) : (a) before ignition, (b) propellant ignition, (c) flame spreading—preferentially around the periphery—and (d) pinching of peripheral flame fronts and residual fuel peeling. A time stamp is given in the top right corner of each frame.

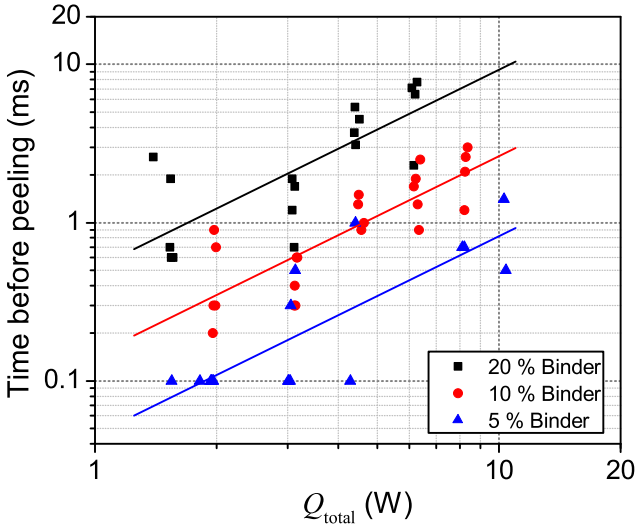

Figure 4.23: The time before ejection vs. input power and binder mass fraction (glass substrate, meander layout).

4.6.2 Hot Spot Layout: Steady Combustion

Long vs. Short Ignition Delay Times

The hot spot layout—combining annular layout geometry and hot spots to limit the heated zone to a small area—successfully prevented the onset of fuel peeling and ejection. Depending on the ignition delay time (i.e., thermal penetration depth), two different combustion regimes were observed. For the long ignition delay times associated with the $a = 90$ μm fit region, large darkened smoldering areas were visible around the igniters before the onset of steady combustion (see figure 4.24). Ignition always occurred from a single point and spread faster over the igniter than through the center. For the shorter delay times associated with the $a = 5$ μm fit region, there were no visible smoldering around the igniters prior to ignition; instead, small amounts of fuel peeling were associated with the onset of combustion (see figure 4.25). Ignition originated from one or more hot spots and spread uniformly across the fuel drop.

Minimum Fuel Mass for Self-Sustained Combustion

Combustion behavior for the hot spot igniters was investigated to ascertain if the deflagration waves can be self-sustaining at these scales. A minimum propellant thickness was needed for the heat generated by the deflagration wave to sustain a steady flame front. Failing this, the combustion front was quenched due to excessive heat losses to the substrate. Although a critical fuel thickness could not be extracted in this study—due to the irregular shape of the propellant drops—a relationship between fuel mass and flame quenching was found. Comparing the fuel masses for the self-sustained and quenched combustion fronts, we found

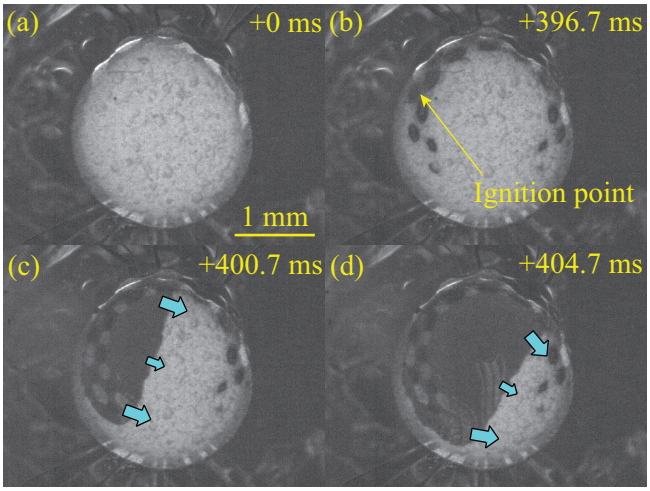

Figure 4.24: High-speed video frames of a typical combustion event (glass substrate, hot spot igniter, $a = 90$ μm fit region, $Q_{total} = 1.3$ W $\left(Q_{total}^{-1} = 0.77\ \text{W}^{-1}\right)$, 10 % binder): (a) when power turned on, (b) emergence of a single flame kernel among the smoldering hot spots, (c) and (d) spreading of flame front—preferentially over the igniter. A time stamp is given in the top right corner of each frame.

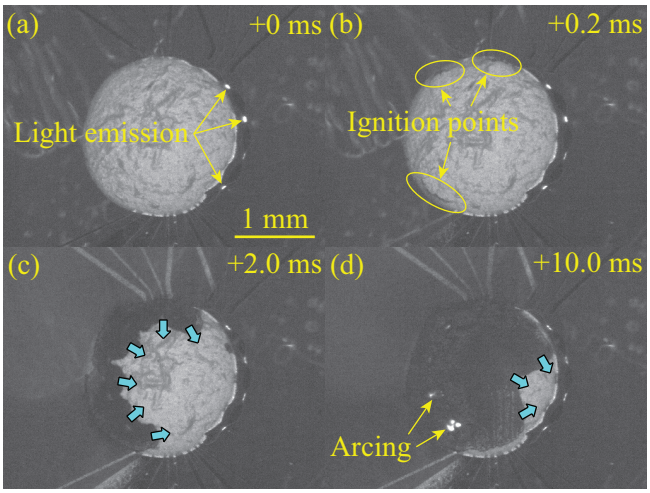

Figure 4.25: High-speed video frames of a typical combustion event (glass substrate, hot spot igniter, $a = 5$ μm fit region, $Q_{total} = 1.5$ W $\left(Q_{total}^{-1} = 0.67\ \text{W}^{-1}\right)$, 5 % binder): (a) when power turned on (light emission at hot spots), (b) emergence of multiple flame kernels (note: no prior smoldering visible), (c) spreading of flame front and (d) arcing and failure of igniter. A time stamp is given in the top right corner of each frame.

that incomplete combustion occurred in fuel drops that weighed less than roughly 100 μg (see Table 4.12). This was true for both fit regions. Interestingly, this minimum fuel mass was independent of binder mass fraction: one would expect the minimum mass for self-sustained combustion to depend on the chemical kinetics of the fuel mixture, which is a function of the binder content of the fuel.

Table 4.12: Effect of fuel mass on combustion quenching (Hot spot layout).

Combustion Behavior	# devices	Fuel Mass (μg)
Steady	59	124 ± 15
Incomplete	35	47 ± 6

Burning Rate

The average burning rate was determined by estimating the flame front path length and dividing it by the combustion duration—both of which were obtained from the high-speed videos. Figure 4.26 shows that the burning rate for the self-sustained deflagration waves. The burning rate first decreased exponentially with increasing input power (a = 90 μm regime) before stabilizing at a constant value (a = 5 μm regime). Figure 4.26b shows a linear relationship between the stabilized burning rate and the binder content—over the limited range of binder mass fractions tested.

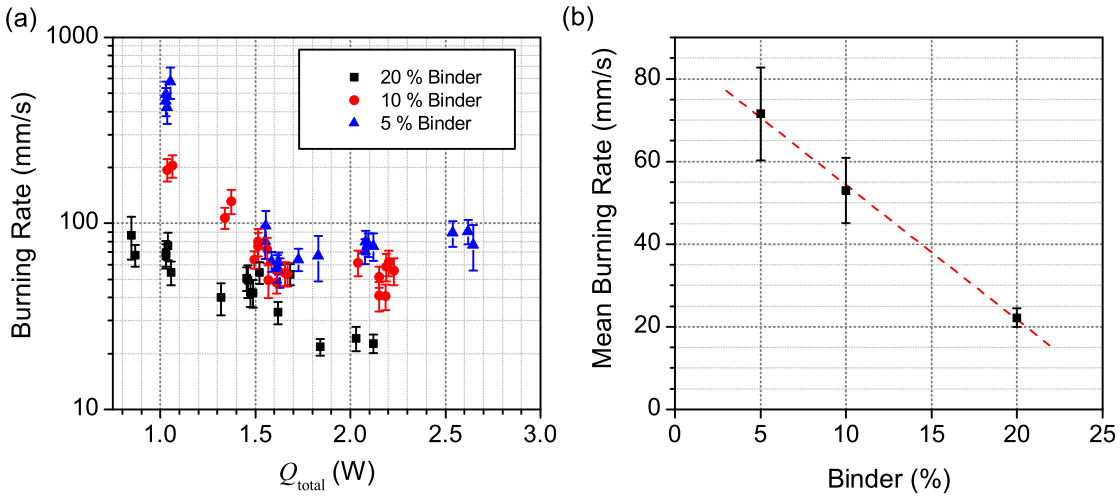

Figure 4.26: (a) Burning rate vs. input power and binder content (Hot spot layout; steady combustion only). (b) Mean asymptotic burning rate vs. binder content.

Burning rates on the order of centimeters per second indicated combustion occurred via subsonic deflagration—which propagates via heat diffusion from the flame front into the adjacent unburned fuel. As such, the higher burning rates at lower heat fluxes were due to the more extensive pre-heating of the fuel charges—as indicated by the large darkened "heat affected" zones. Burning rates for macroscopic samples of K-DNBF are not available in the

literature, since they are not relevant to their main application as initiators. However, K-DNBF is commonly believed to detonate under "normal" conditions—that is for larger fuel masses, on the order of milligrams or more. The burning rates were constant in the $a = 5$ μm regime because the fuel initiated before any significant heating of the surrounding fuel occurred.

4.6.3 Closed Chambers

Due to the confinement caused by encapsulating the igniter and fuel in a closed chamber, the pressure and temperature was allowed to build up inside the chamber and become incandescent (see figure 4.27). As opposed to the open igniters—where combustion occurred under constant pressure conditions—combustion in the closed chambers was constant volume, resulting in much higher combustion pressures and temperatures.

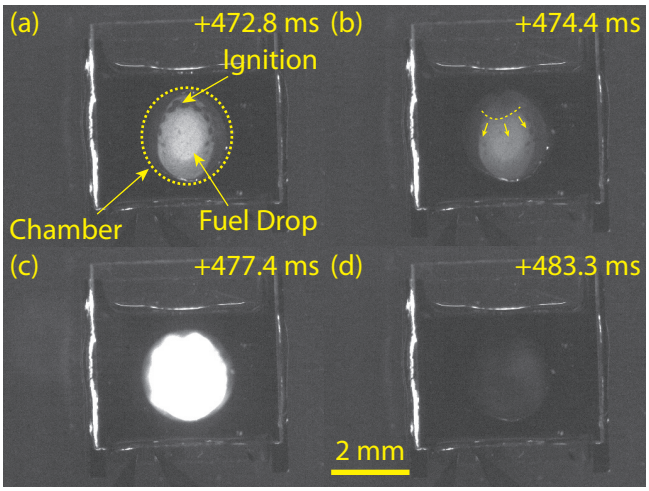

Figure 4.27: High-speed video frames of a typical closed-chamber combustion event (glass substrate, annular igniter, $Q_{total} = 1.39$ W $\left(Q_{total}^{-1} = 0.72 \text{ W}^{-1}\right)$, 10 % binder): (a) onset of ignition, (b) smooth combustion spreading (note: chamber filling with smoke), (c) at maximum luminosity and (d) at the end of combustion. A time stamp is given in the top right corner of each frame.

4.7 Discussion

4.7.1 Ignition

The following conclusions can be made about the ignition behavior of the bottom-side igniters:

1. *Analytical fits.* The analytical fits were in very good agreement with the experimental data:
    - The meander and annular/hot spot igniters were found to obey distinct analytical models based on their geometries—neither of which were simple exponential

decay models. The success of the analytical models—goodness of fit—was based on the fact that the regression residuals were normally distributed and uncorrelated with the independent variable (input power). They also yielded thermal property values in agreement with each other and close to the estimated order-of-magnitude values for organic compounds assumed at the outset (see table 4.10).

- The annular model successfully predicted two linear fit regions for both the annular and hot spot igniters based on the igniter geometries and the thermal penetration depth of the heated zone. In particular, it successfully predicted the sudden drop in ignition delay times for the hot spot igniter at higher input power levels due to the presence of the narrow hot spots—although not its exact magnitude.

2. *Input power.* The input power was by far (> 90 %) the most important source of variance affecting the ignition delay times. Taking only input power into account yielded regression fits with standard errors on the order of about 10 to 25 %—not withstanding the $a = 5$ μm fit region for the hot spot igniter. This value is much lower than those reported by Rossi *et al.* [15] and Zhang *et al.* [28], because poor thermal contact was not an issue with bottom-side igniters, as opposed to their devices.

3. *Binder mass fraction.* Binder mass fraction had no statistically significant effect on ignition delay time except for the hot spot ($a = 5$ μm) fit region, where the binder content was positively correlated with the ignition delay time. Due to the very short ignition delay times (< 1 ms), it was assumed that the fuel's short induction period was no longer negligible and that the slower chemical kinetics at higher binder mass fractions delayed the fuel ignition.

4. *Fuel mass.* Fuel mass fraction played a minor—but statistically significant—role in the ignition delay times. The ignition delay increased slightly with fuel mass until a critical value. After this critical value, the effect of fuel mass disappeared. This small increase in delay time was due to the increased thickness of the fuel near the igniters. Fuel drop thickness measurements using white-light interferometry indicate fuel thicknesses on the periphery on the order of 100 μm. The hot spot ($a = 5$ μm) fit regime was not affected by the changes in fuel mass due to the short thermal penetration depths associated with this regime.

5. *Substrate material.* The substrate material played a key role in determining the ratio of heat dissipated by the fuel and substrate, respectively. The analytical models also provided estimates on this input power ratio. For the borosilicate glass substrates, the amount of power dissipated by the fuel—i.e., the useful power—was just over 20 % for the meander layout and less than 15 % for the hot spot layout. These devices are terribly inefficient and one of the main reasons that the power levels reported in this thesis were many times higher than those reported in the literature—notwithstanding differences in fuels used. The amount of heat lost to the substrate can be mitigated several ways:

    - Typically—in the field of microfabricated hotplates [55]—the heaters are sus-

pended on thin membranes to reduce power consumption. The group at CNRS-LAAS obtained successful fuel ignition with input power levels down to 80 mW—using ZPP fuel [15]. However, this solution is not ideal due to the debris caused by the bursting membranes.

- Another method of reducing the thermal losses to the substrate is to fabricate suspended igniters above a bulk substrate using a sacrificial material. The small air gap separating the igniter from the substrate acts like a thermal resistance. This method was successfully demonstrated by the group at SAMLAB [11, 19] and achieved input power levels down to 350 mW using K-DNBF fuel.
- In this work, the thermal losses were mitigated by making use of lower thermal conductivity substrate materials. Using polyimide, a heat resistant polymer foil k_{pi} = 0.29 W/(m·K), rather than borosilicate glass k_{glass} = 1.2 W/(m·K), the input power needed for ignition was reduced by a factor of 3.8 for the meander igniter, achieving fuel combustion for input powers as low as 240 mW.

6. *Closed chambers.* Adding the silicon combustion chambers to the igniters did not affect the ignition delay times; however, the small silicon chambers increased the thermal losses in the fuel, increasing the minimum input power levels required for ignition from ~ 850 mW to ~ 1300 mW. Others have noted that using bulk silicon combustion chambers in compact arrays of pyroMEMS thrusters leads to thermal cross-talk between the neighboring devices and sympathetic combustion that can spread through the entire array [5]. These thermal losses can be mitigated by adding insulating grooves [5] or making use of a lower thermal conductivity material, such as glass [15, 17] or a polymer material (as in chapter 6).

4.7.2 Combustion

Firstly, the fuel combustion was found to propagate via subsonic deflagration, rather than super-sonic detonation—as is commonly observed macro-scale fuel grains. This is attributed to the larger thermal losses at smaller scales. The burning rate increased with decreasing input power, due to the increased pre-heating of the fuel mass prior to the onset of combustion; however, below a certain level of input power, deflagration did not occur only smoldering. This threshold level was found to depend on the thermal losses to the environment—e.g., the substrate chamber materials. Furthermore, if the fuel drop was too thin, the deflagration was found to quench. As such, a minimum fuel mass and input power must be attained in order to ensure complete fuel combustion in pyroMEMS devices.

Second, stable sustained combustion was achieved using bottom-side Joule-effect pyroMEMS igniters. We investigated the effect of igniter layout, binder content and input power on the combustion behavior and found that both increasing binder content and power delayed the onset of fuel peeling and ejection—binder content being the more important factor. Both the meander and annular igniters suffered from fuel peeling; however, adding the hot spots nearly

completely eliminated the onset of peeling for all amounts of binder and input power.

The onset of fuel peeling occurs when the pressure generated by the expanding combustion front overcomes the adhesion of the fuel to the substrate. We investigated three methods to counteract this action:

1. *Binder content.* Increasing the binder content reduced fuel peeling by:
    - increasing the adhesion of the fuel to the substrate (adhesin® is an adhesive);
    - reducing the energy content of the fuel mixture, as confirmed by chemical kinetics simulations (adhesin® is inert);
    - slowing the chemical kinetics of the mixture, as demonstrated by the reduced the burning rates.
2. *Input power.* Increasing the input power lead to larger thermal gradients within the fuel drop and smaller thermal penetration depths before ignition. This localized the fuel heating to a smaller area. When this initial volume ignited, it released a small amount of energy that heated the surrounding fuel, which ignited in turn. This caused a steady combustion wave to propagate. If the initial heated zone is too large, the large energy release will cause the drop to be ejected from the surface. Of course, if the fuel drop is much thicker than this initial ignited volume, localized fuel ejection will occur.
3. *Hot spots.* Hot spots acted in the same way as input power, in that they increased the localized heat flux. However, uncertainty in the fuel/igniter alignment lead to increased ignition delay time variance. A compromise is therefore needed between ignition variance and fuel peeling.

4.7.3 Fuel/Igniter Alignment

To summarize, one of the main sources of variability in for ignition and combustion results using the drop-coated, bottom-side igniters was the fuel/igniter alignment. There are many ways to improve or mitigate problems caused by small fuel drop misalignments: in this work this was done by using igniters with multiple annular rings to ensure the heater covers the edge of the drop. However, increasing the heated area lead to peeling and fuel ejection—as demonstrated by the annular igniters above. Ideally, we want a highly localized heat flux—using hot spots—exactly on the edge of the fuel drop. Future work will investigate ways to control the area of the fuel drop on the substrate, such as:

- optimizing the fuel deposition parameters;
- patterning hydrophilic/hydrophobic materials on the substrate to “pin” the water-soluble fuel mixture to a specific area on the substrate;

- etching a shallow (~ 10 μm) indentation in the substrate—via buffered hydrofluoric acid etching of glass, for example—to create a small side-wall, which will limit the extent of the fuel drop on the surface.

4.7.4 Summary

Presented in table 4.13 is a broad summary of the results, along with published results found in the literature. The bottom-side, hot spot igniters performed well: they successfully prevented fuel peeling by igniting the drops along their periphery. Fuel peeling was avoided by localizing the fuel heating to small areas near the periphery of the fuel drops—using the hot spot layout—and by increasing the binder content. The minimum ignition power levels on borosilicate glass were relatively high compared with existing results—particularly those fabricated on suspended membranes—however they were substantially lowered by fabricating the devices on polyimide foil. The ignition delay times achieved with the bottom-side igniters were up to 2 orders of magnitude shorter than the fastest times in the published in the literature, whereby substantially lowering the overall energy needed for ignition. Lastly, in terms of standard error, the results obtained using the bottom-side igniters were better than those in the published literature—notwithstanding the results obtained using the hot spot igniter in the $a = 5$ μm fit region. This is because the bottom-side igniters ensure intimate thermal contact between the fuel and the igniter. The optimum configuration was found to be the hot spot igniters with relatively low input powers—0.8 to 1.25 W—such that it is operating in the $a = 90$ μm regime.

Table 4.13: Comparison of bottom-side ignition behavior with literature.

		Q_{total} (W)		Δt_I (ms)			
Substrate	Layout	min	max	min	max	error	Reference
Borosilicate Glass	Meander	1.39	12.58	17	970	10 %	This work
	Annular	0.78	18.00	1	18000	10 – 25 %	
	Hot Spot	0.85	2.67	0.1	9500	25 –100 %	
Polyimide Foil	Meander	0.24	4.08	38	850	10 %	This work
	Hot Spot	0.28	0.58	0.3	2300	~100 %	
SiO_2/SiN_x Mem.	Meander	0.08	0.15	20	750	~100 %	[15]
Ceramic (LTCC)	Line	1.3		600	2000	~ 54 %	[28]
Borosilicate Glass	Meander	0.16		12940		N/A	[29]

4.8 Conclusion

In this chapter, we carried out an in-depth study of the ignition and combustion behavior of a novel bottom-side igniter concept with fuel droplets. This represents the first in-depth study of pyroMEMS ignition—varying multiple parameters and testing hundreds of devices—ever carried out. This was made possible due to the igniter's highly simplified and robust

fabrication process. Furthermore, their ignition and combustion behavior was more reliable than the current state-of-the-art. The bottom-side igniters are ideally suited for pyroMEMS applications in which reliability and cost are key concerns, such as automated fluid actuators for drug injection or safe, arm and fire devices for military ordinance.

5 Top-side Igniters

5.1 Introduction

In this chapter, we will investigate and characterize a simple method of fabricating top-side pyroMEMS igniters in direct contact with the fuel to ensure good thermal contact between the two. Although the bottom-side architecture and devices presented in chapter 4 have advantages in terms of simple fabrication and reliable performance, they only work for fuel drops on the order of a few hundred micrograms. In many applications—such as thrusters for small satellites—very high loading densities are required in order to achieve reasonable performance levels. In such cases, fully-filled fuel chambers—and therefore top-side igniters—are required.

From the beginning, we wanted to develop an alternative to the membrane-suspended igniters for 3 reasons:

1. The ruptured membranes generate debris that is highly undesirable in space environments and can clog the nozzle leading to catastrophic failure of the thruster;
2. Membrane delamination and premature rupture are leading causes of ignition failure [15];
3. Micrometer-thick dielectric membranes are extremely fragile, making fuel filling more difficult. Although thicker membranes—such as the ones used by [17]—are more sturdy, they exacerbate the debris problem.

PyroMEMS architectures have been limited by the fact that solid propellants are generally forbidden in cleanroom environments: designers were limited to adding the fuel during the back-end processing. In a sense, the membrane-suspended igniters act as a sacrificial platform on which the igniter and the fuel can be brought into contact. Our aim is to do away with the membrane—and all it's associated problems—and directly deposit the igniter onto the fuel surface by offset shadow mask metal evaporation. Integrating the solid propellant

fuel into the process flow—as opposed to adding it during back-end processing—is part of a continuing trend in MEMS development of integrating an increasing number of unconventional functional materials into microsystems. The primary goal of these experiments was to demonstrate that exotic materials—such as solid propellants—can be successfully integrated into the pyroMEMS device fabrication.

In this chapter, we will present two generations of shadow mask igniters: the first fabricated over top the fuel drops used in chapter 4 (see figure 5.1a) and the second deposited onto full fuel-filled chambers (see figure 5.1b).

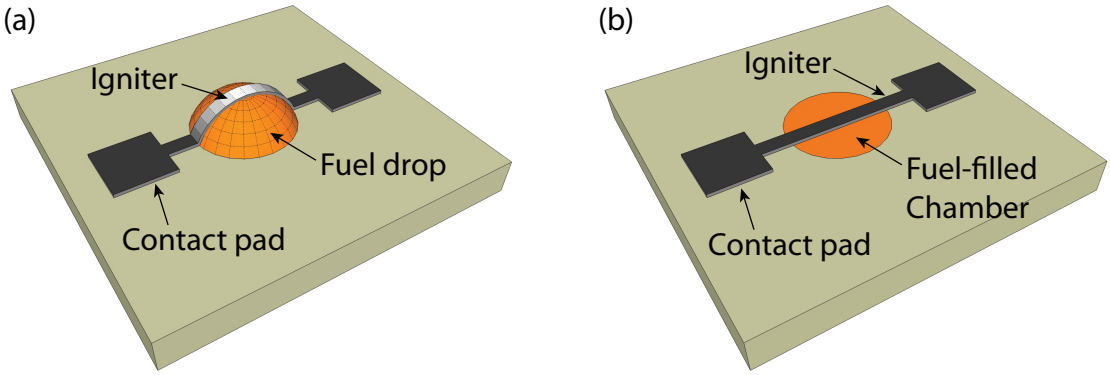

Figure 5.1: Sketch of a shadow-mask evaporated top-side igniter over (a) a fuel drop and (b) a fuel-filled chamber.

5.2 Concept and Fabrication

Offset shadow mask evaporation allows patterning of metal onto a surface in a non-contact, dry manner—which is highly desirable when the surface is highly unorthodox, like a solid propellant fuel mixture (figure 5.2). It reduces the risk of damage to the surface as well as cross-contamination, although at the price of reduced deposition resolution.

5.2.1 Shadow Mask Layout

The shadow mask consisted of a 100 μm thick stainless steel sheet patterned via laser micromachining. A 1 mm stainless steel spacer was used to prevent the shadow mask from touching the fuel drop (figure 5.3), resulting in a 500 μm clearance between the 500 μm-thick glass surface and the shadow mask. The layout used for the shadow mask igniters was a simple dog-bone shape, consisting of a straight line with square contact pads at either end. For the first generation of shadow mask igniters, the line measured 200 μm wide and 3 mm long, and the square contact pads were 1 mm × 1 mm. Twenty igniters were processed at a time in parallel, although nothing in principle prevents wafer-scale processing from being carried out. For the second generation of shadow mask igniters, the overall dimensions were increased to facilitate the manual alignment of the mask overtop the chips. The contact pads measured

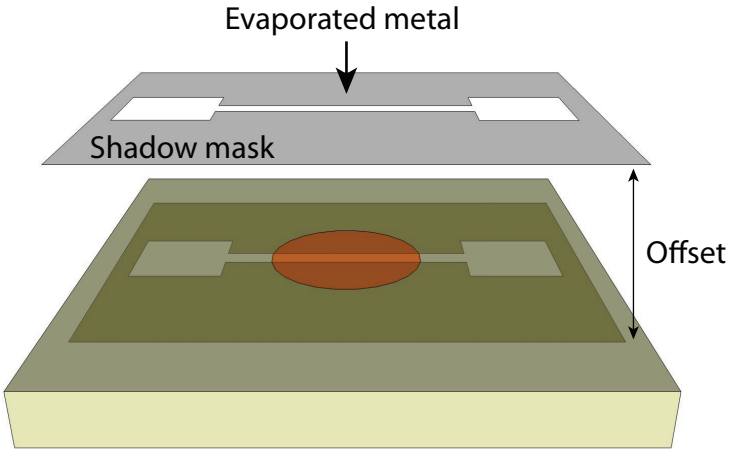

Figure 5.2: Sketch of offset shadow mask evaporation.

1.5 mm × 1.5 mm, while the lines measured 500 μm wide by 9 mm long. 14 devices were patterned at a time.

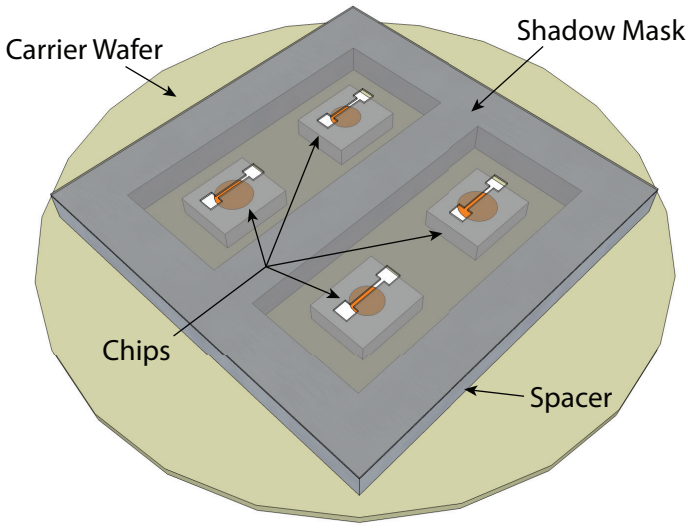

Figure 5.3: Sketch of the shadow mask evaporation jig.

5.2.2 Fuel

For the first generation device, we recycled bottom-side igniter chips in order to test the compatibility of metal evaporation onto the solid propellant fuel mixture. For all of the shadow mask igniters presented in this chapter, the binder mass fraction of the fuel mixture was fixed at 10 %. An added challenge in depositing conductive metal igniters onto the fuel was the high surface roughness of the fuel mixture, on the order of 2.5 μm (figure 5.4). This required relatively large metal thicknesses in order to obtain tightly-controlled igniter resistance values.

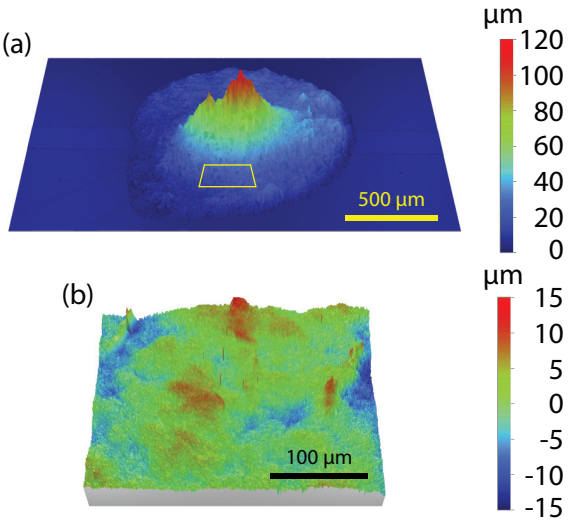

Figure 5.4: (a) White-light interferogram of a fuel drop with a line-of-sight igniter and (b) a close-up of the propellant surface roughness.

5.2.3 Choice of Metal

A major concern with this fabrication method was whether the fuel would survive the atomic bombardment during physical vapor deposition without igniting. For this reason evaporation was preferred over sputtering, because the atoms are generally less energetic. Furthermore, the kinetic energy of the impinging atoms scales with the heat of vaporization, therefore metals with lower values were preferred for the shadow mask igniters. An additional requirement was adequate surface adhesion of the metal. From the list of available target materials at the EPFL CMI cleanroom facility (table 5.1), aluminum was chosen and deposited by electron-beam evaporation.

Table 5.1: List of available e-beam evaporation targets.

Material	Heat of vaporization (KJ/mol)
Aluminum	294.0
Copper	300.4
Chromium	339.5
Cobalt	377.0
Nickel	377.5
Titanium	425.0

5.3 1^{st} Generation: Igniters on Fuel Drops

5.3.1 Deposition Parameters

The deposition thickness and substrate stage were varied in order to optimize the igniter's performance (see table 5.2). 20 igniters were fabricated at a time and a total of 80 igniters were produced.

Table 5.2: Shadow mask igniter evaporation parameters (1^{st} gen.).

#	# devices	Thickness (nm)	Substrate Holder
1	40	800	Rotary-Planetary
2	20	1500	Rotary-Planetary
3	20	800	Fixed

The baseline case (trial 1) consisted of an 800 nm (nominal) aluminum film deposited via electron-beam evaporation on a rotary–planetary stage. The rotary–planetary stage was used to obtain conformal coverage of the rough fuel surface to achieve a continuous metal line. The disadvantage of the rotary–planetary stage was poorer feature definition (i.e. 'under-evaporation') and thinner metal lines—due to the 500 μm offset between the shadow mask and the substrate (figure 5.5).

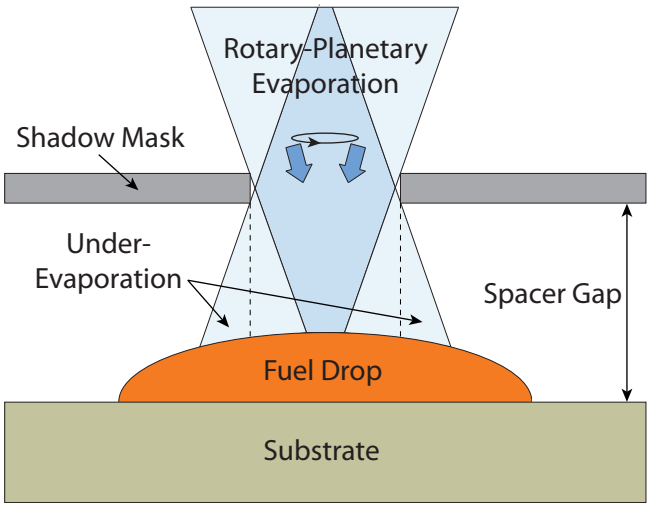

Figure 5.5: Sketch of offset shadow-mask evaporation using a rotary-planetary substrate holder showing under-evaporation.

In order to counter the thinning effect of the under-evaporation, the metal thickness was increased to 1500 nm for trial #2. Alternatively, a fixed substrate holder was used to perform a line-of-sight evaporation for the last trial.

5.3.2 Igniter Characterization

All three evaporation trials were successfully carried out without any fuel ignition or any other visible degradation of the propellant (e.g., figure 5.6). The rotary–planetary igniters exhibited under-evaporation and decreased line thicknesses due to the relatively large spacer gap (figure 5.7). A deposition thickness of 800 nm—on the quartz microbalance—resulted in line thicknesses on the order of 100 nm, whereas 1500 nm-thick depostion (nominal) resulted in a ~ 500 nm line thickness. The line-of-sight evaporation, on the other hand, yielded the expected thickness of 800 nm. Unfortunately, the line-of-sight trial yielded igniters with poor substrate adhesion and could not be wire-bonded for combustion testing.

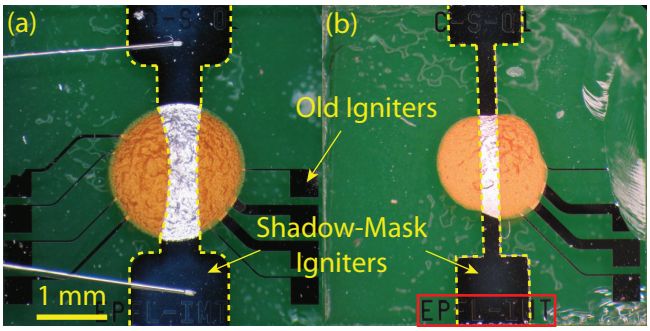

Figure 5.6: Dark field photographs of the shadow mask igniters (1^{st} gen.) fabricated using (a) a rotary–planetary substrate holder (1500 nm) and (b) line-of-sight evaporation (800 nm). The contact pads lining the sides of the chips and interconnects leading underneath the fuel drops are the bottom-side igniters from chapter 4 and are unrelated to this study (indicated as 'old igniters').

The repeatability of the fabrication technique was characterized by measuring the dispersion in the igniter resistances. The resistance values were found to follow log-normal distributions (see figure 5.8). The reason for this is that the electrical resistance R of a metallic line element of length l and cross-sectional area A is given by

$$R = \rho \frac{l}{A} \tag{5.1}$$

where ρ is electrical resistivity of the line. Assuming that the individual line dimensions follow normal distributions, the line resistance—obtained from the multiplication and division of normally distributed data—will therefore obey a log-normal distribution. Intuitively, this follows since electrical resistance has, by definition, a lower bound—zero ohms—but has no upper bound; therefore, distributions with relatively small means and large variances will inevitably be positively skewed. For distributions with variance much smaller than their means, log-normal distributions approach normal distributions—as was the case for trial #2.

The mean and modal resistance values and standard deviations of the igniters are given in

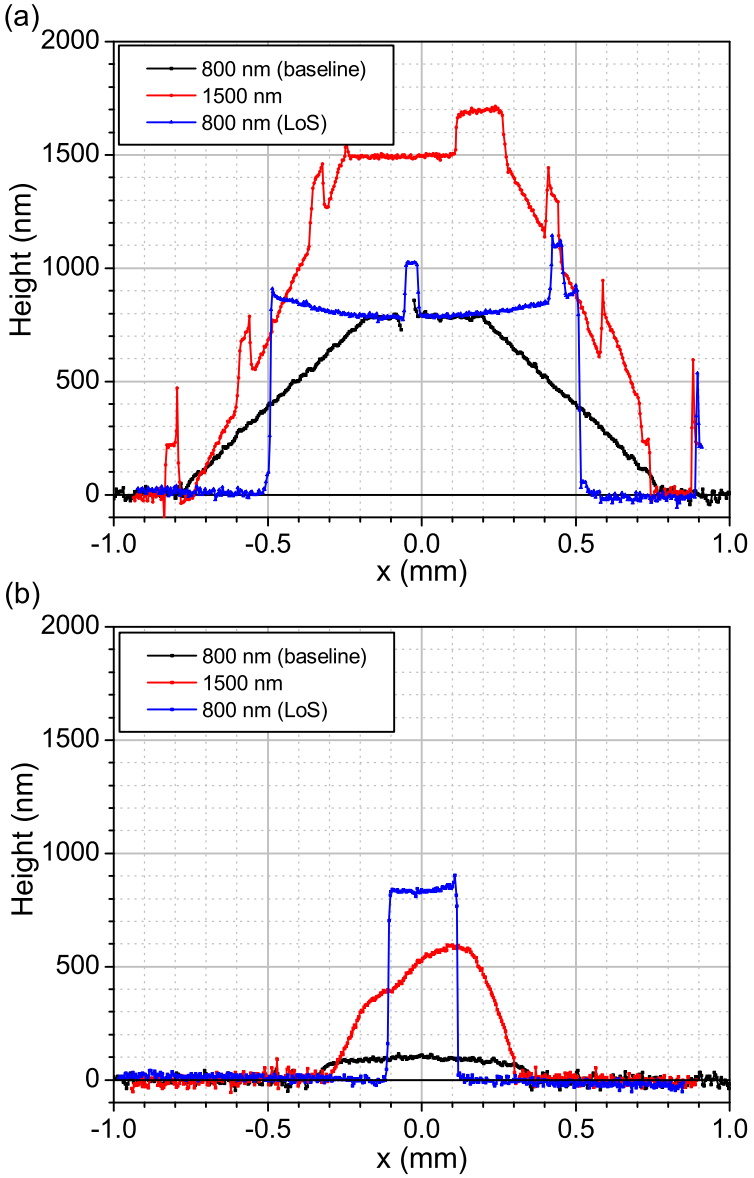

Figure 5.7: 2D profiles of the (a) contact pads and (b) igniter lines obtained via white-light interferometry. The ~ 200 nm high bumps on the pad profiles were due to word 'EPFL-IMT' patterned alongside the old igniters (i.e., see red box at the bottom of figure 5.6b).

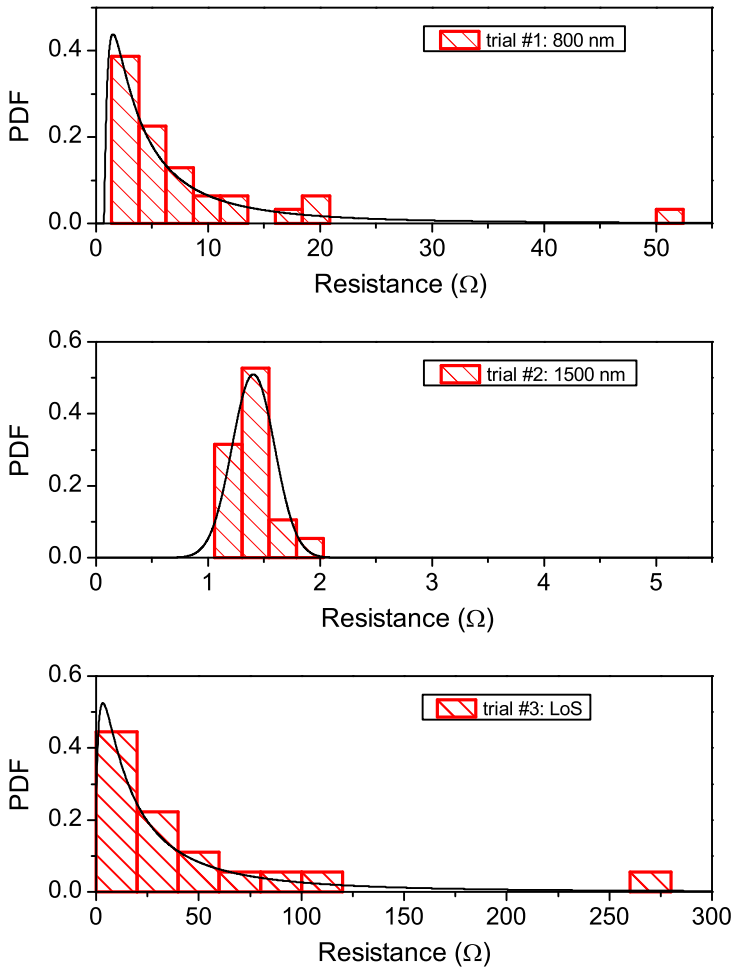

Figure 5.8: Igniter resistance histograms for the 1^{st} gen. shadow mask igniter resistances (red columns) with their best fit log-normal probability density functions (black line).

table 5.3. The trial identifiers refer to the parameter which was varied during that trial.

Table 5.3: Shadow mask igniter resistance values (1^{st} gen.).

#	Trial ID	Mode (Ω)	Std. dev. (Ω)	Relative st. dev. %
1	Baseline	1.92	4.82	251
2	1500 nm	1.37	1.40	102
3	LoS	3.55	20.9	589

The thin igniters—trials 1 and 3—exhibited large variance and positive skew, while the 1500 nm thick igniter histogram was relatively sharp and nearly Gaussian. We postulate that the thin igniters were composed of a network of interconnected metallic islands caused by the large roughness of the propellant surface ($R_a \sim 2.5\ \mu$m). Similar behavior has been observed in conductive granular materials [56]. Compared to the baseline trial—using the rotary-planetary substrate holder—the igniters fabricated with line-of-sight evaporation (trial 3) yielded a substantially higher standard deviation (20.9 versus 4.82) and modal resistances (3.55 versus 1.92) even though they yielded improved feature definition and thicker lines. This is because igniters fabricated by line-of-sight evaporation were more susceptible to defects due to the non-conformal coating of the rough propellant surface. Compared to the bottom-side igniters patterned by photolithography—hard contact mode—the offset shadow mask igniters yielded much larger relative errors (> 100 % vs. ~ 2 %). This was due to the large offset distance and the large roughness of the propellant surface. In summary, we expect the best ignition behavior from the 1500 nm aluminum igniters (trial #2) based on their sharp resistance distribution.

5.3.3 Experimental Methodology

The same experimental set up as in chapter 4 was used. A 1 s, square voltage pulse was applied to the igniters . The voltage pulse magnitude was varied from 2 to 100 V. Experiments were performed in air.

5.3.4 Results

Two different ignition regimes, Joule heating and spark-induced ignition, were observed depending on the thickness of the igniter and the input power level. This section is divided into two parts: first the two different ignition regimes will be presented, followed by a summary of the results for the two different igniters—the 800 nm-thick and the 1500 nm-thick igniters. A summary of the ignition and combustion results is given in table 5.4.

Joule Heating Ignition Regime

The Joule heating ignition regime was characterized by a well-defined ignition delay time Δt_I which decreased with increasing input power Q_{total}. Combustion began with the formation of

Table 5.4: Summary of the shadow mask ignition and combustion results (1^{st} gen.).

		Success Rate (%)	
Substrate Holder	Igniter Thickness (nm)	Ignition	Combustion
Rotary-Planetary	800	12/40 (30 %)	12/12 (100 %)
	1500	20/20 (100 %)	12/20 (60 %)
Fixed	800	Not Tested	

one or more flame kernels near the center of the drop—which ruptured the igniter—and steady flame spreading until the fuel drop was completely consumed (see figure 5.9). The flame spread faster over the igniter than across the virgin propellant due to localized pre-heating of the fuel by the igniter.

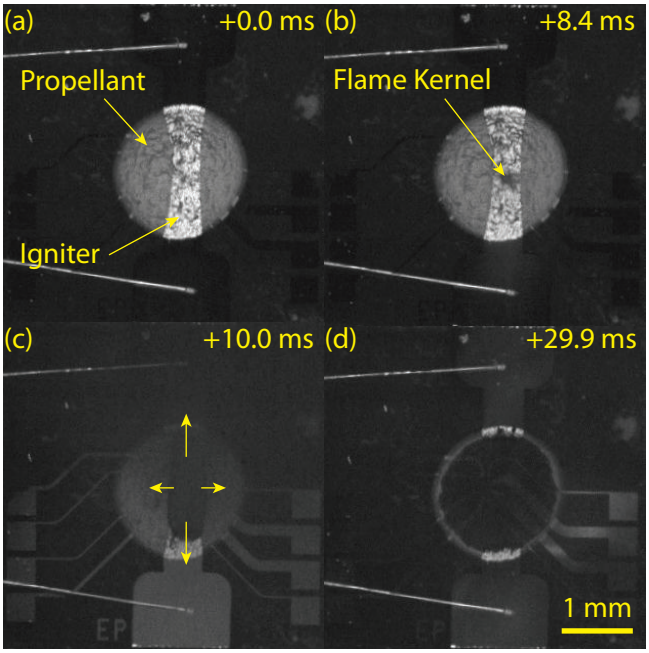

Figure 5.9: High-speed video frames showing Joule heating ignition and combustion (1500 nm thick igniter (1^{st} gen.), Q_{total} = 1.7 W): (a) before ignition, (b) appearance of flame kernel in the center of the drop, (c) smooth combustion, and (d) post combustion. Time stamp is given relative to the start of the voltage pulse.

Spark-Induced Ignition Regime

So-called spark-induced ignition was said to occurred at high input voltages, which caused the igniter to fail, release sparks and ignite the fuel. The sparks always occurred within one high-speed video frame (i.e. less than 100 μs) of the initiation of the voltage pulse (see figure 5.10). They tended to appear in the troughs (darkened zones) of the igniter surface—i.e.where breaks and shadowing defects were likely to occur.

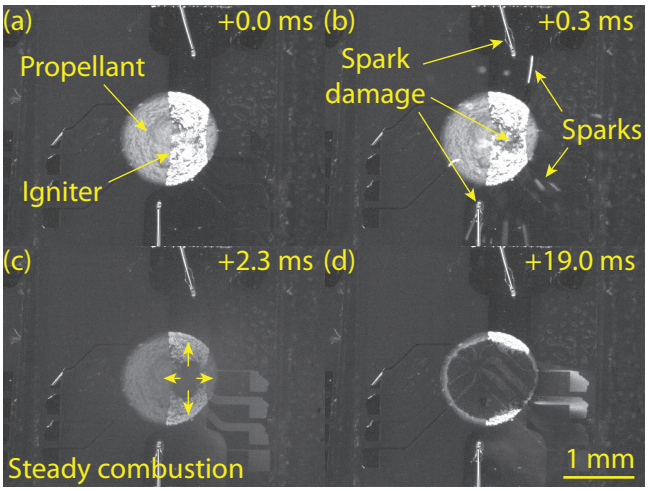

Figure 5.10: High-speed video frames showing spark-induced ignition and combustion (800 nm-thick igniter (1^{st} gen.), Q_{total} = 12.5 W): (a) before ignition, (b) 2 frames after sparking, (c) smooth combustion and (d) post combustion. Time stamp is given relative to the start of the voltage pulse.

1500 nm Igniter Results

For the 1500 nm-thick igniters, all 20 igniters were successfully ignited, although only 12 maintained self-sustained combustion waves—failing shortly after the igniter was severed (e.g., see figure 5.13d). Typical voltage and current traces are given in figure 5.11, showing a smooth decrease in current due to the increase in temperature—and resistance—prior to ignition. When the fuel ignited, the current dropped to zero as the igniter ruptured. In this way, the igniters automatically minimized the input energy needed to achieve ignition for a given input power level. The Joule heating ignition regime was observed at moderate input powers between 1.7 W and 11.3 W (see figure 5.12). At lower input powers (0.87 W and below), no combustion occurred for voltage pulses up to 2.5 s—i.e. two orders of magnitude longer than the longest ignition delay times reported in figure 5.12. For higher powers (~ 30 W), spark-induced ignition was observed.

The mean ignition delay times decreased with increasing input power. The devices that maintained self-sustained combustion waves ignited faster than those that quenched. Combustion quenching was due to the smaller thickness of the drops—as found in chapter 4. The thinner drops were cooled by the glass substrate, which behaved as a heat sink. This cooling effect caused the combustion front to fail, whereas complete combustion was observed for the thicker drops (figures 5.13a,b vs. figures 5.13c,d).

800 nm-thick Igniter Results

Ignition with the 800 nm-thick shadow mask igniters failed to ignite with voltages in line with Joule heating ignition, requiring instead voltages which were orders of magnitude larger (75

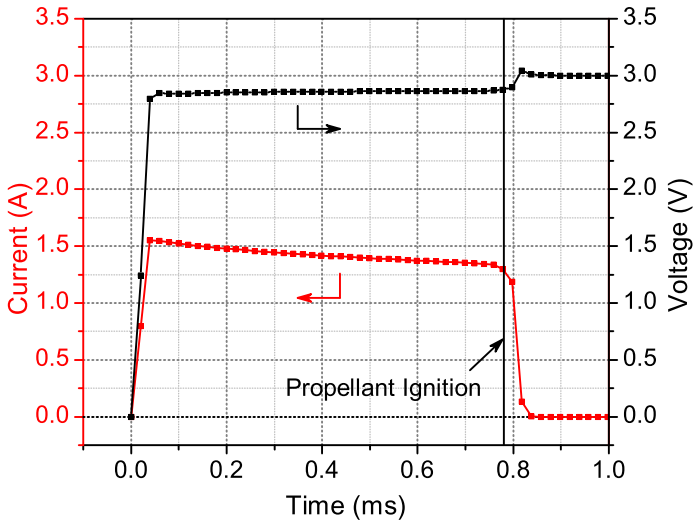

Figure 5.11: Representative current and voltage traces for a 1500 nm-thick shadow mask igniter (1^{st} gen., Q_{total} = 4.1 W).

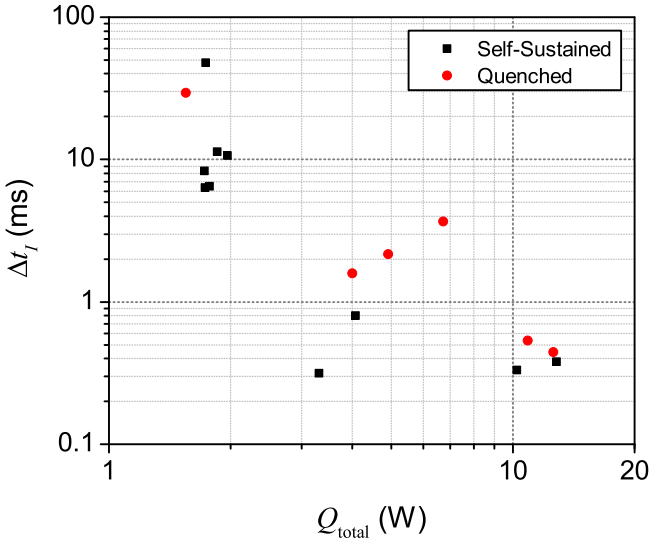

Figure 5.12: Ignition delay time versus input power for the top-side shadow mask igniters (1500 nm thick, 1^{st} gen., Joule ignition regime). Devices underwent both self-sustained (black) and quenched combustion (red).

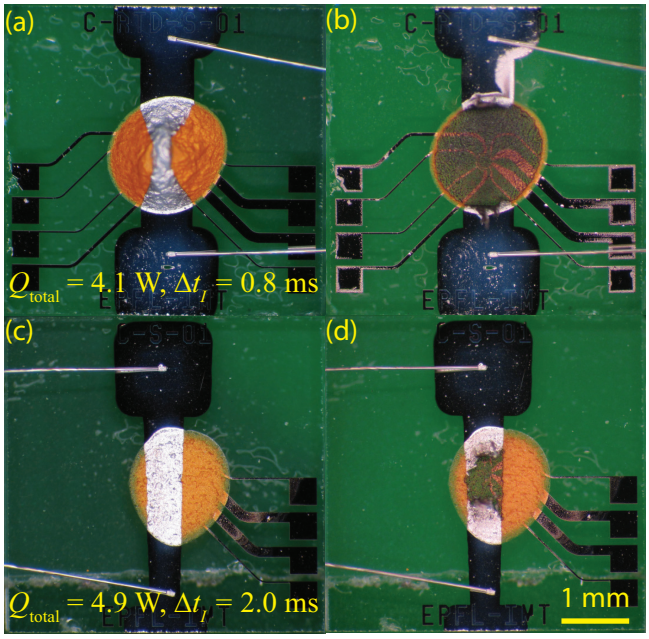

Figure 5.13: Effect of drop thickness on ignition and combustion behavior. (a) Thick drops (400 ± 20 μm) achieved (b) complete combustion, while (c) thinner drops (100 ± 75 μm) (d) failed to sustain the flame front.

and 100 V were tested). Ignition depended on sparking across random defects in the metal lines, which cannot be reliably controlled. If the input voltage was too low, the igniter sparked and was damaged—open circuited (figure 5.14)—but did not ignite the fuel (13 out of 40 tested igniters), and if it was too high, the device would be completely destroyed (15/40), i.e. evaporation of the igniter metal and bondwires (figure 5.15). The remaining 12 thin igniters successfully ignited the fuel (as in figure 5.10). Successful combustion occurred for the largest igniter resistances, while those that were destroyed had the lowest resistances (figure 5.16).

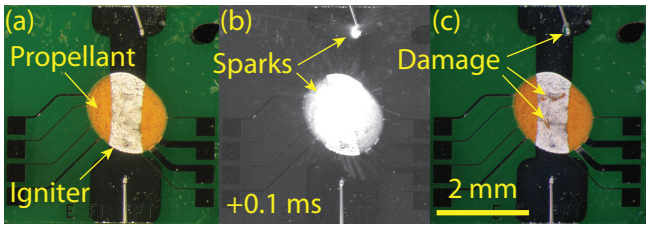

Figure 5.14: A 800 nm thick shadow mask igniter that failed to ignite due to spark-induced igniter damage: (a) before, (b) 0.1 ms after ignition and (c) after voltage pulse.

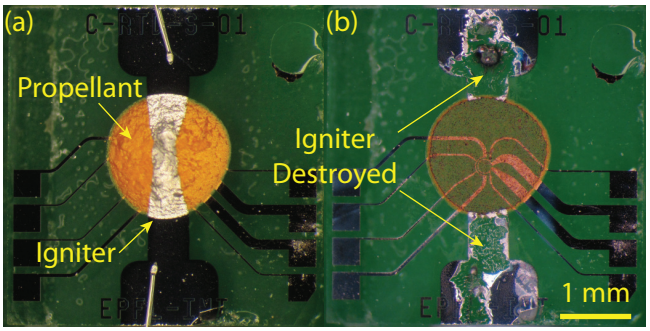

Figure 5.15: (a) Before and (b) after photographs of a 800 nm-thick shadow mask igniter that was destroyed by an excessively large voltage pulse.

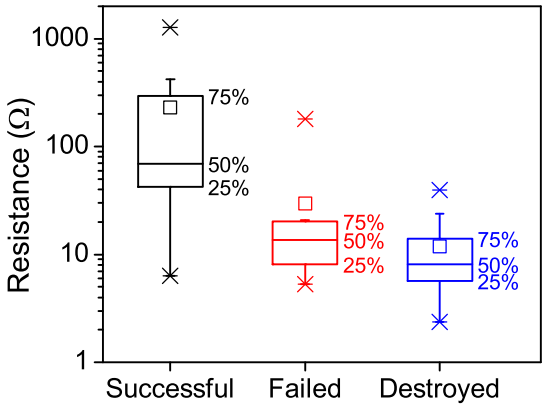

Figure 5.16: Box plot showing the igniter resistance distributions vs. combustion outcome—successful ignition, failed ignition or igniter destruction. The labels represent the percentiles of the boxes.

5.4 2^{nd} Generation: Igniters on Full Chambers

5.4.1 Igniter Design

The main difficulty in fabricating reliable shadow mask igniters on top of fuel-filled chambers is how to deal with the sharp edge of the chamber. We chose to deal with this by over filling the fuel chamber so that the fuel covered the sharp corner (figure 5.17). Furthermore, based on the results from the 1^{st} generation, many changes to the igniter design were made for the second generation shadow mask igniters in order to improve device performance:

1. The evaporated metal thickness was further increased to 2000 nm;
2. The fuel chamber diameter was increased to 4 mm—compared with the fuel drop diameter of ~ 1.6 mm—in order to facilitate the alignment of the shadow mask on top of the chips;
3. The line width was increased to 500 μm to reduce the effect of shadowing by the offset shadow mask. This effect severely diminished the resultant thickness of the igniter lines as shown in figure 5.7.

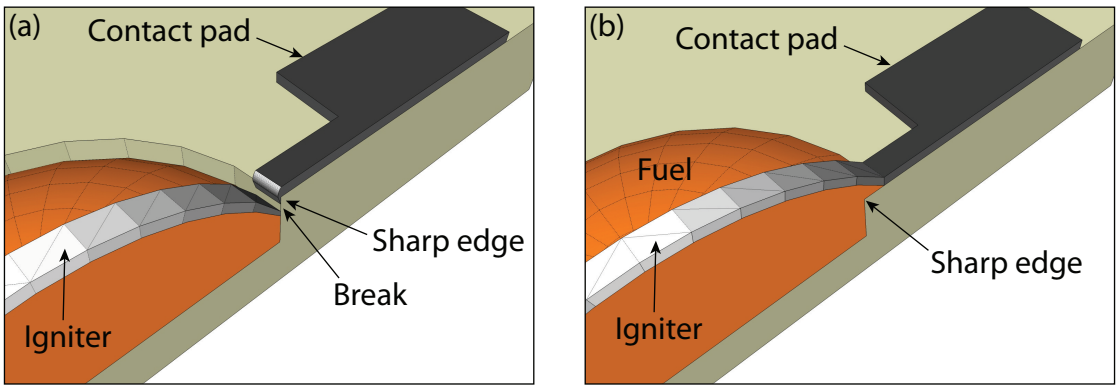

Figure 5.17: Sketches showing (a) the igniter discontinuity caused by the sharp edge of the fuel chamber and (b) the proposed solution by overfilling the fuel chamber.

The final 2^{nd} generation dimensions consisted of:

- Chip: 15 mm × 6 mm;
- Contact pads: 1.5 mm × 1.5 mm;
- Line width: 500 μm;
- Line length: 9 mm

A single evaporation trial (2000 nm, Al, rotary-planetary substrate holder) was performed yielding for a total of 14 full chamber shadow mask igniters.

5.4.2 Igniter Characterization

Figure 5.18a shows a full chamber device after shadow mask evaporation. Typical 2D profiles are shown in figure 5.18b. Although the strategy of overfilling the fuel chambers to cover the chamber's sharp edge was successful, it was not reliable. The main difficulty lay with the propellant deposition method: after the fuel was deposited and placed in the oven to evaporate the water, the fuel shrunk by half it's initial volume. As such, many of the overfilled chambers shrunk away from the chamber edge causing breaks in the igniter, or very thin lines which would break upon application of moderate voltages. A total of 5 out of the 14 devices yielded resistances in the range of a few ohms (figure 5.19), while the others were open circuited.

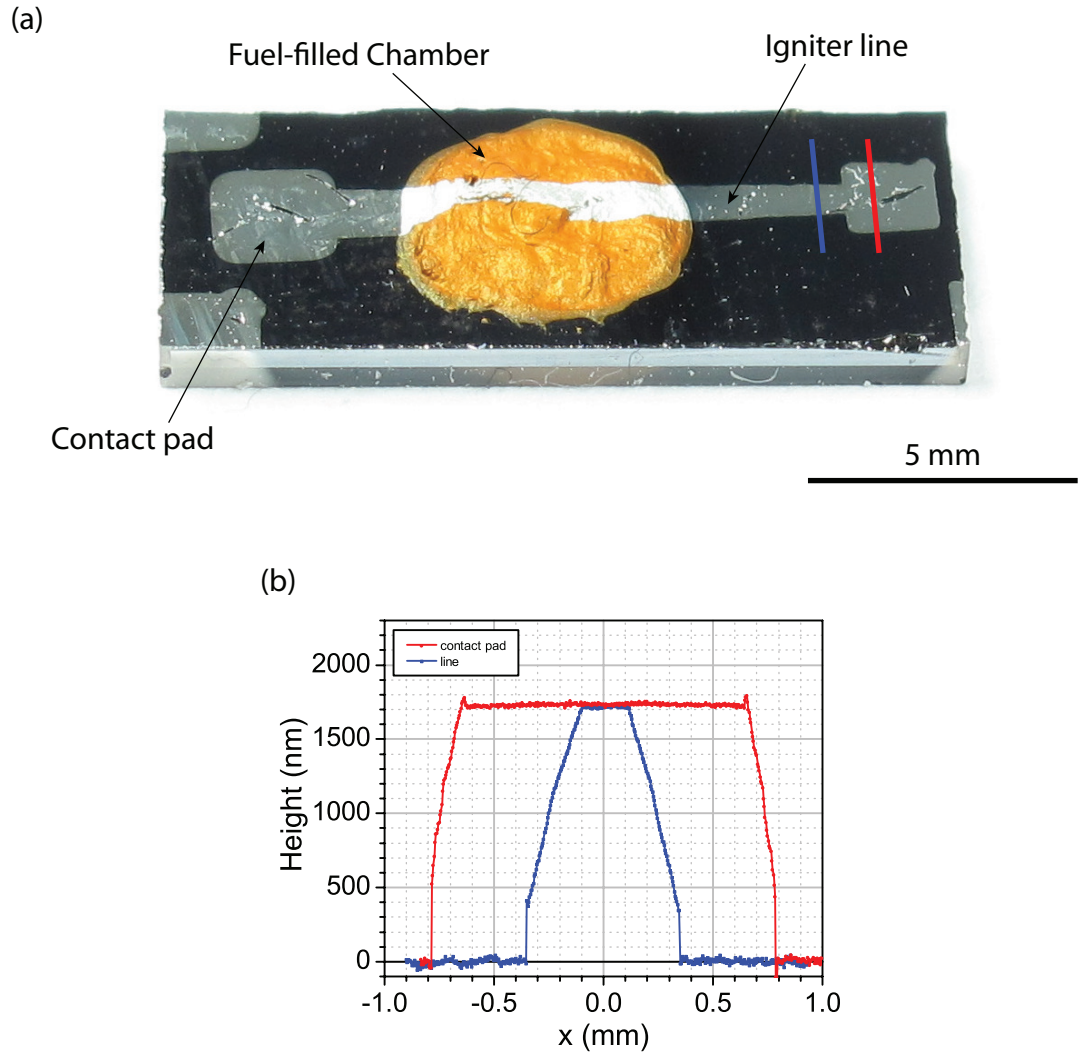

Figure 5.18: (a) Picture of a top-side igniter over a fuel-filled chamber. (b) 2D profiles of the contact pad and igniter line measured by white-light interferometry.

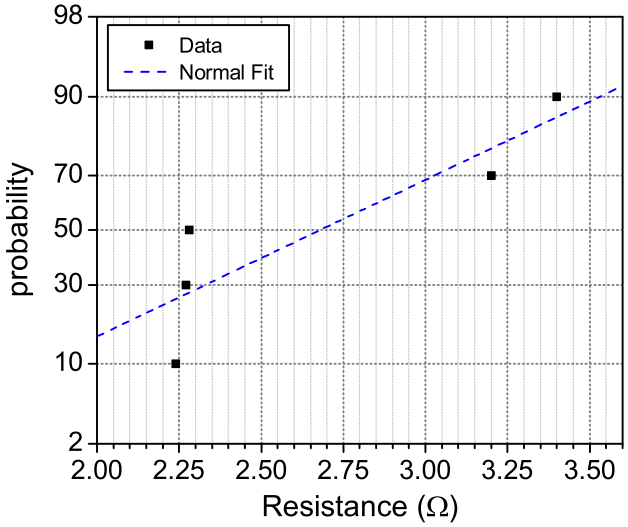

Figure 5.19: Shadow mask igniter resistance probability plot.

5.4.3 Results

Successful combustion of the fuel charge was achieved for the 5 igniters with low resistances (35.7 % success rate). A range of input voltages were tested: four of the devices ignited by Joule heating near the center of the fuel charge and another ignited by spark-induced ignition—due to the excessive input voltage used. All successful tests resulted in fully self-sustained combustion waves (see figure 5.20).

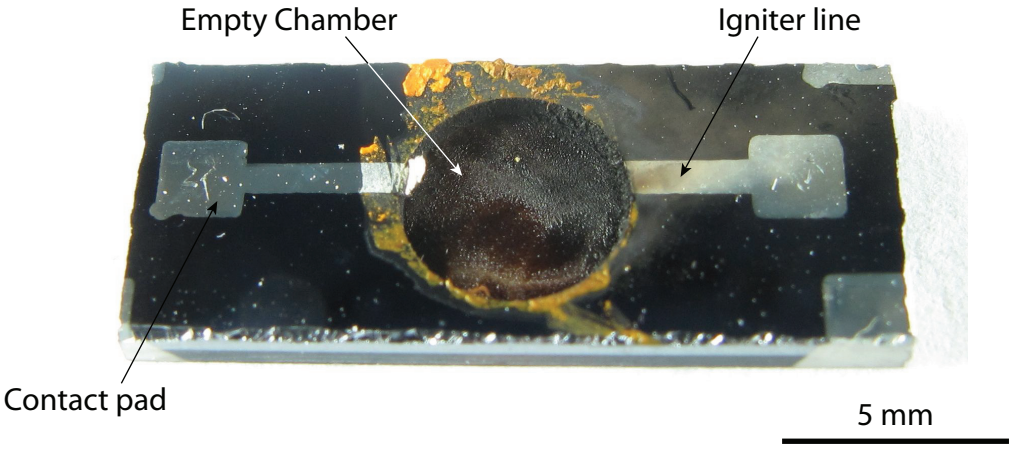

Figure 5.20: Picture of a top-side igniter after complete fuel combustion.

Failure of the shadow mask igniters was attributed to poor step coverage at the edge of the chamber due to shrinkage of the fuel away from the chamber walls (see figure 5.21). One can clearly see (inside the yellow circle) in figure 5.21a the small bridge—bright spot—spanning

chamber edge step—dark line—which was subsequently destroyed by the application of the ignition signal in figure 5.21b and c.

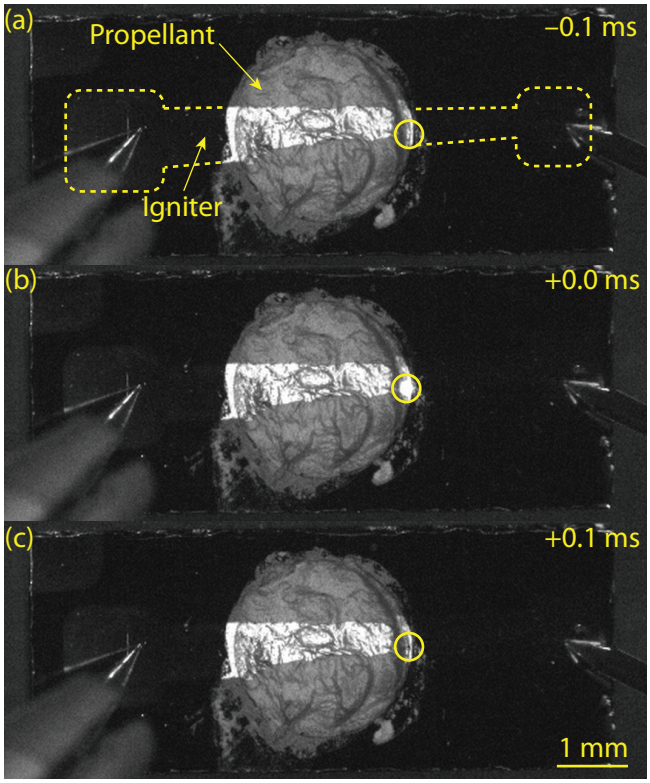

Figure 5.21: A 2^{nd} gen. top-side igniter that failed to ignite due to poor chamber edge step coverage: (a) before, (b) at ignition and (c) 0.1 ms after ignition.

Ignition delay time versus total input power is shown in figure 5.22. The ignition delay times for the full chamber devices were an order of magnitude longer than for the igniters over fuel drops. This was due to the larger igniter line width—a wider line must dissipate more heat over a larger area in order to obtain the same temperature rise.

5.5 Discussion

In this work, we successfully demonstrated—for the first time—that metal igniters can be directly evaporated onto the solid propellant fuel surface without igniting or damaging the fuel. Self-sustained combustion was achieved in both fuel drops and full fuel chambers. As with the membrane-suspended igniters, the shadow mask igniters were ruptured during fuel ignition—which automatically minimized the energy consumed by the igniter. We faced two main challenges in fabricating functional top-side igniters by offset shadow-mask evaporation:

1. *Fuel surface roughness.* The large surface roughness of the dried fuel mixture ($R_a \sim 2.5$ μm) needed to be conformally-coated by the igniter. This required a large amount of

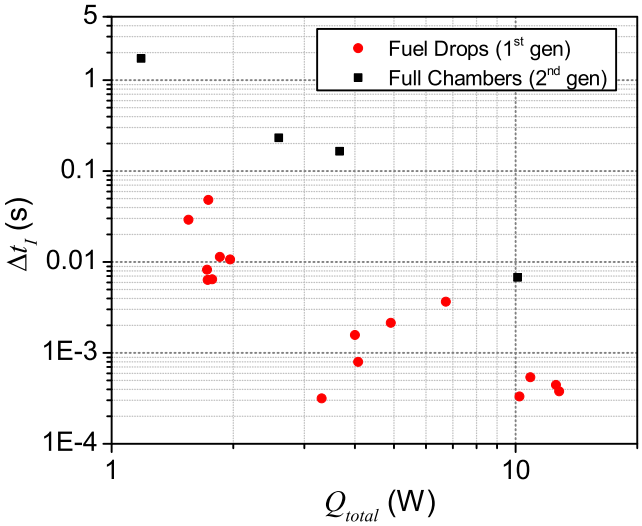

Figure 5.22: Ignition delay time vs. input power for the shadow mask igniters over fuel drops (1^{st} gen., red circles) and over full fuel chambers (2^{nd} gen., black squares).

metal to be evaporated—> 1000 nm, using a rotary-planetary substrate holder—in order to yield controllable igniter resistances and reliable fuel ignition.

2. *Fuel shrinkage.* After fuel deposition, the chips are placed in an oven at 120 °C in order to evaporate the solvent and cure the binder. During this step, the fuel volume shrank by ~ 50 %, making it difficult to accurately control the amount fuel deposited on the chamber and obtain a flat fuel surface on which to deposit the igniter. The primary cause of igniter failure was line discontinuities at the sharp edge of the chamber wall. We attempted to overcome this problem by slightly overfilling the chambers, but this was difficult to control.

A summary table of the shadow mask igniter performance is given in table 5.5). For the evaporators fabricated on fuel droplets (1^{st} generation devices), ignition success rates of up to 100 % and complete combustion in 60 % of the devices was achieved. The major cause of combustion failure was quenching due to the small size of the fuel drops—not due to the igniter itself. For the full fuel chamber devices (2^{nd} gen.), only 5 out of 14 devices were successfully ignited due to igniter discontinuities at the chamber wall edge. All of the successfully ignited devices maintained self-sustained combustion without quenching. The shadow mask ignition reliability was relatively poor, although the fabrication is far from optimized—the goal of this study was to demonstrate the proof-of-concept, not optimize the performance. There are many ways to optimize the fabrication process, we plan to investigate two in particular:

1. *Reduce shadow mask offset height.* Reducing the offset height will improve the resolution of the evaporated igniters by reducing the amount of under-evaporation that occurs. In

addition, reducing the offset height will enable the line width to be reduced as well and therefore, the amount of input power required for ignition. In order to do so, the fuel deposition process needs to be better controlled or an extra processing step needs to be performed to planarize the fuel drop—i.e., raking the drop flat.

2. *Sharp chamber edge.* The inability to conformally coat the sharp chamber wall edges with metal was the primary cause of igniter failure for the full chamber devices. The 90° walls can be avoided all together by etching the chambers with potassium hydroxide (KOH) in a two-step process (one maskless) to eliminate the sharp edge [57].

Table 5.5: Comparison of the shadow mask igniter performance with the literature.

	Q_{total} (W)		Δt_I (s)			
Type	min	max	min	max	error	Reference
Shadow mask						
Fuel drop (1500 nm)	1.7	11.8	0.0003	0.048	N/A	chap 5
Full chamber	1.18	10.1	0.0068	1.730	N/A	
Hot spot						
Glass	0.85	2.67	0.0001	9.5	25 %	chap 4
Polyimide	0.28	0.58	0.0003	2.3	~ 100 %	
Membrane						
SiO_2/SiN_x	0.065	0.5	0.025	1	N/A	[21]
SiO_2/SiN_x	0.08	0.15	0.020	0.75	~ 100 %	[15]
Foturan	0.22	0.8	0.025	0.625	N/A	[17]
In-plane						
Ceramic (LTCC)	1.3	1.3	0.630	2	~ 54 %	[28]
Glass	0.16	0.16	12.94	12.94	N/A	[29]

5.6 Conclusion

Shadow-mask evaporated pyroMEMS igniters were successfully demonstrated using fuel-drop-coated glass substrates. This represents a first step in developing simpler top-side pyroMEMS igniters; however, the fabrication process needs to be further optimized and more propellants need to be tested to evaluate the broader suitability of this fabrication technique for pyroMEMS devices.

We envision a final device architecture consisting of only three parts: a substrate containing fuel-filled cavities, the shadow-mask evaporated top-side igniters and microfabricated nozzles. The complete device can potentially be assembled at the wafer scale—using low-temperature bonding—and diced with the nozzles protected using dicing tape—"blue tape"—to protect the fuel from the cooling water.

The shadow mask igniters represent an attempt to further integrate the solid propellant into the cleanroom fabrication process in order to simplify the overall device fabrication. In the next chapter, the opposite approach will be taken: the pyroMEMS fabrication process will be carried out using cleanroom-free (compatible) processing.

6 PyroMEMS Balloon Actuator

6.1 Introduction

As a final validation of the work presented in this thesis, a pyroMEMS balloon actuator was modeled (using the ICT code validated in chapter 3), designed (using the lessons learned from chapter 4) and fabricated. A semi-analytical predictive model was constructed and successfully used as a design tool to size the devices and predict their performance. Low-cost, foil-level fabrication methods were used to make the pyroMEMS balloon actuators.

A pyroMEMS balloon actuator is composed of an elastic membrane enclosing a fuel-covered igniter inside a combustion chamber (see figure 6.1a). Upon ignition of the solid propellant, the combustion gases expand and inflate the membrane out-of-plane (figure 6.1b). This high-energy balloon actuator can be used as an on-chip fluid actuator in microfluidic chips [23, 34, 36, 37] or as a fluid ejector for drug injection applications [12, 13, 31, 34] (figure 6.2). PyroMEMS are ideally suited to microfluidic or medical applications because both have many single-use applications. In order to easily and efficiently integrate—or ideally co-fabricate—pyroMEMS balloon actuators with microfluidic devices, they should be fabricated in the same manner and with the same materials.

Recently, there has been a push to fabricate microfluidic chips outside the cleanroom, using low-cost materials—e.g., silicones and epoxies—and replication techniques, such as soft lithography [58]. As such, one of the goals in this chapter was to leverage low-cost, cleanroom-free and "microfluidic-compatible" fabrication techniques to make the balloon actuators. Previous pyroMEMS balloon actuators have been made using standard cleanroom techniques and materials [23, 31]. The igniters were fabricated on glass substrates using photolithography and e-beam evaporation—like the igniters in chapter 4. The combustion chambers were made of deep reactive ion etched silicon and the membrane was made of silicone—polydimethylsiloxane (PDMS).

In our case, the pyroMEMS igniters were fabricated by inkjet-printing of a conductive silver ink on a polyethylene terephthalate (PET) foil. However, in order to reduce the current densities

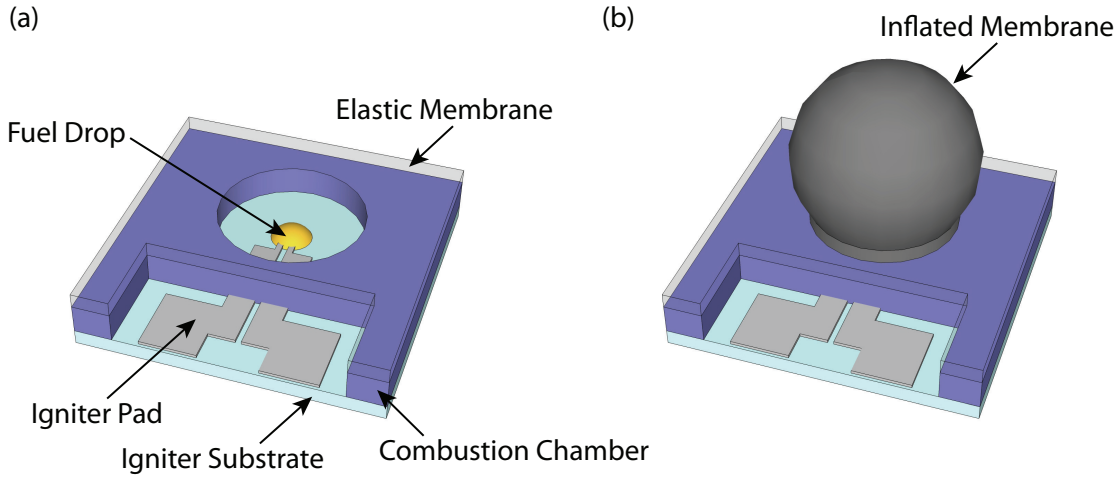

Figure 6.1: Sketch of a pyroMEMS balloon actuator (a) before and (b) after actuation showing the large out-of-plane displacement of the inflated membrane.

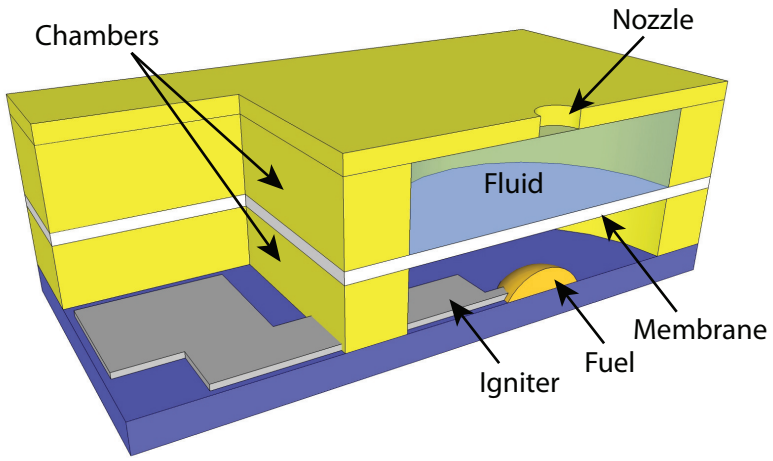

Figure 6.2: Sketch of a pyroMEMS balloon actuator used as a fluid ejector for drug injection applications.

in the igniters during ignition, the igniters were electroplated with nickel to increase their thickness. The combustion chambers were fabricated using a thick (~ 750 μm) photodefinable dry epoxy film. This epoxy film is basically the dry-film equivalent to the commonly used SU-8 epoxy for microfluidic devices. Lastly, the elastic membranes were made of PDMS. All of these materials and their processing was cleanroom-free compatible.

6.2 Fabrication

The device consisted of three different layers: (1) a plastic foil with a fuel-covered, inkjet-printed igniter, (2) an epoxy combustion chamber, and (3) a PDMS membrane. Each layer was processed individually—at the foil level—and assembled together in one step. The epoxy dry film acted as both structural layer—the combustion chamber—and adhesive. Prior to lamination the layers were diced/cut into 2 × 2 arrays of balloon actuators to facilitate handling. 56 inkjet-printed pyroMEMS igniters were fabricated, of which 29 pyroMEMS balloon actuators were assembled and tested—the remaining igniters were used for various characterizations (e.g., electrical stress testing, temperature coefficient of resistance, ignition and combustion behavior). Two different binder mass fractions—10 % and 20 %—were investigated and three different chamber heights—750, 1500 and 2250 μm. The membrane diameter (5 mm) and membrane thickness (~ 90 μm) were not varied.

6.2.1 Igniters

The pyroMEMS igniters were fabricated using cleanroom-free, low-cost, additive methods only—inkjet printing and electroplating. Inkjet printing presents many advantages over standard cleanroom metallization methods:

1. *Maskless.* Inkjet printing does not require any masks to define the deposition pattern, making it easy to prototype devices and modify deposition layouts.

2. *Additive.* With additive fabrication techniques, such as inkjet printing, the metallization is only added where it is needed, reducing fabrication costs and material waste.

3. *Cleanroom-free.* By-passing the cleanroom greatly reduces fabrication costs and adds more freedom with respect to the materials and processes that can be used to fabricate the devices.

However, inkjet printing does have limitations, mostly in terms of feature resolution (min. ~ 50 μm) and materials available to print—certain metal colloids, such as silver and gold, and some polymers. Obtaining large thicknesses and small features can also be a challenge; for this reason we coupled inkjet-printing with electroplating in order to obtain thick metallizations.

Layout

The igniters consisted of a single annular igniter, two wide interconnects—to minimize any stray heating—and two large contact pads (figure 6.3). The annular shape was chosen based on the results from chapter 4, indicating that the annular shape helps prevent fuel ejection. However, the lower line resolution used in these tests limited the geometry of the igniter and precluded the addition of hot spots—the igniter geometry will be optimized in the future. The heated area measured roughly 1.5 mm × 1.5 mm with a nominal line width of 200 μm. The igniters were all shorted together electrically for nickel electroplating. Prior to lamination, those connections were removed manually with a scalpel. However, it is possible—using a smarter design—to have these connections automatically severed when the devices are diced.

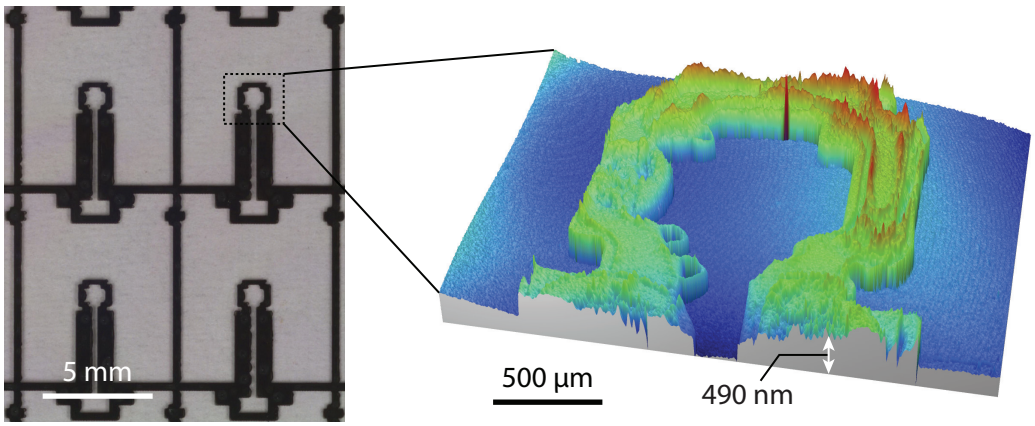

Figure 6.3: (a) Photo of a 2 × 2 array of inkjet-printed and electroplated igniters on a PET foil. Inset: White-light interferogram of the igniter showing the thickness profile.

Process

The high-temperature igniters were fabricated using a two-step process: first, 2 layers of silver nanoparticles were inkjet-printed onto the plastic foil (thickness ~ 180 nm), followed by a 500-nm (nom.) nickel electroplating of the igniters. As will be shown below, the inkjet printed devices alone were not able to sustain the large current densities (~ 1×10^6 A/cm^2) required for propellant combustion; therefore, the nickel-plating was added.

The devices were fabricated on a 125-μm thick polyethylene terephthalate (PET) foil (Dupont Melinex ST506). PET was chosen due to its low cost, commercial availability and its suitability for inkjet printing. Prior to printing, the substrates were dehydrated for a minimum of 1 hour

in an oven at 120 °C and then treated with microwave oxygen plasma (PVA TePla PS210) for 4 minutes (400 sccm, 400 W).

Inkjet printing was carried out using a Dimatix DMP-2800 printer with 10 pl drop cartridges and a commercially-available silver-nanoparticle ink (DGP 40LT-15C by Anapro). The printing parameters are given in table 6.1.

Table 6.1: List of inkjet printing process parameters.

Parameter	Value
# of Nozzles	3
# of Printed Layers	2
Drop Size	10 pL
Drop-to-Drop Spacing	40 μm
Drop Jetting Frequency	1 kHz
Drop Jetting Speed	3.5 m/s
Nozzle Translation Speed	4 cm/s
Substrate Temperature	50 °C
Curing Time	60 min
Curing Temperature	150 °C

The nickel electro-deposition process was done in a nickel sulfamate bath at 54 °C under an electrical current density of 20 mA/cm^2. Nickel was used as the plating material because it was readily available.

Propellant

Two different binder mass fractions were tested in these devices: 10 and 20 %. The 10 % binder fuel drops weighed 312^{+132}_{-0} μg, while the 20 % binder drops weighed 418^{+86}_{-0} μg. The drop measured 2.0 ± 0.2 mm in diameter. A fabricated array of nickel-plated igniters on a PET substrate with deposited fuel drops is shown in figure 6.4.

6.2.2 Combustion Chambers

The balloon actuator chambers were fabricated using 750-μm thick epoxy sheets (SUEX™ by DJ DevCorp) [59]. The SUEX sheets were developed for wafer-level packaging, thick plating molds and as a structural material for microfluidic devices, among others. The combustion chamber process flow is detailed in table 6.2.

The combustion chambers measured 5 mm in diameter and the contact pad openings were 5 mm × 2 mm (see figure 6.5). The usual post-exposure bake was not performed, instead it was replaced by the lamination step. The deep striations visible in the epoxy chambers disappeared after lamination (see figure 6.6). Thicker chambers were realized by stacking and laminating multiple sheets at the same time.

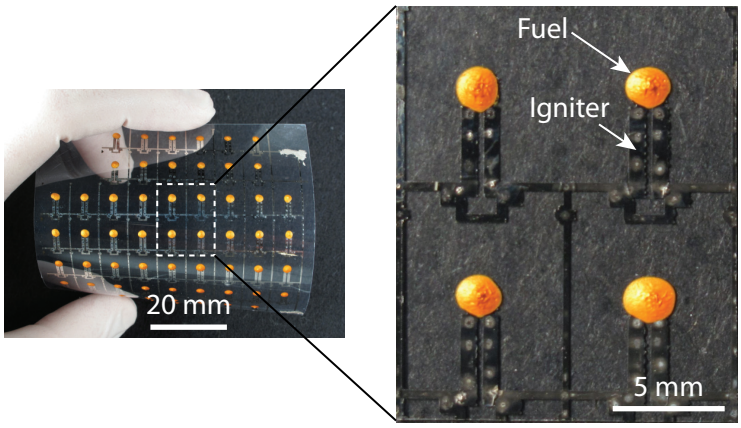

Figure 6.4: Photo of an array on nickel-plated igniters with deposited fuel drops. Inset: Close-up of a 2 × 2 array of igniters.

Table 6.2: 750 μm-thick SUEX combustion chamber process flow.

#	Parameter	Value
1	Exposure	2250 mJ/cm^2 (Non-contact)
2	Post-Exposure Bake	30 min @65 °C
3	Development	150 min in PGMEA

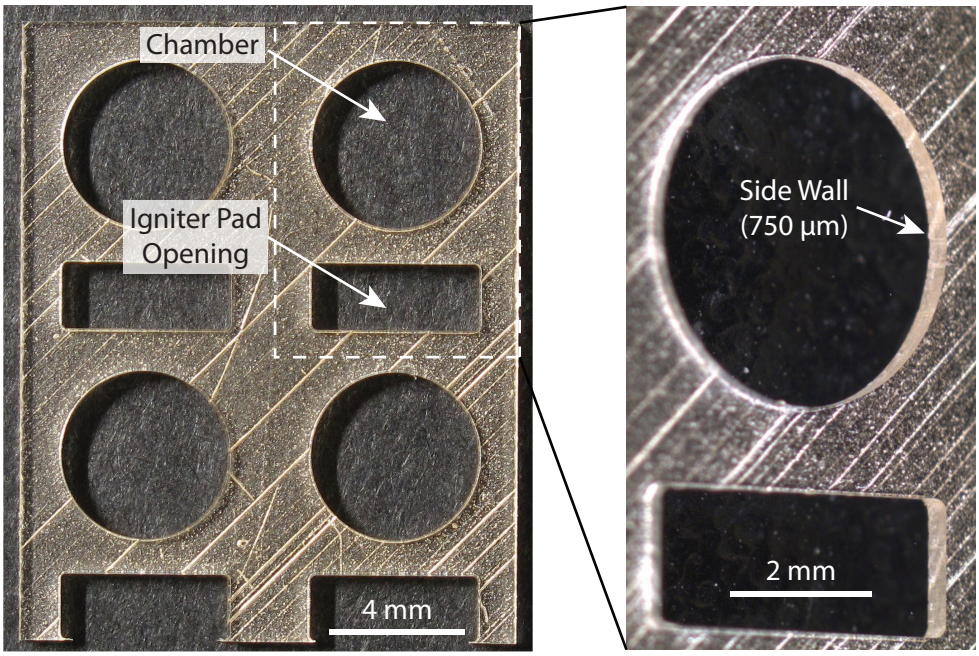

Figure 6.5: (a) Photo of a 2 × 2 array of SUEX photodefinable dry film epoxy combustion chambers and (b) a close up showing the vertical chamber side walls.

In this work, we made use of a chrome photomask and a mask aligner to pattern the SUEX chambers, although it is possible to avoid the cleanroom altogether by making use of a transparency mask and a UV lamp—due to the large size of the features involved. The cleanroom was used simply out of convenience.

6.2.3 PDMS Membranes

The elastic membranes were made of PDMS (Sylgard® 186 by Dow Corning) with a 10:1:5.5 mix ratio (base:catalyst:iso-octane). The elastomer was degassed under vacuum for 30 min and cast by pouring it on a 50-μm thick polyimide (PI) sheet (Kapton® E by Dupont) and leveled using a ZUA 2000 universal applicator (Zehntner GmbH). The PDMS sheets were cured for 4 hours at 65 °C. The PDMS membrane thickness (92.7 ± 9.8 μm) was measured on its PI handling foil before lamination using a white-light interferometer (Wyko NT1100 by Veeco).

PDMS is well adapted for use in balloon actuators: it is readily processed into thin membranes, is highly elastic and resistant to tearing. However, it is permeable to gases, leading to leakage of the combustion products through the membrane. In order to decrease the leak rate of the PDMS membranes, a 100-nm thick (nominal thickness; 0.35 g of dimer) parylene-C sealing layer was deposited by chemical vapor deposition as a last step after lamination [60]. The parylene-C thickness was measured—on a dummy silicon substrate—to be 68.2 ± 1.7 nm.

6.2.4 Lamination

Lamination of the different layers was carried out in a temperature-controlled press. Prior to lamination, the PET foil was carefully cleaned with isopropanol and de-ionized water to remove traces of fuel, dirt and dust on the surface. Next, silanization of the epoxy chambers was carried out using (3-aminopropyl)triethoxysilane (APTES) to improve adhesion to the PDMS membrane. The PDMS membrane surface was activated with 15-second oxygen plasma treatment (400 sccm, 400 W) and the complete stack was immediately assembled. The stack was then placed into the press, loaded with 200 N (~ 5 bars) and heated for 90 min at 120 °C—i.e., the standard hard-bake conditions for the SUEX chambers. A bonded, 2×2 matrix of pyroMEMS balloon actuators is shown in figure 6.6. Stacks containing up to 3 epoxy layers were successfully bonded (see figure 6.7)—taller stacks were not tested.

6.3 Characterization

6.3.1 Inkjet-Printed Igniters

The nickel plated igniter resistance was 6.05 ± 1.83 Ω. The relatively large variance in the resistance values was due to the poor feature definition. The printing parameters were far from optimized and will be improved in the future. The igniter thickness was 570 ± 100 nm and the line width was approximately 285 ± 60 μm for a cross-sectional area of 162 ± 44 μm^2

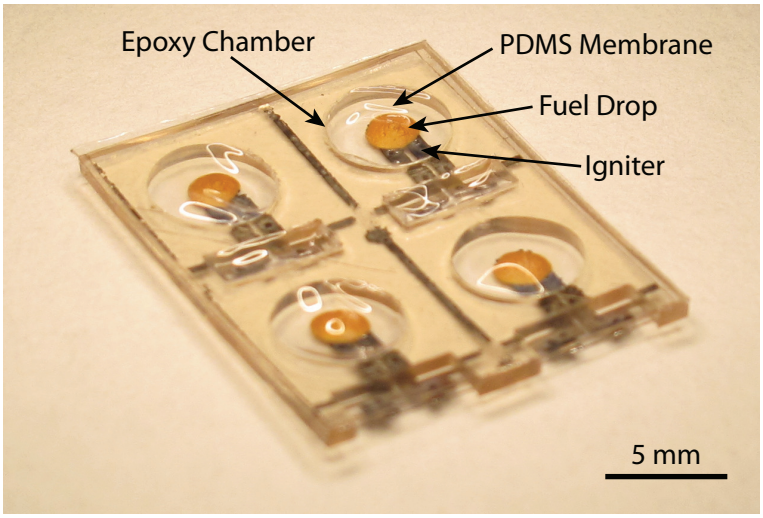

Figure 6.6: Photograph of a 2×2 array of pyroMEMS balloon actuators.

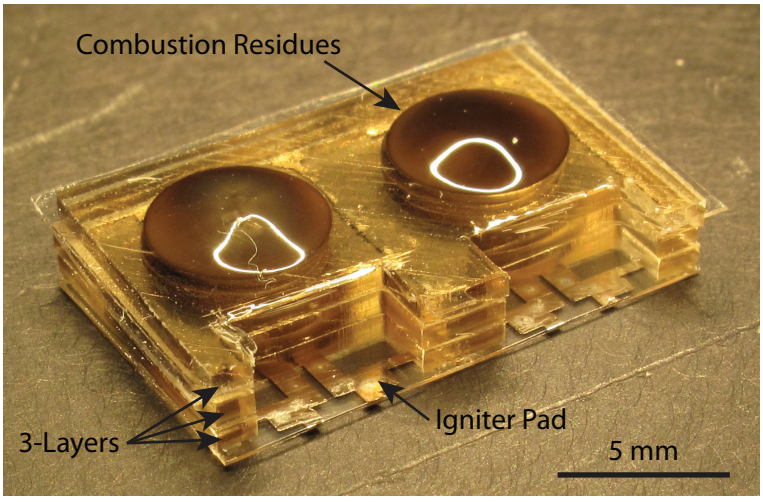

Figure 6.7: Photograph of a 1×2 array of pyroMEMS balloon actuators after combustion (3-layer thick chambers).

(see figure 6.3).

Temperature Coefficient of Resistance

The temperature coefficient of resistance (TCR) of the silver inkjet-printed igniters—with and without Nickel plating—was measured in a temperature-controlled oven under nitrogen atmosphere (Vacucenter by SalvisLab). The temperature accuracy of the oven is rated at 0.1 °C. The resistance of the igniters was measured using the 4-wire method to isolate the igniter resistance from the effects of the wires—which are not at the same temperature as the igniter. The oven was ramped in steps with 2 hour hold periods to allow the igniter to reach thermal equilibrium before the resistance measurements were taken. The measurements were taken from room temperature up to ~ 170 °C.

The increase in resistance with temperature for both the plated and non-plated igniters was extremely linear (R^2 = 99.997 % and R^2 = 99.88 %, respectively). The temperature coefficient of resistance (based on a reference temperature of 23 °C) was 271.4 ppm/°C and 60.8 ppm/°C for the 500-nm nickel plated and non-plated igniters, respectively.

Maximum power

Inkjet-printed silver igniters—with and without nickel plating—were tested to determine their maximum power before failure. The bare inkjet-printed igniters could not sustain these power levels—failing after 100 ms at 0.6 W—whereas the nickel-plated igniters performed nominally at 2.5 V (~ 1 W) for 1 s (see figure 6.8).

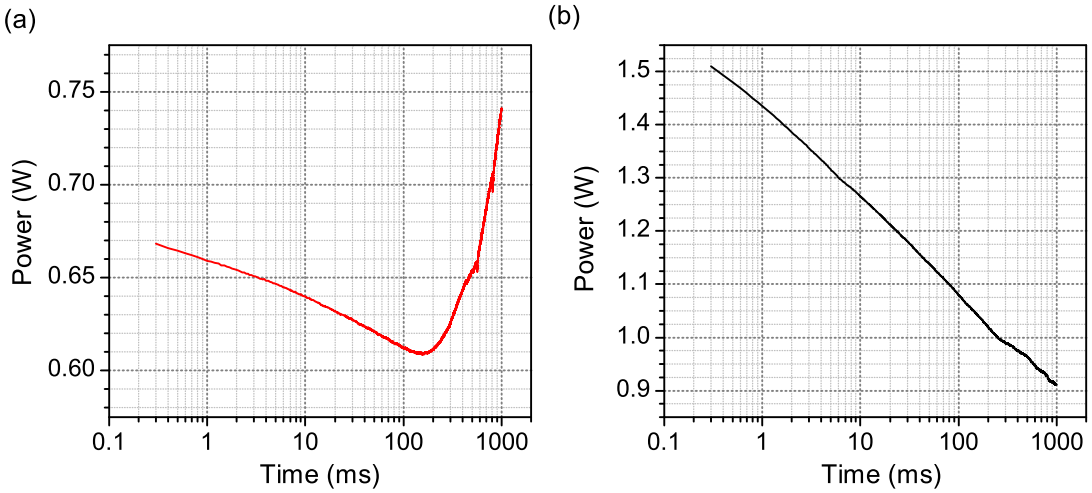

Figure 6.8: Igniter power dissipation (constant voltage). (a) The bare inkjet-printed igniter began failing after 100 ms at 0.6 W, while (b) the 500 nm Ni-plated igniter dissipated ~ 1 W of power over 1 s.

Long-Term Electrical Stress Tests

The nickel-plated igniters were subjected to long-term—1 hour—electrical stress tests to analyze the stability of the igniters under a constant current load (see figure 6.9). Given that the devices are expected to operate for less than 1 s, 1 hour represents a long-term test for our needs.

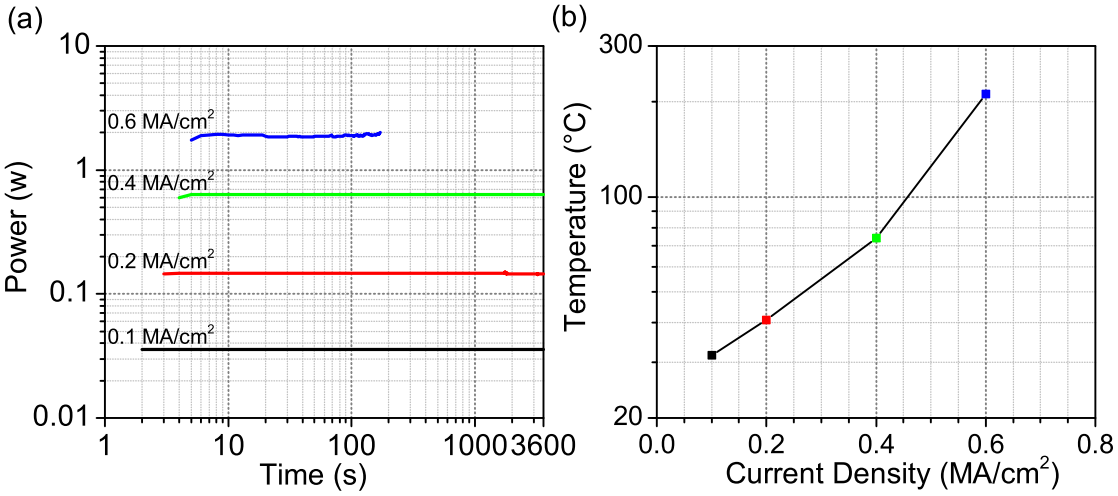

Figure 6.9: (a) Igniter dissipated power vs. time for different input current densities (Nickel-plated igniters). (b) Igniter temperature vs. current density.

The igniters were found to operate nominally without failing for current densities of at least 0.4 MA/cm^2 for 1 hour. For 0.6 MA/cm^2, or ~ 2 W of input power—i.e., significantly more than is required for ignition—the igniters functioned nominally for nearly 200 s. Based on measured TCR values above, we estimated the maximum igniter temperature as a function of applied current density, obtaining a temperature of 211 °C at 0.6 MA/cm^2 (figure 6.9b). However, these values are error prone for two reasons: (1) the highest temperatures obtained are beyond the range used to determine the TCR (up to ~ 170 °C) and (2) the igniters are not at a single, uniform temperature: the heating was concentrated around the annular igniter, as opposed to the interconnects. As such, temperature values based on the overall igniter resistance will underestimate the actually igniter temperature.

An SEM picture of a failed igniter clearly shows the failure mechanism to be igniter rupture due to melting of the underlying PET foil (see figure 6.10). Other than the hole in the substrate, the igniter showed no signs of damage, indicating that the substrate failed rather than the igniter. Based on the manufacturers datasheet, the PET foil melting temperature is 265 °C—further evidence that the temperature values in figure 6.9b were underestimated. Furthermore, the small heat affected zone in the vicinity of the annular igniter (indicated by the black dashed line) showed the igniter was able to deliver localized heating to the fuel drop. The substrate around the interconnects showed no signs of melting.

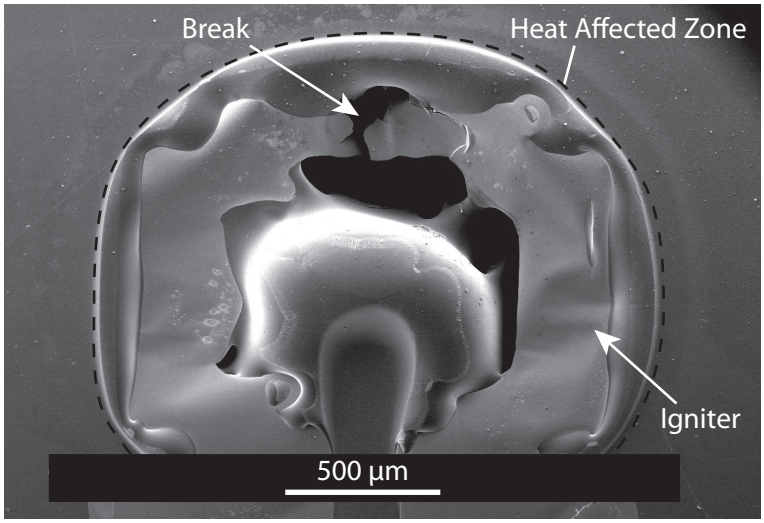

Figure 6.10: SEM picture of a failed nickel-plated igniter (applied current density = 0.6 MA/cm^2).

6.4 Modeling

A complete semi-analytical model of the pyroMEMS balloon actuator was developed. The model served two important functions:

1. *Design.* A pyroMEMS balloon actuator inflates a ~ 100 μm-thick elastic membrane with high-pressure combustion products in less than 100 ms in order to generate large deformations. If not properly designed, the combustion products can easily rupture the thin membrane. The model enabled us to obtain functioning balloon actuators on the first attempt.

2. *Performance Prediction.* The model also served to predict the maximum vertical displacement of the balloon, in order to compare with experiments. The model was used to determine the effect of changing the initial chamber volume as well as adding a sealing layer to the permeable PDMS membrane.

6.4.1 Assumptions

The following assumptions were made when constructing the pyroMEMS balloon actuator model:

1. *Constant Volume Combustion.* The combustion was assumed to occur under constant volume conditions. This assumption was imposed by the ICT code (see chapter 3). It effectively decoupled the fuel combustion from the membrane inflation.

2. *Calorically Perfect Gas.* The products of combustion were assumed to be calorically

perfect gases, i.e., they obey the law of ideal gases and have constant heat capacities.

3. *Adiabatic Walls.* All the chamber walls and the membrane were assumed adiabatic.

4. *Leak-free Membrane.* No mass transfer across the membrane.

5. *Incompressible Membrane.* The membrane was assumed to behave as an incompressible solid.

6. *Constant Membrane Properties.* The effect of the combustion event—high temperature, shock impact—on the material properties of the membrane were ignored.

7. *Thin Membrane.* The membrane thickness was much smaller than the radius of the balloon (i.e., $r/t \geq 10$), thus rendering radial stress σ_{rr} negligible compared to the hoop stress $\sigma_{\theta\theta}$.

8. *Spherical Cap Membrane.* The inflated shape of the membrane was assumed to be a spherical cap, generating a biaxial membrane stress, i.e., $\sigma_{\phi\phi} = \sigma_{\theta\theta}$. Effects of gravity and clamping stresses on the membrane were ignored.

6.4.2 Modeling Strategy

The assumptions of constant volume combustion and isolated system—no heat or mass losses to the environment—effectively break down the pyroMEMS balloon actuation into three steps: (1) fuel combustion, (2) by membrane inflation (mechanical relaxation) and finally, (3) cool down to thermal equilibrium. As such, the dynamics of the balloon actuation cannot be captured by this model. That would require a full finite element model with moving mesh to model the membrane, coupled with a chemical kinetics program to simulate the fuel combustion. Such a model is highly complex and computationally demanding. As such, it would not be as useful as a design tool.

Our time-invariant model is shown schematically in figure 6.11. First, the constant volume combustion was simulated using the ICT Thermodynamics Code presented in chapter 3. Second, the combustion gases were allowed to expand adiabatically against the thin membrane. Mechanical equilibrium was reached when the force exerted by the pressurized gases equalled the stress generated by stretching the membrane. This equilibrium position was assumed to represent the maximum possible membrane deflection, since heat losses and gas leakage from the system were neglected. Lastly, the combustion gases was cooled to room temperature and the final equilibrium membrane position was computed.

6.4.3 Membrane Stress Distribution

In order to determine the final shape of the inflated membrane, we must develop relations between (1) the state of stress in the membrane due to the applied loads and (2) the constitutive equation—i.e., stress/stretch relations—for the membrane. The goal is to be able to predict

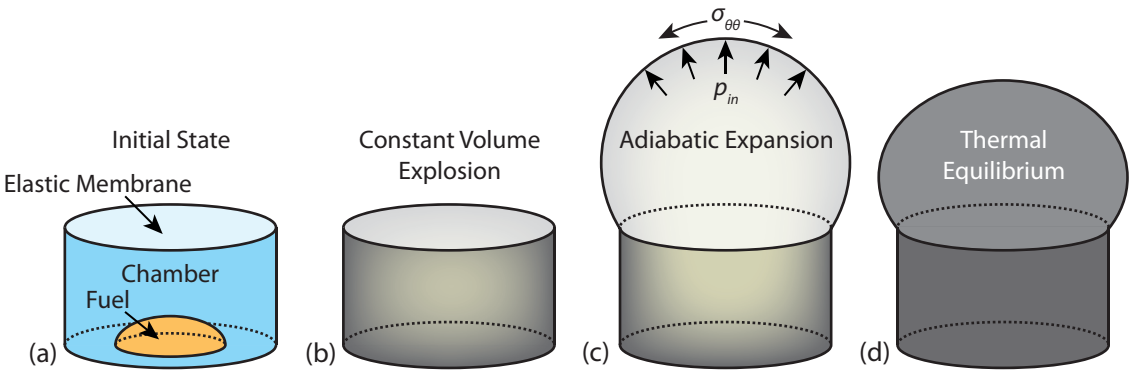

Figure 6.11: Sketch showing the pyroMEMS balloon actuator modeling strategy. (a) Initial state; (b) After an adiabatic, constant volume combustion of the fuel; (c) after an adiabatic expansion of the products against the elastic membrane; and finally, (d) the final membrane position at thermal equilibrium.

the final equilibrium shape of the membrane for a given combustion chamber pressure and temperature. For our model, the final shape parameter of interest is the height of the balloon—as opposed to balloon radius or membrane stretch—because it is the easiest parameter to extract from the high-speed videos of the membrane inflation.

State of Stress

Based on the thin-shell and spherical balloon membrane assumptions, the stress tensor for the membrane contains only one non-zero term, the hoop stress, given as

$$\sigma_{\theta\theta} = \frac{\Delta P \cdot r}{2e} + \sigma_0 \tag{6.1}$$

where ΔP is the combustion chamber overpressure, r is the radius of curvature of the membrane, e is the membrane thickness and σ_0 is the intrinsic stress in the membrane. However, as the membrane is stretched, its thickness decreases due to conservation of mass. Assuming the volume of the membrane is conserved, the thickness of the membrane stretched membrane e becomes

$$e = \frac{e_0}{\lambda_{\theta\theta}^2} \tag{6.2}$$

where e_0 is the initial membrane thickness and $\lambda_{\theta\theta}$ is the membrane biaxial stretch, which is

defined as

$$\lambda_{\theta\theta} \equiv \frac{l}{l_0} = \frac{l}{2a} \tag{6.3}$$

where $2a$ is the unstretched membrane diameter and l is the arc length of the stretched membrane—i.e., the same line segment $2a$, but stretched. Combining (6.1) and (6.2) yields

$$\sigma_{\theta\theta} = \frac{\Delta P r \lambda_{\theta\theta}^2}{2e_0} + \sigma_0 \tag{6.4}$$

Based on the spherical cap geometry of the membrane (see figure 6.12), the membrane stretch can be expressed in terms of membrane height h and initial radius a using the following relations

$$l = \begin{cases} 2\theta r & \text{for } h < a, \\ 2(\pi - \theta) r & \text{for } h \geq a, \end{cases} \tag{6.5}$$

$$\theta = \sin^{-1}\left(\frac{a}{r}\right) \tag{6.6}$$

$$r = \frac{a^2 + h^2}{2h} \tag{6.7}$$

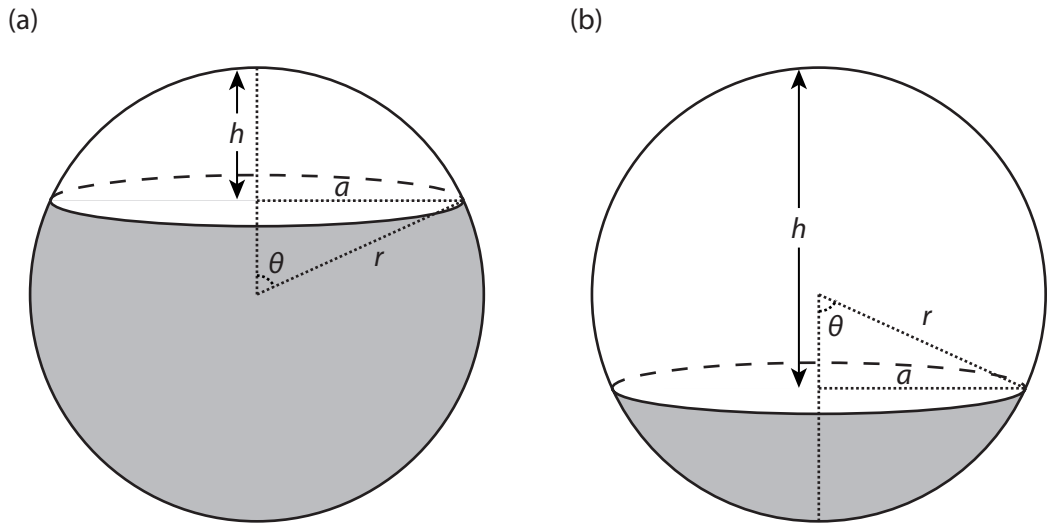

Figure 6.12: Sketch of spherical cap membrane geometry: (a) case when $h < a$, and (b) case when $h \geq a$.

Substituting equations (6.5), (6.6) and (6.7) into (6.3), we can express the biaxial stretch $\lambda_{\theta\theta}$ in terms of a and h:

$$\lambda_{\theta\theta} = \begin{cases} \frac{a^2+h^2}{2ah} \sin^{-1}\left(\frac{2ah}{a^2+h^2}\right) & \text{for } h < a, \\ \frac{a^2+h^2}{2ah}\left[\pi - \sin^{-1}\left(\frac{2ah}{a^2+h^2}\right)\right] & \text{for } h \geq a, \end{cases} \tag{6.8}$$

In this section, we have developed a set of equations to determine the membrane hoop stress $\sigma_{\theta\theta}$ for a given applied pressure ΔP and a given membrane shape—i.e., a and h. Next, we need to determine the deformation induced by a given applied stress. This relation is called the material's constitutive relation.

Stress-Stretch Constitutive Relation

A constitutive relation is a connection between two physical quantities that is specific to a material or substance, and approximates the response of that material to external forces. Some constitutive relations are phenomenological—based on empirical observations—others are derived from first principles, while others still are hybrids of the two.

The stress-stretch constitutive relation relates the stress applied to a material with its observed deformation. PDMS is a hyperelastic material, which exhibits strongly non-linear stress/strain behavior. For this work we chose a phenomenological model known as the Yeoh hyperelastic material model. The material was assumed incompressible and under pure biaxial loading. Furthermore, the model was truncated at 3 terms for simplicity. The details of the model can be found in [61]. The functional form of the model is

$$\sigma_{\theta\theta} = 2\left(\lambda_{\theta\theta}^2 - \frac{1}{\lambda_{\theta\theta}^4}\right)\sum_{i=1}^{3} i \cdot C_i (I_1 - 3)^{i-1} \tag{6.9}$$

where the C_i's are the empirical fitting parameters and I_1 is the first strain invariant, which for biaxial stress is

$$I_1 = 2\lambda_{\theta\theta}^2 + \frac{1}{\lambda_{\theta\theta}^4} \tag{6.10}$$

Bulge Test

In order to determine the 3 fitting parameters in the Yeoh model—and the instrinsic stress σ_0—bulge test measurements were made on PDMS and parylene-C coated PDMS membranes. In a bulge test measurement, the deflection of a clamped membrane is measured as a function of the applied pressure. For these measurements, the elastic membranes were laminated onto epoxy combustion chambers without the igniter foil. The epoxy chambers were then glued to an aluminum plenum chamber that was connected to a pressure controller (Druck DPI 510). At each pressure step, a delay of one minute was taken to allow the membrane deflection and pressure level to reach equilibrium. The measurements were made on virgin membranes and carried out until failure.

The hoop stress in the membrane was calculated using (6.4). The biaxial stretch in the membrane was measured by taking photographs of the deflected membrane and using image processing software to measure the arc length of the balloon cross-section. For this, a custom MATLAB program was created fit the periphery of the deflected membranes (see figure 6.13).

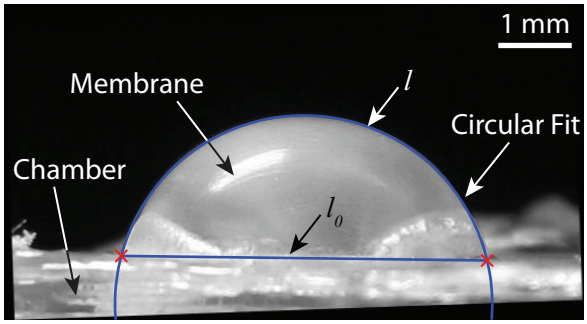

Figure 6.13: Picture of a membrane pressurized at 300 mbar after image processing (5 mm-diameter, parylene-C coated PDMS). The membrane shape was fitted to a circle and the biaxial stretch l/l_0 was extracted.

For small deflections, a circular fit was applied; however, for stretches greater than 1.5, the membrane deflection deviated from a circle. In order to correct for this deviation, elliptical fits were applied to the membrane to calculate the biaxial stretch (see figure 6.14). For stretches of greater than 3, the deformation caused by the clamping stress was substantial and those data points were not used for the constitutive model fitting (figure 6.15).

The resultant stress-stretch data and hyperelastic model fits are shown in figure 6.16. The fitted parameters are given in table 6.3. The fits were in good agreement with the data—R^2 = 99.99 % and R^2 = 99.86 % for the PDMS and parylene-C coated PDMS membranes, respectively. The membrane failure was found to occur for stretch of ~ 3.45.

The individual fitting parameters varied significantly, however, there was little overall difference in the stress/stretch curves of the membranes due to the addition of the ~ 70-nm thick parylene-C layer.

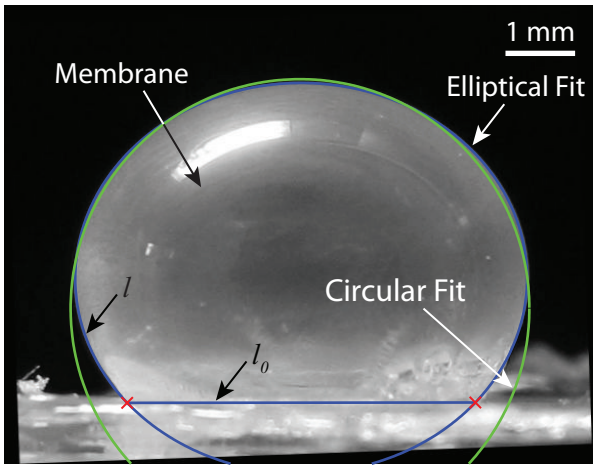

Figure 6.14: Picture of a membrane pressurized at 500 mbar after image processing (5 mm-diameter, parylene-C coated PDMS). The membrane shape was fitted to an ellipse (blue curve) and the biaxial stretch l/l_0 was extracted (circular fit (green curve) shown for comparison).

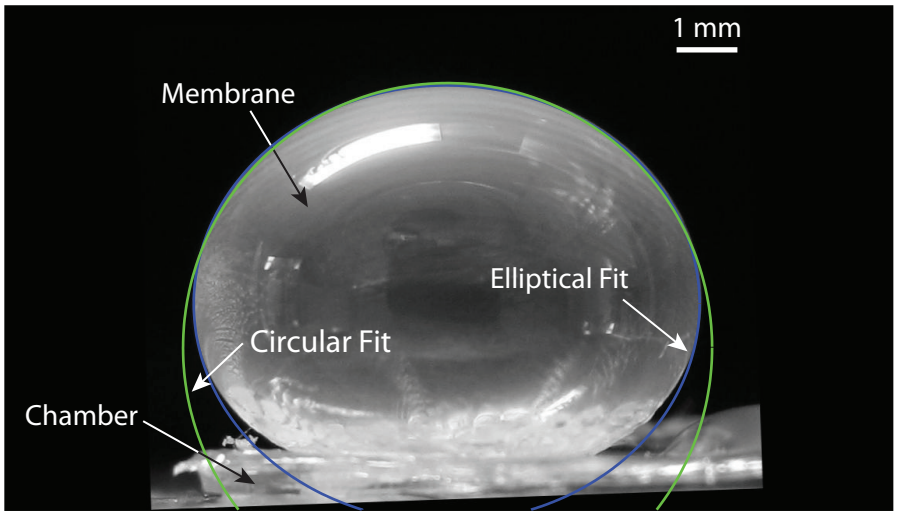

Figure 6.15: Picture of a membrane pressurized at 750 mbar after image processing (5 mm-diameter, parylene-C coated PDMS). The membrane shape was incompatible with both circular (green curve) and elliptical (blue curve) fits.

Table 6.3: Yeoh model fit parameters (PDMS and parylene-C coated PDMS).

Parameter	PDMS	PDMS + Parylene-C
C_1 (mbar)	1900 ± 200	3000 ± 3000
C_2 (mbar)	100 ± 40	-50 ± 200
C_3 (mbar)	8 ± 2	10 ± 6
σ_0 (mbar)	1000 ± 300	-2000 ± 9000
s_ϵ (mbar)	200	2000
R^2	99.99 %	99.86 %

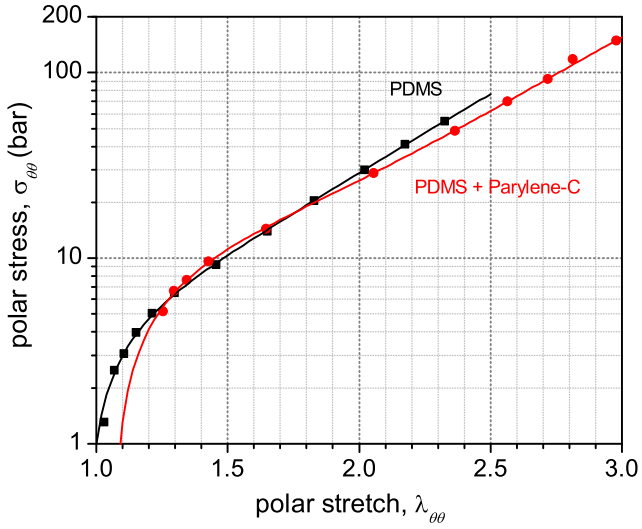

Figure 6.16: Stress-Stretch curves with Yeoh model fits (PDMS and parylene-C coated PDMS).

6.4.4 Algorithm Implementation

The model was implemented in three steps: first the final pressure of the products of combustion was determined using the ICT Thermodynamic Code (presented in chapter 3); second, the equilibrium deflection of the membrane is computed; and third, the final membrane deflection is calculated with the products cooled down to room temperature. The two final steps were carried out using a custom MATLAB code (see appendix B). The equilibrium deflection of the membrane is achieved when the force induced by the applied pressure is equal to the stress in the membrane, that is

$$P_{atm} + \frac{2e_0}{r\lambda_{\theta\theta}^2}(\sigma_{\theta\theta} - \sigma_0) = P_i\left(\frac{V_i}{V_f}\right)^{\gamma} \tag{6.11}$$

where γ is the ratio of specific heats, V_i is the combustion chamber volume and V_f is the final total volume under the inflated membrane, given as

$$V_i = 2\pi a h_c \tag{6.12}$$

$$V_f = V_i + \frac{\pi h}{6}(3a^2 + h^2) \tag{6.13}$$

P_{atm} is the atmospheric pressure and h_c is the chamber thickness. Both $\sigma_{\theta\theta}$ and V_f are

functions of the membrane height h; therefore we solve for the maximum inflation equilibrium height h^*_{max} using a bisection root-finding algorithm (see appendix C). Although faster root-finding algorithms exist, it was chosen due to its simplicity to code and its robustness [62].

Since $\lambda_{\theta\theta}$ is represented by a different expression depending on whether h is larger or smaller than a (see (6.8)), the algorithm was implemented in two steps: first, h was assumed smaller than a and the bisection algorithm was carried out between 0 and a. If the algorithm failed to converge, then the expression for h was modified for the case where h was larger than a and the search was conducted between a and an arbitrarily large value, e.g., $h = 50a$.

Finally, the pressure of the combustion products at room temperature is determined using the perfect gas law:

$$P_f = \frac{n_f R T_f}{V_f} \tag{6.14}$$

where R is the universal gas constant, T_f is the final equilibrium temperature—298 K—V_f is the final volume and n_f is the number of moles of gas generated by the fuel combustion at 298 K—which is given by the ICT code output (see appendix A). This final pressure is compared with the pressure generated inside the membrane in order to determine the final room temperature equilibrium balloon height h^*_{RT}, i.e.,

$$P_{atm} + \frac{2e_0}{r\lambda^2_{\theta\theta}}(\sigma_{\theta\theta} - \sigma_0) = \frac{n_f R T_f}{V_f} \tag{6.15}$$

Design Tool

Assuming a fixed range of fuel masses—based on the deposited fuel mass distributions (see table 3.1)—initial chamber volume was varied in order to maintain a maximum membrane stretch $\lambda_{\theta\theta}$ below failure levels to prevent membrane rupture. The final chamber dimensions presented earlier in this chapter—i.e., $a = 2.5$ mm and $h_c = 750$ μm—were based on design calculations assuming propellant fuel masses between 100 and 200 μg for both the 10 % and 20 % binder mass fractions. The final design parameters are summarized in table 6.4.

Unfortunately, the second fuel deposition run yielded fuel masses several times larger than anticipated. This will cause much larger overpressures and potentially lead to membrane rupture. In the next section, we will present the final modeling results taking into account the actual fuel mass deposited on the devices. A sensitivity analysis will also be carried out to determine the relative importance of each design parameter.

Table 6.4: Summary of the balloon actuator design parameters.

		Value	
Parameter	Symbol	Min.	Max.
Fuel mass (μg)	m_{fuel}	100	200
Binder (%)		10	20
Membrane radius (mm)	a	2.5	2.5
Membrane thickness (μm)	e_0	90	90
Chamber height (μm)	h_c	750	750
Chamber volume (mm^3)	V_i	14.6	14.6
Balloon height (max inflation) (mm)	h^*_{max}	4.74	5.61
Balloon height (room temperature) (mm)	h^*_{RT}	3.15	4.35
Chamber pressure (max inflation) (bar)	ΔP	1.81	2.23
Membrane stretch	$\lambda_{\theta\theta}$	2.63	3.10
Rupture stretch	λ_{max}	3.45	3.45
Safety Margin		24 %	10 %

6.4.5 Modeling Results

In this section, the modeling results will be presented for the actual balloon actuators produced. The sensitivity of the model to the different input parameters and variables was calculated for the balloon at maximum inflation (table 6.5) and after the combustion gases cooled to room temperature (table 6.6). The output values given are the equilibrium balloon height h^*, the combustion chamber overpressure ΔP and the membrane stretch $\lambda_{\theta\theta}$. The input variables investigated are the fuel mass m_fuel, the initial combustion chamber volume V_i, unstretched membrane radius a, membrane thickness e_0 and the Yeoh model fitting parameters $C_i + \sigma_0$.

The top half of the table gives the baseline results for both the 10 % and 20 % binder fuel drops—with and without the parylene-C sealing layer. The baseline cases for each binder mass fraction used the modal values of the fuel mass distributions in table (3.1), while the maximum fuel mass values were the 75 % percentile values. The baseline value was also taken as the minimum value since the 25 % percentile values were larger than the modal values—due to the large skew in distributions. The bottom half of the tables describe the relative sensitive of each input variable.

The variable with the largest impact on the balloon height was the membrane radius. This is because the stress in the membrane scales with the membrane surface area, which is proportional to a^2. Increasing the initial membrane radius increases the equilibrium balloon height, while decreasing the membrane stretch and the chamber overpressure. The second most important factor affecting the balloon inflation was the initial fuel mass: increasing the fuel mass increased the balloon height, chamber overpressure and membrane stretch. Increasing the membrane thickness or Yeoh fitting coefficients—i.e., making the membrane stiffer—increased the chamber overpressure, while decreasing the balloon height and membrane

Table 6.5: Balloon actuator model sensitivity analysis (Maximum inflation).

Parameter	Value	h^*_{max} (mm)		ΔP (bar)		$\lambda_{\theta\theta}$	
10 % Binder							
Baseline m_{fuel} (μg)	312	6.38		2.76		3.52	
+ Parylene-C (nm)	68.2	6.49	(+1.7 %)	2.63	(−4.7 %)	3.59	(+2.0 %)
Max. m_{fuel} (μg)	435	6.87	(+7.7 %)	3.18	(+15.2 %)	3.80	(+8.0 %)
20 % Binder							
Baseline m_{fuel} (μg)	418	6.69		3.02		3.70	
+ Parylene-C (nm)	68.2	6.77	(+1.2 %)	2.87	(−5.0 %)	3.74	(+1.1 %)
Max. m_{fuel} (μg)	504	6.98	(+4.3 %)	3.28	(+8.6 %)	3.86	(+4.3 %)
(Compared to the 10 % binder baseline)							
m_{fuel}	+10 %		(+2.2 %)		(+4.0 %)		(+2.3 %)
	−10 %		(−2.4 %)		(−4.3 %)		(−2.3 %)
V_i (a const.)	See figure 6.17						
a (V_i const.)	+10 %		(+3.0 %)		(−15.2 %)		(−6.3 %)
	−10 %		(−4.0 %)		(+21.7 %)		(+6.8 %)
e_0	+10 %		(−1.3 %)		(+3.6 %)		(−1.1 %)
	−10 %		(+1.4 %)		(−4.0 %)		(+1.7 %)
$C_i + \sigma_0$	+10 %		(−1.3 %)		(+3.6 %)		(−1.1 %)
	−10 %		(+1.4 %)		(−4.0 %)		(+1.7 %)

stretch. Lastly, changing the initial chamber volume had a negligible effect

Table 6.6: Balloon actuator model sensitivity analysis (Room Temperature).

Parameter	Value	h^*_{RT} (mm)		ΔP (bar)		$\lambda_{\theta\theta}$	
10 % Binder							
Baseline m_{fuel} (μg)	312	5.09		1.96		2.82	
+ Parylene-C (nm)	68.2	5.22	(+2.6 %)	1.87	(−4.6 %)	2.89	(+2.5 %)
Max. m_{fuel} (μg)	435	5.62	(+10.4 %)	2.24	(+14.3 %)	3.10	(+9.9 %)
20 % Binder							
Baseline m_{fuel} (μg)	418	5.53		2.19		3.05	
+ Parylene-C (nm)	68.2	5.67	(+2.5 %)	3.08	(−5.0 %)	3.13	(+2.6 %)
Max. m_{fuel} (μg)	504	5.82	(+8.6 %)	2.36	(+11.7 %)	3.21	(+8.2 %)
(Compared to the 10 % binder baseline)							
m_{fuel}	+10 %		(+2.9 %)		(+3.6 %)		(+2.8 %)
	−10 %		(−3.3 %)		(−3.6 %)		(−3.2 %)
V_i (a const.)	See figure 6.17						
a (V_i const.)	+10 %		(+2.4 %)		(−11.2 %)		(−6.7 %)
	−10 %		(−3.5 %)		(+15.8 %)		(+6.7 %)
e_0	+10 %		(−1.6 %)		(+3.1 %)		(−1.4 %)
	−10 %		(+1.6 %)		(−3.1 %)		(+1.4 %)
$C_i + \sigma_0$	+10 %		(−1.6 %)		(+3.1 %)		(−1.4 %)
	−10 %		(+1.6 %)		(−3.1 %)		(+1.4 %)

Lastly, the effect of initial chamber volume on the balloon height was modeled for the 10 % binder modal fuel mass (see figure 6.17). Assuming the amount of gas generated by the combustion was constant—i.e., the initial adiabatic constant $P_i V_i^{\gamma}$ remains unchanged—one would expect the balloon height to drop as the combustion chamber volume increases, since we are adding a fixed amount of gas into a larger initial volume (the red line in figure 6.29). However, amount of gas generated by the combustion process was not fixed, but increased with decreasing temperature (see figure 6.18). This is because the equilibrium constants of the various combustion products change with temperature. As such, the balloon height was found to increase initially with increasing chamber volume, before slowly decreasing.

Effect of Gas Leakage

Although PDMS is known to be permeable to gases over time scales on the order of several hours [60], it is not clear how important this effect is on the performance of pyroMEMS balloon actuators. PDMS leak tests are usually conducted under steady conditions with small pressure differences—e.g., 20 kPa—and at room temperature. No in-depth studies of gas leakage in pyroMEMS balloon actuators has been carried out to date.

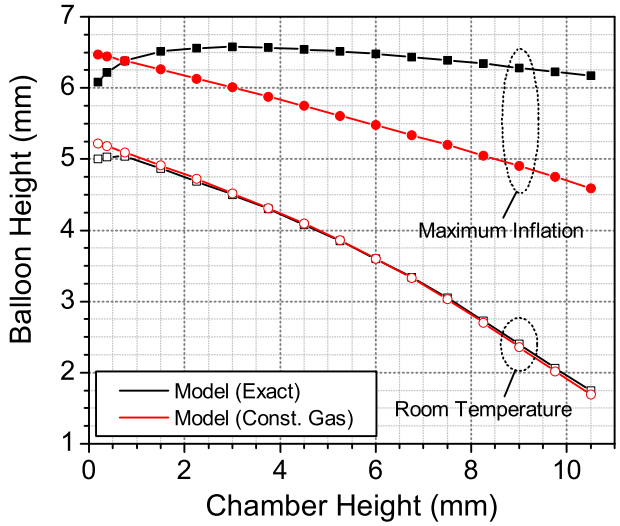

Figure 6.17: Maximum balloon height vs. initial chamber height (model, 10 % binder, $m_{fuel} = 312$ μg, $a = 2.5$ mm, PDMS without parylene-C). The red points represent the model predictions assuming a fixed adiabatic constant $P_i V_i^{\gamma}$, while the black points are the model results without approximation. The solid symbols are the results at maximum inflation and the open symbols are when the combustion products have cooled to room temperature.

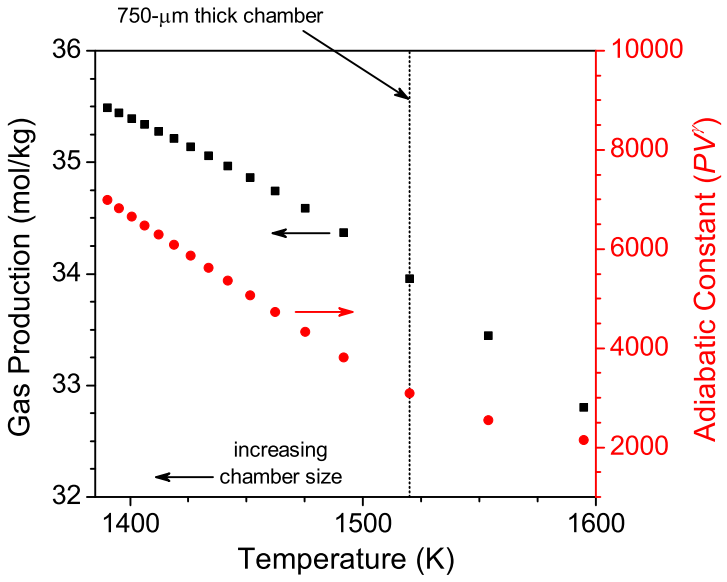

Figure 6.18: Effect of combustion temperature on the number of moles of gas generated by the combustion per unit mass of fuel and the adiabatic constant (10 % binder). The dotted line shows the baseline conditions ($a = 2.5$ mm, $h_c = 750$ μm).

In order to get a rough estimate of the contribution of gas leakage across the PDMS membrane, a simple gas permeability model used based on the permeability silicone rubber at room temperature [63]. The volume of gas ΔV lost across a membrane of thickness δ and surface area A under an applied pressure ΔP during a time t is given as

$$\Delta V = \frac{pAt\Delta P}{\delta} \tag{6.16}$$

where p is the permeability of the membrane. Since ~ 50 % of the gaseous combustion products are CO, the permeability of CO was used. Assuming a constant internal pressure equal to the pressure at maximum membrane displacement (10 % binder, baseline), we obtain a volume lost of ~ 10 mm^3 over 1 second—the duration of the measurements—which represents only 10 % of the volume of the inflated membrane at maximum height. In comparison, the volume decrease due to the cooling of the combustion products down to room temperature was over 37 %—almost 4× higher. As such the gas leakage is important, but it is not the primary cause of balloon deflation. Note: this calculation represents only a rough estimate as the permeability values used were measured at a pressure difference of 20 psi (1.36 bar), were not for Sylgard 186 and not for the gas mixture found in the K-DNBF combustion products.

6.5 Results

First, the ignition and combustion behavior of the nickel-plated igniters will be presented—without chambers or membranes attached. Then the balloon inflation results will be presented. The effects of binder content, parylene-C sealing layer and chamber height were investigated.

6.5.1 Experimental Setup

The same experimental setup as in chapters 4 and 5 was used for the ignition and combustion experiments. For the inflation tests, the balloon actuation was captured from the side using the high-speed framing camera with a TV lens (Computar TV lens, 75 mm diameter, F1.4). The frame rate was set to 21,000 frames per second (47.57 μs frame intervals). The image scaling was established by placing a ruler in the frame behind the balloon. Instead of wire-bonding the devices, the electrical connects were made with probe needles (see figure 6.19).

A 1.5-second, square voltage pulse was applied to the igniters as before. Voltages between 2 and 3 V were used—i.e., input power levels between 0.7 – 1.3 W.

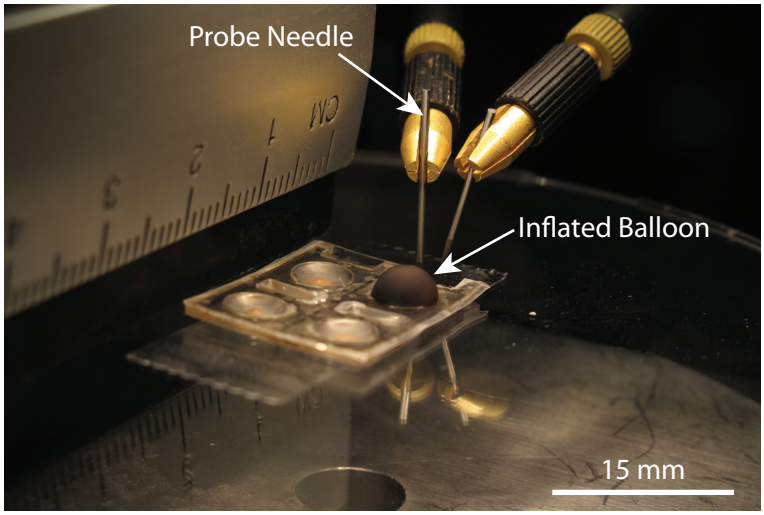

Figure 6.19: Picture of the experimental setup for pyroMEMS balloon actuator tests. A 2 × 2 array of balloon actuators is visible in the center of the frame, with the top right actuator already inflated. The ruler to the left of the frame was used to scale the images taken with the high-speed camera (not shown)

6.5.2 Fuel Ignition and Combustion

Initial fuel ignition and combustion tests were carried out using the nickel-plated inkjet-printed igniters without the epoxy chambers or PDMS membranes—in order to gain optical access to the combustion event.

Ignition Behavior

Ignition and complete combustion of both the 10 % and 20 % binder mass fraction fuel drops was successfully achieved with the nickel-plated igniters. Succeeded for voltages ≥ 2.5 V (≥ 0.9 W), but failed for input voltages of 2 V (~ 0.6 W). A typical ignition power curve is shown in figure 6.20. The ignition of the fuel is clearly visible at 0.694 s as a sudden drop in power—i.e., increase in temperature—in the igniter. The behavior of the nickel-plated, inkjet-printed igniters was ohmic, with a smooth increase in dissipated power with temperature. The small fluctuations in the power curve were due to line noise at 50 Hz.

Combustion Behavior

Although ignition was successfully achieved with both binder mass fractions, only the 20 % binder fuel drops exhibited smooth combustion (see figure 6.21), whereas the 10 % binder drops suffered from fuel peeling and ejection. In general, the igniters were not adversely effected by the combustion of the fuel drops: figure 6.21d clearly shows the igniter still operational and incandescent until the end of the voltage pulse. In about 25 % of cases (8/31), the heat dissipated by the igniter/combustion punctured holes in the PET substrate and ruptured

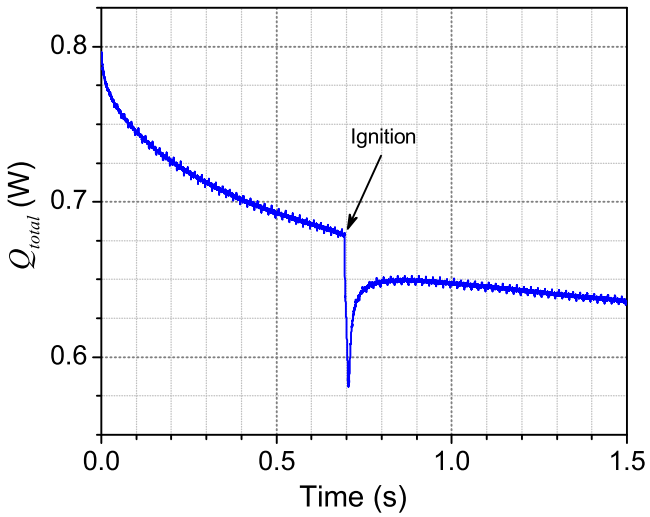

Figure 6.20: Input power vs. time curve for the pyroMEMS balloon actuators (Nickel-plated igniter, 2.5 V, 20 % binder). The ignition point is clearly visible at 0.694 s.

the igniter (as in figure 6.10); however, most of the time, both survived intact (see figure 6.22). A further three igniters were on the verge of failing—their resistances had increased substantially. The mean increase in resistance due to the combustion event was statistically negligable—$0.10 \pm 0.15\ \Omega$—not counting the failed igniters.

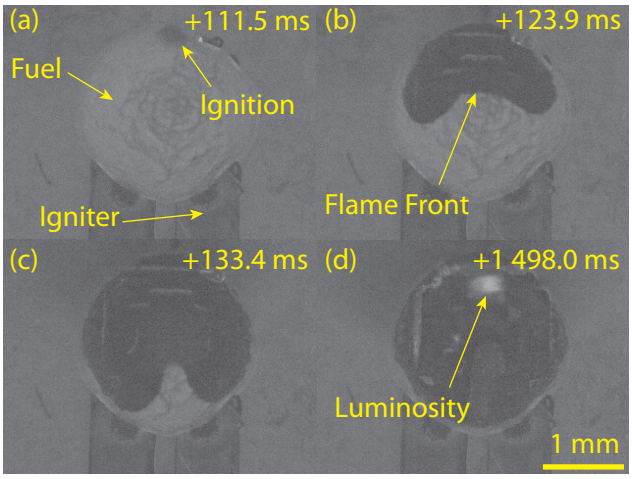

Figure 6.21: High-speed video frames of a "successful" combustion event (Nickel-plated igniter, Q_{total} = 1 W, 20 % binder): (a) at ignition, (b) and (c) smooth combustion; (d) at the end of the voltage pulse.

Increasing the substrate thickness as well as changing to polyethylene naphthalate (PEN) substrates with a higher glass transition temperature will be considered in the future. Polyimide (PI) was also tested—the same as that used in chapter 4—but exhibited poor adhesion to the

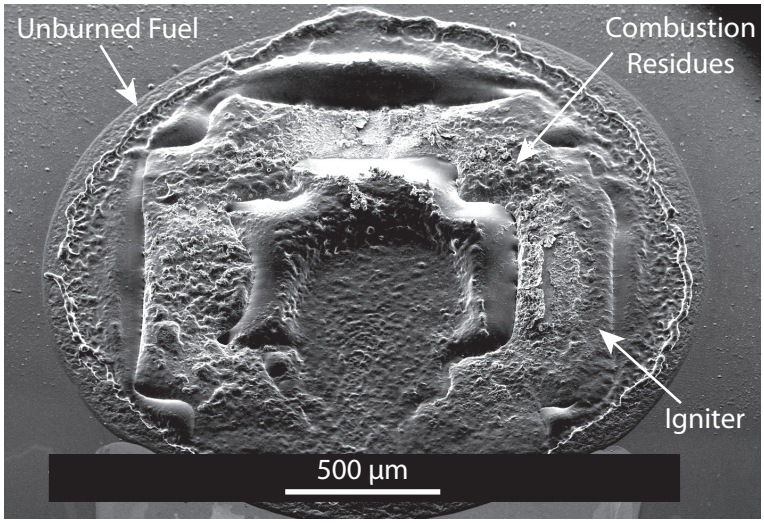

Figure 6.22: SEM of nickel-plated igniter after fuel combustion. Note: no visible holes in PET foil.

epoxy chambers.

6.5.3 Balloon Inflation

Of the 29 balloon actuators successfully fabricated, 11 were successfully inflated, 6 membranes were punctured and leaked relatively slowly (figure 6.24), 8 membranes bursted violently (figure 6.25) and 4 failed to ignite. In the following sections, we will break down these 29 inflation results and investigate the adhesion between the various layers as well as the effect of binder content, parylene-C coating layer and initial chamber volume on the pyroMEMS balloon inflation were investigated.

Balloon Dynamics

The pyroMEMS balloon actuators were successfully inflated (see figure 6.23). The membrane inflation began suddenly as the pressure waves generated by the fuel combustion impacted the membrane. This caused the center of the membrane to overshoot its equilibrium position and oscillate—as illustrated in figure 6.23a and b. These oscillations were highly damped and decayed after only one period of oscillation. Afterwards the initial oscillations decayed, the membrane inflated smoothly, reaching maximum height in 2.33 ms. The height of the balloon increased approximately exponentially before stabilizing at its peak height of 6.58 ± 0.33 mm (see the black data points in figure 6.27). This represents an average membrane inflation speed of 2.8 m/s—and a maximum initial speed of 21.6 m/s (or ~ 80 km/h). Then, the balloon deflated exponentially. The balloons remained partially inflated for a few hours after actuated—as in figure 6.19. The uncertainty in the experimental values stem from the uncertainty in the image scaling.

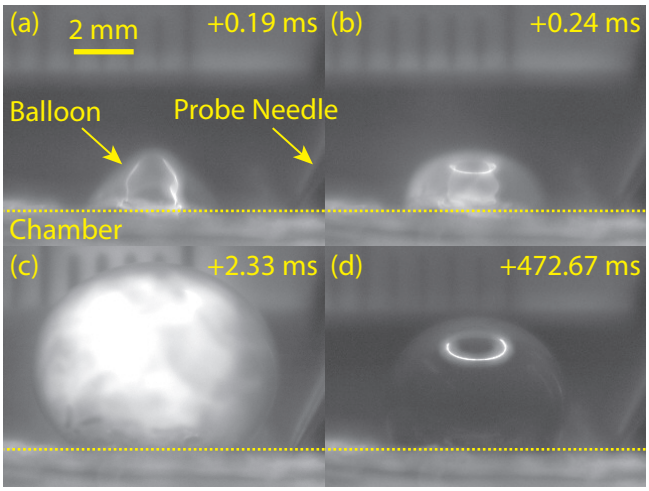

Figure 6.23: High-speed video frames of a successful balloon actuation (Parylene-C coated PDMS membrane, a = 2.5 mm, h_c = 750 μm, Q_{total} = 845 mW, 10 % binder): (a) and (b) show the highly unsteady early stages of the membrane inflation, (c) shows the membrane at maximum height and (d) shows the deflated membrane long after combustion has ended. A time stamp is given in the top right corner of each frame. The incandescent combustion products are clearly visible through the membrane in frame (c).

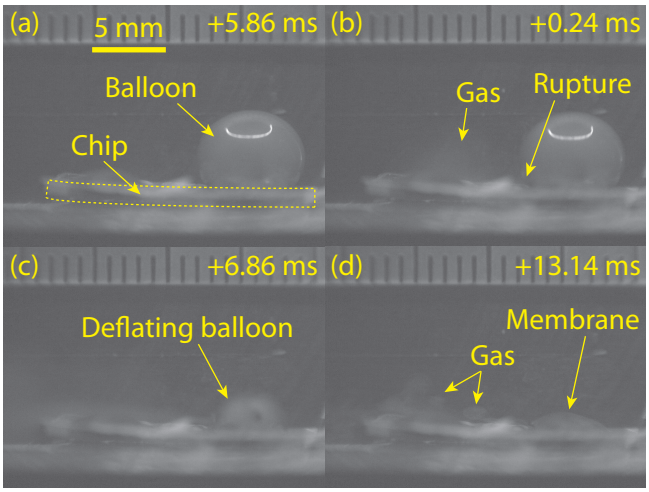

Figure 6.24: High-speed video frames of a failed balloon actuation due to gas leaking (Parylene-C coated PDMS membrane, a = 2.5 mm, h_c = 750 μm, Q_{total} = 914 mW, 20 % binder): (a) balloon before onset of leaking, (b) membrane ruptures and gas begins to leak, (c) balloon rapidly deflates (appears blurry in frame) and (d) membrane completely deflated, but plastically deformed—puffs of gas indicated. A time stamp is given in the top right corner of each frame.

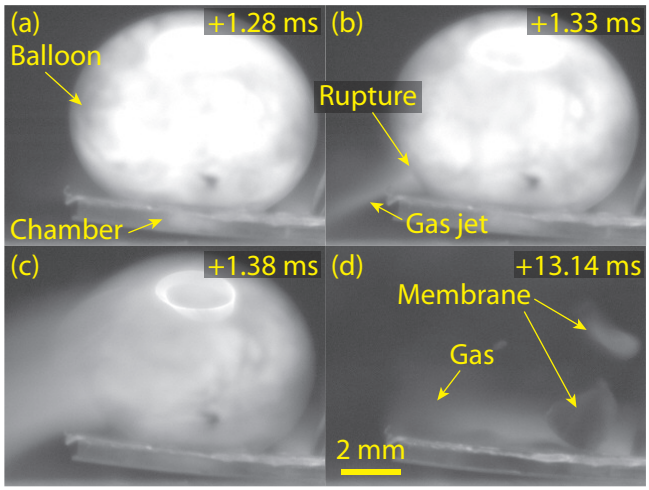

Figure 6.25: High-speed video frames of a failed balloon actuation due to sudden membrane bursting (Parylene-C coated PDMS membrane, $a = 2.5$ mm, $h_c = 750$ μm, $Q_{total} = 899$ mW, 10 % binder): (a) 1 frame before bursting, (b) membrane ruptures and a gas jet is visible, (c) tear propagates and gas escapes balloon and (d) membrane flies apart in pieces. A time stamp is given in the top right corner of each frame.

Layer Adhesion

The bonding between the PDMS and the epoxy chamber was good: no delamination of the PDMS membranes was observed in any of the high-speed videos. The adhesion strength between the PET substrate and epoxy chambers was also investigated qualitatively. When the PET substrate was separated from the epoxy chambers, the soot generated from the combustion left an imprint on the igniter substrate (see figure 6.26). The edges of the soot imprint were sharp, indicating no visible delamination occurred at the PET/epoxy interface. However, no quantitative measurements of layer adhesion have been carried out to date.

Effect of Binder

The balloon dynamics for both the 10 % and 20 % binder mass fraction fuel drops are shown in figure 6.27. The 10 % binder devices inflated faster (2.331 s vs. 9.942 s) and to a greater extent (6.58 mm vs. 5.03 mm) than the 20 % binder chips—and this despite the larger fuel mass of the 20 % binder drops (418 μg vs. 312 μg). The semi-analytical model predicted balloon heights of between 6.49 mm and 6.96 mm for the 10 % binder drops and between 6.77 mm and 7.06 mm for the 20 % binder devices (750 μm chamber height, parylene-C coated membranes). For equal masses of fuel, the ICT code predicted ~ 2 % higher post-combustion pressures for the 10 % binder mixture.

The reason for the unusually low balloon heights associated with the 20 % binder are unknown; however, from the high-speed videos do offer a clue. As shown in figure 6.28, one can see that the 10 % binder mass fraction fuel mixtures resulted in incandescent combustion products that

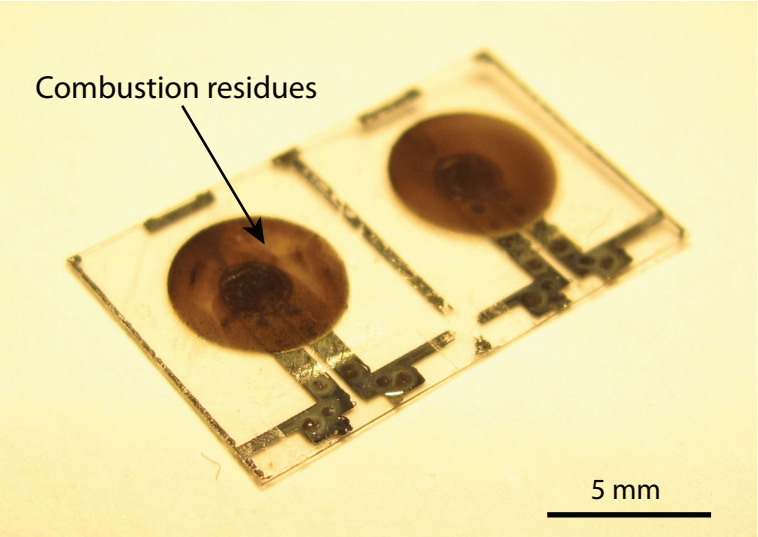

Figure 6.26: The PET substrate after fuel combustion (epoxy layer removed). The combustion residues (soot) left a sharp imprint on the substrate, indicating good PET/epoxy adhesion with little delamination.

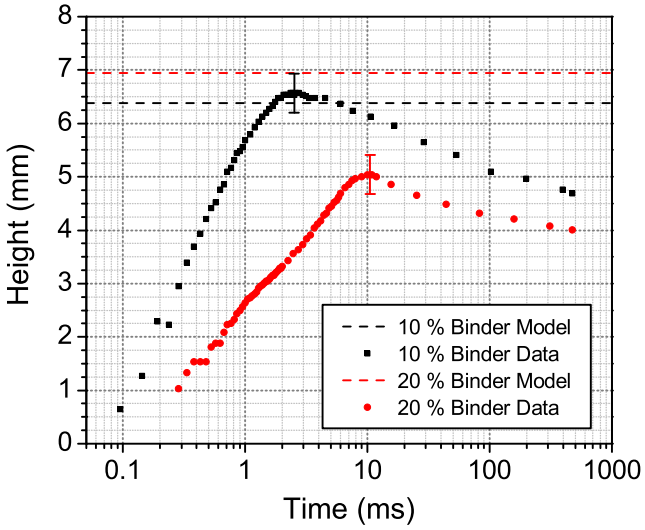

Figure 6.27: Balloon height vs. time for both the 10 % and 20 % binder fuel mixtures (Parylene-C coated PDMS membrane, $a = 2.5$ mm, $h_c = 750$ μm).

were clearly visible through the thin membranes, while the 20 % binder drops did not generate any substantial light emission. This lack of incandescence is a sign that the combustion temperatures were substantially lower.

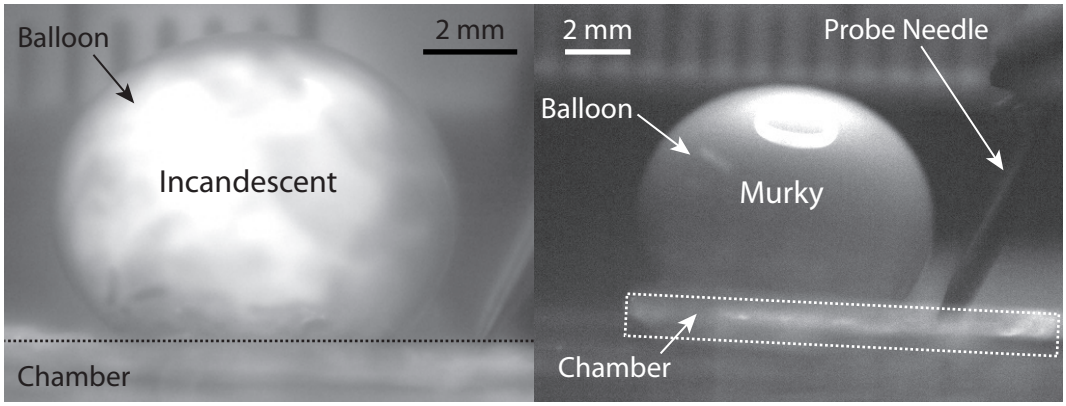

Figure 6.28: High-speed video frames at maximum balloon stretch for (a) 10 % and (b) 20 % binder fuel mixtures. The 10 % binder combustion products were highly incandescent, while the 20 % binder products were not.

Effect of Parylene-C Capping Layer

PDMS membranes are known to be permeable to gas; therefore we evaporated a thin 100 nm-thick (nominal) parylene-C sealing layer onto some of the balloon membranes in order to determine its effectiveness in preventing gas leakage [60]. For 20 % binder mass fraction, no statistically significant change in the balloon height was observed (5.03 ± 0.2 mm vs. 5.10 ± 0.33 mm, for the coated and uncoated membranes, respectively). Furthermore, the parlene-C coated membranes deflated at the same rate as the uncoated devices. A more in-depth investigation—using more devices and different thicknesses of parylene-C—is needed to better understand the importance of gas leakage in pyroMEMS balloon actuators.

Effect of Initial Chamber Volume

Lastly, a series of pyroMEMS balloon actuators were inflated with different chamber volumes—from 1 to 3 epoxy layers thick—but with the same unstretched membrane radius a. The balloon height was found to increase with increasing chamber volume, as predicted by the model—although the magnitude of the increase was inaccurate.

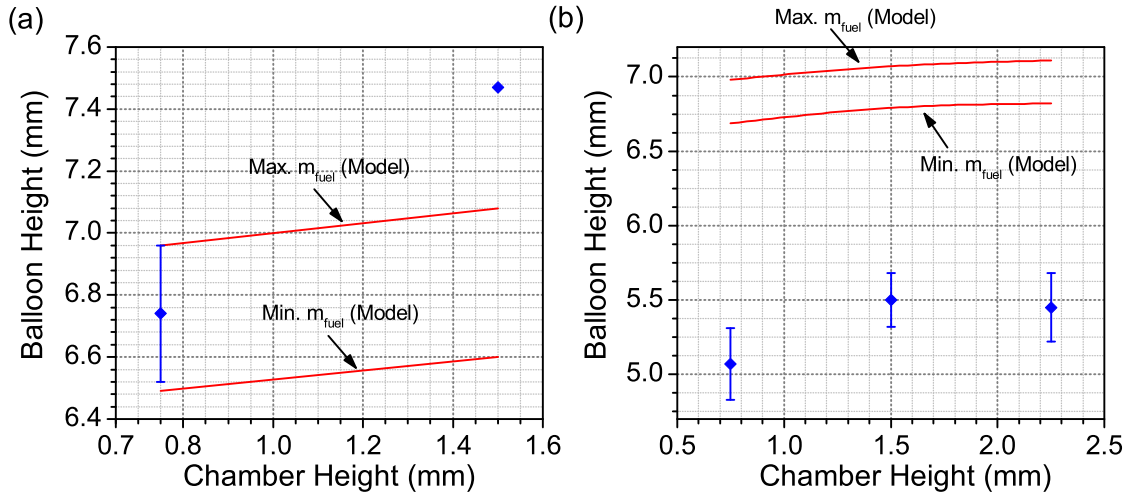

Figure 6.29: Maximum balloon height vs. initial chamber height: (a) parylene-C coated PDMS membrane, $a = 2.5$ mm, 10 % binder, and (b) PDMS membrane, , $a = 2.5$ mm, 20 % binder. The red lines represent the model predictions over the range of fuel masses and the experimental data is given as the blue diamonds.

6.6 Discussion

6.6.1 Igniters

The nickel-plated inkjet-printed igniters exhibited excellent properties: their fabrication was reliable—yielding a relatively tight distribution of resistances—and they were able to dissipate 2 W of power for nearly 200 s, reaching over 265 °C. Their failure was linked to igniter rupture due to melting of the underlying PET substrate—rather than electromigration. This can be mitigated by using a more heat-resistant substrate such as polyethylene naphthalate (PEN) or polyimide (PI).

The large width of the igniter lines (~ 200 μm) resulted in higher minimum ignition powers—~ 900 mW vs. ~ 350 mW for the bottom-side igniters patterned on polyimide, see table 4.13. It also led to fuel peeling for the 10 % binder fuel drops. It should be noted that the inkjet-printed igniters were designed with a relatively large margin of safety in terms of feature size and current density. In fact, straight inkjet-printed lines as thin as 50 μm can be readily be made. Reducing the line width should decrease the input powers required for ignition as well as diminish the occurrence of fuel peeling.

6.6.2 Epoxy Chambers

Fabricating the combustion chambers using the SUEX™ photodefinable epoxy dry film sheets greatly simplified the fabrication of the pyroMEMS devices compared to using standard silicon microfabrication. With the SUEX™ dry film, all of the steps associated with deep reactive ion

etching are replaced by a simple photolithography step and a 150 minute development step using the standard SU-8 developer (PGMEA). Furthermore, the epoxy chambers readily adhere to many substrate materials—including silicon, glass, PET and PDMS—greatly simplifying the layer assembly. The adhesion was able to withstand the high pressures (~ 1-2 bar overpressure) developed inside the combustion chambers without any visible traces of delamination.

6.6.3 PDMS Membranes

We found that coating the PDMS membranes with parylene-C did not have an appreciable effect on the maximum balloon height or deflation rate of the pyroMEMS balloon actuators. The parylene-C thickness used in this work—68.2 nm (0.35 g dimer)—was much less than used by Sawano et al. [60]. Their exact parylene-C thickness was not given, but the mass of dimer used was between 1 and 4 g. The final thickness is proportional to dimer mass, but also depends on the size of the evaporation chamber used to deposit the parylene-C—which is unknown. Since excess parylene-C greatly stiffens the PDMS membranes, we chose parylene-C dimer masses smaller than Sawano. More work needs to be done to:

1. quantify the gas leakage through the PDMS membranes;
2. optimize the parylene-C thickness if it is found to be useful in preventing gas permeation for these pyroMEMS balloon actuators.

6.6.4 Inflation Results

A summary of the pyroMEMS balloon inflation results is given in table 6.7. Due to the unexpectedly large amount of propellant deposited on the pyroMEMS balloon actuators, more than half of the balloons ruptured due to excess internal pressure. The 10 % binder results were in relative good agreement with the model simulations, whereas the 20 % binder results were overpredicted by ~ 20 %. Increasing the chamber height increased the balloon displacements, as predicted by the model. Finally, the parylene-C sealing layer had a negligible effect of the balloon height and deflation rate. These results represent a first validation of the fabrication process and predictive model—more tests are needed to truly validate the model. In particular, testing balloon actuators with different membrane radii—the most sensitive design parameter—will provide a true test of the model's validity.

Only one other pyroMEMS balloon actuator study has been published in the literature by the group at the CNRS-LAAS [23, 64]. A comparison between their devices and those presented here is given in table 6.8. Their balloon actuators were much smaller than ours: they consisted of 30-μm thick, square PDMS membranes measuring 500 μm×500 μm. This represents a length-over-thickness ratio of ~ 17 compared to ~ 54 for our membranes—making their membranes stiffer. Their devices burned ~ 90 ng of a hetero-metallic (Mn-Co) Werner complex—normally used as a gas generator in airbags—in a chamber volume of 0.025 mm^3—compared to ~ 300 – 400 μg of fuel in 14.7 mm^3 chambers for our devices. This resulted in

Table 6.7: Summary of balloon inflation results.

Binder (%)	Chamber Height (μm)	Parylene-C	Success Rate	Balloon Height (mm)
10	750	yes	3/8 (37.5 %)	6.74 ± 0.22
	1500	yes	1/4 (25 %)	7.47
20	750	yes	1/9 (11.1 %)	5.03
	750	no	2/4 (50 %)	5.10 ± 0.33
	1500	no	2/2 (100 %)	5.50 ± 0.18
	2250	no	2/2 (100 %)	5.45 ± 0.23

smaller fuel loading densities—3.6 mg/cm^3 vs. $\sim 7-27$ mg/cm^3. As a result, they obtained much smaller balloon heights—with respect to the unstretched membrane length—of 0.092 vs. 1.5 for our devices. However, the CNRS-LAAS measured their balloon heights after the balloons stabilized at room temperature, while our balloon heights were taken at maximum displacement. One of the great advantages of their fuel was that it generated only benign gases—H_2O, N_2 and O_2. Lastly, both studies obtained success rates at or near 50 %, indicating that the fabrication processes for these types of devices are far from optimized. Most of our failures (14/18) were due to membrane rupture brought about by too much fuel deposited on the devices—only 4 out of a total of 29 failed to ignite for unknown reasons. The devices were originally designed for fuel masses on the order of $100-200$ μg as obtained in the first fuel deposition run (see table 4.2).

Table 6.8: PyroMEMS balloon actuators: comparison with the literature.

Parameter	This work	CNRS-LAAS [23]
Fuel		
Type	K-DNBF	(Mn-Co) Werner complex
Mass (μg)	$\sim 300-400$	0.09
Loading density (mg/cm^3)	$7-27$	3.6
Chamber		
Volume (mm^3)	$14.7-44.2$	0.025
Membrane		
Material	Sylgard® 186	Sylgard® 184
Shape	Circular	Square
Length (mm)	5	0.5
Thickness (μm)	92.7 ± 9.8	30
Length/Thickness	54	17
Displacement		
Max. balloon height (mm)	6.74	0.046 (Room temperature)
Balloon height (mm) [model]	$6.49-6.96$	$53-71$
Height/Length	1.5	0.092
Success Rate	38 % (11/29)	50 %

6.6.5 Balloon Actuator Model

The goal of the balloon actuator model was twofold: (1) to properly size the devices to avoid membrane rupture during actuation and (2) to predict the maximum size of the inflated balloon. The model was relatively successful (11 out of 25), primarily because the mass of the deposited fuel drops were 300 % larger than anticipated (~ 300 μg vs. 100 μg). As for the maximum balloon height, the initial experiments are promising: the maximum height of the 10 % binder devices was in relatively good agreement with the model (at most ~ 5.5 % error), although the 20 % binder results were overpredicted by ~ 20 %. The reason for the small balloon heights is unclear at this time, but the lack of visible incandescent combustion products may indicate substantially lower combustion temperatures and perhaps incomplete combustion—which is not captured in the model.

Only one other pyroMEMS balloon actuator model has been published in the literature by the group at the CNRS-LAAS [23, 64, 65]. The CNRS team developed a finite element model that simulated the igniter heating, propellant ignition and combustion as well as the membrane deflection all together. As such, they did not need to make as many simplifying as for the semi-analytical model presented in this work. They obtained a discrepency of between 13 – 35 % between the model and the experiment.

A key difference between our model and the one developed by the CNRS-LAAS was that we predicted the maximum balloon inflation—before the combustion products have cooled down—as well as the equilibrium—room temperature—deflection level. This is important, because the actual performance of the actuator depends on the force generated by the membrane at maximum displacement, not when the products have cooled down to room temperature.

Lastly, one of the major drawbacks of the model was that the ICT code and the MATLAB algorithm were not integrated together, making design iterations time consuming. Ultimately, the MATLAB code should be able to automatically run the chemical solver and retrieve the outputs in an automated fashion.

6.7 Conclusion

By leveraging low-cost, additive fabrication techniques, we successfully demonstrated large deformation pyroMEMS balloon actuators on plastic foil. This technology demonstrator was made possible through the combination of cleanroom-free (compatible) processing and reliable, drop-coated annular igniter geometries.

The next step in developing reliable pyroMEMS balloon actuators for fluid pumping and ejection is to measure the force generated by the balloon actuator against a range of back pressures. Furthermore, the balloon actuator model needs to be validated for different membrane diameters and membrane thicknesses to ensure that the model is robust. Lastly, direct combustion chamber temperature measurements—using the micro-thermocouples—would

put to rest once and for all the importance of gas cooling in the membrane deflation.

7 Conclusion

7.1 Summary

In this work, we have presented modeling and fabrication techniques to improve pyroMEMS reliability and performance. First, the fuel was carefully chosen based on its relatively low ignition temperature, large volume of gas generated and relative stability. It was specially modified to yield micrometric grain sizes for deposition via a drop coating dispenser. The combustion behavior was simulated using a chemical equilibrium solver (ICT code) and the results were validated experimentally by measuring the *in situ* pressure and temperature inside a pyroMEMS device. We recorded combustion temperatures of 1300 ± 160 °C and combustion overpressures of 49 ± 16 bar. These results were in good agreement with the values obtained from the ICT code. This represents the first such measurements ever carried out in pyroMEMS devices. The ICT code was used to construct a complete model of a pyroMEMS balloon actuator.

Two complementary pyroMEMS igniters were developed in this thesis: a drop-coated bottom-side igniter and a top-side shadow-mask evaporated igniter. The bottom-side igniter concept was based on the localized, peripheral heating and ignition of fuel droplets—using narrow line segments, or "hot spots"—to obtain smooth, steady combustion without fuel peeling or ejection. Fuel peeling was further mitigated by adding additional binder to the fuel mixture to improve its surface adhesion and decrease its burning rate. The overall fabrication process was highly simplified and extremely robust—over 350 igniters were successfully fabricated and tested. An in-depth investigation of igniter performance based on substrate material, igniter layout, fuel binder content and input power was performed. Simple, semi-analytical thermal ignition models were developed and successfully predicted the ignition delay times of all the igniter geometries. These bottom-side igniters can be used in pyroMEMS devices where reliability and cost are key concerns, such as automated fluid actuators for drug injection or safe, arm and fire devices for military ordinance.

For applications where high fuel loading densities are required for performance specifications—such as micro-thrusters—a simplified fabrication concept for a top-side igniter was developed.

The existing pyroMEMS thrusters—based on membrane suspended igniters—suffered from poor ignition reliability due to delamination or premature rupture of the membranes. The igniter concept was based on the direct deposition of a metal igniter on the fuel surface via offset shadow mask evaporation—thereby avoiding the membranes all together. Metal igniters were deposited on the fuel surface without fuel degradation or ignition. The ignition concept was successfully demonstrated on fuel drops and over top full fuel chambers. The main cause of igniter failure was the non-conformal coverage of the sharp chamber wall edges leading to discontinuous metal lines.

Lastly, pyroMEMS balloon actuators for use in automated drug delivery systems and microfluidic actuators was designed, fabricated and tested. We made use of low-cost polymer materials and additive fabrication techniques to construct the devices. The igniters were fabricated on PET foils by inkjet printing and nickel electroplating. The combustion chambers were made using a photodefinable thick epoxy dry film material that readily adheres to a wide variety of substrates. Arrays of devices were fabricated at the foil-level and assembled together via lamination—no chip-scale manual post-processing was required. The goal was to develop a robust fabrication process that was compatible with microfluidic devices and avoided manual, chip-scale processes. Using the epoxy for the combustion chambers greatly simplified the assembly of the devices: rather than adding an additional adhesive layer, the chambers themselves were bonded to the other foils by applying heat and pressure.

The resulting balloon actuators generated large out-of-plane displacement of up to 7.47 mm (for a membrane diameter of 5 mm). The balloon dynamics were recorded using a high-speed framing camera—the balloons were found to inflate in little over 2 ms. The fabrication yield was very good, with 25/29 balloon actuators successfully ignited; the balloon inflation success rate was rather poor (11/29) due to membrane rupture caused by the excessive amount of fuel deposited in the devices. The effect of binder content, initial chamber volume and parylene-C sealing layer on the balloon height were investigated. A model of the pyroMEMS balloon inflation was developed combining the ICT chemical equilibrium code—to calculate the thermodynamic state of the combustion products—and a hyperelastic material model to determine the resulting membrane displacement. A sensitivity analysis of the different device parameters found that the membrane radius was the most important parameter in determining the balloon height. The model was used to both design the geometry of the balloon actuator and benchmark the experimental measurements. The good agreement between the model and experiments was obtained—except for the 20 % binder fuel mixtures. The maximum discrepency between the model and the results was ~ 20 %, which is similar to the other pyroMEMS model in the literature.

7.2 Main Contributions

The first main contribution of this work was to quantify—for the first time—the ignition and combustion reliability of a pyroMEMS igniters. This is particularly important for single-use

devices—such as pyroMEMS—that require large numbers of analogous devices in order to properly characterize their performance. At this time, the biggest hurdle to the development of pyroMEMS devices is their complex—and often artisanal—fabrication processing. This variability introduced in the fabrication is carried over to the device's performance. Furthermore, large numbers of devices are difficult, if not impossible to produce, preventing accurate predictive models from being developed. The only way to overcome this stagnation is to focus on simple, robust fabrication methods with little to no chip-scale, manual processing. This challenge was addresses in three complementary ways:

1. The exhaustive study of bottom-side igniter ignition and combustion behavior using simple analytical models to understand the effect of the different design parameters.

2. The shadow mask evaporated top-side igniters allow the solid propellant fuel to be more deeply integrated into the pyroMEMS fabrication process—rather than relegated to the back-end processing. This improves the intimate contact between the fuel and the igniter and opens up more—hopefully more robust—device architectures.

3. A pyroMEMS fabrication process that is cleanroom-free (compatible) was demonstrated to make arrays of balloon actuators. As opposed to trying to integrate the fuel into the cleanroom, in this process, the microfabrication was taken outside the cleanroom by leveraging polymer materials, additive processing and foil-level lamination techniques. The critical fabrication step that makes this technique useful was the robust, low-temperature lamination of the device stack. This was made possible by fabricating the chambers using photodefinable epoxy dry sheets, which readily form strong bonds to a number of different substrates—including silicon, glass, PET and PDMS.

The second main contribution of this thesis was the development of experimentally-validated pyroMEMS models. Analytical models were preferred over numerical models because they not only predict the performance the system at a particular point or set of points, but explain the underlying processes involved and point the way towards potential improvements. However, the drawback of analytical models is that they generally require more restrictive assumptions in order to model the system and therefore may not be as accurate as a numerical model. Two different analytical models were developed in this work: thermal models to predict the ignition behavior of the various bottom-side igniter layouts presented in chapter 4 and a thermo-mechanical model of the pyroMEMS balloon actuator inflation developed in chapter 6. Both models produced results that were in relatively good agreement with the experimental results.

7.3 Future Work

Now that relatively robust pyroMEMS fabrication methods have been demonstrated, the next step is to optimize the propellant deposition parameters.

Furthermore, there is an urgent need to carry out more experimental validation of the pyroMEMS models. More temperature and pressure measurements are needed for a wide variety of chamber volumes to push the limits of the ICT thermodynamic code. In addition, property measurements with different chamber materials can be envisioned to quantify the effect of thermal losses to the environment.

Lastly, the relative importance of gas leakage versus membrane deflation due to heat losses in pyroMEMS balloon actuators needs to be put to rest once and for all. By integrating the microthermocouples presented in chapter 3 into the balloon actuator combustion chambers, the combustion products temperature can be monitored in real time to quantify the contribution of gas cooling to the membrane deflation.

A ICT Thermodynamics code: sample output

The following output is for a 312 μg K-DNBF fuel mass with 10 % binder (modeled as acetylcellulose) in a 14.7 mm^3 volume chamber (the parameters used in chapter 6 for the pyroMEMS balloon actuators). Note: a ratio of 80/20 fuel to binder is used for the 10 % binder mass fraction fuel mixture because the original 10 % binder mixture contains 50 % water—which evaporates during curing. Therefore, the final mixture ratio is 40/10 fuel to binder.

```
COMPOSITION                                ENTHALPY OF FORM.

WEIGHT% NAME                                     (KJ/MOLE)

 80.000 KDNBF                                S   -653.96
 20.000 ACETYLCELLULOSE                      S  -1560.63
                      OXYGEN BALANCE:   -58.39 %
HEAT OF FORMATION:  -2936.66 KJ/KG =   -701.88 KCAL/KG
SUM FORMULA (for one kg):      DENSITY:  1.941 G/CC
             C = 25.3348
             O = 25.3942
             N = 11.3391
             H = 19.6058
             K =  2.8348

Iteration of temperature started at  1524. K

PRESSURE:             90.85 BAR        TEMPERATURE:      1466.2 K
VOLUME:             4719.9 CC          LOADING DENSITY:  .02119 G/CC
MOLES PER KG:       39.831 (total)     34.452 (gases)     5.379 (cond.)
MMW GASES:          22.035 G/MOLE      MMW CONDENSED:    44.779 G/MOLE
MMW (100./GMZ):     25.106 G/MOLE      MEAN SPEC. HEAT:  1172.9 J/(KG)(K)
```

```
SPEC.HEAT Cp:        1627.4 J/(KG)(K)          40.858 J/(MOLE R.PROD.*K)
SPEC.HEAT Cp:        36.019 J/(MOLE GASES*K)
SPEC.HEAT Cv:        27.658 J/(MOLE GASES*K)   1255.2 J/(KG OF GASES)(K)

B(T):                 28.23 CC/MOLE    C(T):    595.1 CC**2/MOLE**2

ENTHALPY:           -2508.1 J/G        INTERNAL ENERGY:    -2936.9 J/G
ENTROPY:              7.798 J/(G)(K)
KAPPA(=Cp/Cv):       1.3023            GAMMA:                1.3294
KAPPA(GASES+COND.):  1.2285            GAMMA(GASES+COND.):   1.2540
C*:                   971. M/SEC       VELOCITY OF SOUND:    755.0 M/SEC
SPECIFIC ENERGY:      420.0 J/G        COVOLUME:              .967 CC/G

REACTION PRODUCTS:  NAME           MOLE NUMBER   MOLE%    WGT.%

                    C          G   1.69960E-18    .000     .000
                    O          G   1.25392E-13    .000     .000
                    N          G   3.65764E-14    .000     .000
                    H          G   2.00714E-05    .000     .000
                    K          G   5.24693E-03    .013     .021
                    CO2        G   8.47182E-01   2.127    3.728
                    H2O        G   8.93174E-01   2.242    1.609
                    N2         G   5.65135E+00  14.188   15.831
                    CO         G   1.86008E+01  46.699   52.101
                    H2         G   7.92087E+00  19.886    1.597
                    OH         G   5.79074E-08    .000     .000
                    NO         G   5.29406E-10    .000     .000
                    O2         G   6.48509E-15    .000     .000
                    NH3        G   1.00470E-02    .025     .017
                    CH4        G   4.81324E-01   1.208     .772
                    HCN        G   5.66046E-03    .014     .015
                    HNCO       G   5.54239E-05    .000     .000
                    NH2        G   5.31339E-08    .000     .000
                    CHO        G   1.72173E-06    .000     .000
                    CH2O       G   3.31848E-04    .001     .001
                    CO2H2      G   2.24399E-05    .000     .000
                    CH3        G   2.95826E-05    .000     .000
                    C2H2       G   5.42597E-05    .000     .000
                    KCN        G   2.06624E-02    .052     .135
                    KH         G   4.71351E-05    .000     .000
                    KOH        G   1.54748E-02    .039     .087
```

KO	G	1.59504E-10	.000	.000
K2	G	8.90130E-07	.000	.000
K2O2H2	G	4.51224E-05	.000	.001
C	s	3.98200E+00	9.997	4.783
K2CO3	l	1.39663E+00	3.506	19.302

Condensed products, which were considered but are not present at 1466. K:

KCN	l	KOH	l

REACTION PRODUCTS AT 298. K (Freeze-out temperature 1466. K)

NAME		MOLE NUMBER	MOLE%	WGT.%
C	G	1.69960E-18	.000	.000
O	G	1.25392E-13	.000	.000
N	G	3.65764E-14	.000	.000
H	G	2.00714E-05	.000	.000
K	G	0.00000E+00	.000	.000
CO2	G	8.47182E-01	2.127	3.728
H2O	L	8.93174E-01	2.242	1.609
N2	G	5.65135E+00	14.188	15.831
CO	G	1.86008E+01	46.699	52.101
H2	G	7.92087E+00	19.886	1.597
OH	G	5.79074E-08	.000	.000
NO	G	5.29406E-10	.000	.000
O2	G	6.48509E-15	.000	.000
NH3	G	1.00470E-02	.025	.017
CH4	G	4.81324E-01	1.208	.772
HCN	G	5.66046E-03	.014	.015
HNCO	G	5.54239E-05	.000	.000
NH2	G	5.31339E-08	.000	.000
CHO	G	1.72173E-06	.000	.000
CH2O	G	3.31848E-04	.001	.001
CO2H2	G	2.24399E-05	.000	.000
CH3	G	2.95826E-05	.000	.000
C2H2	G	5.42597E-05	.000	.000
KCN	G	0.00000E+00	.000	.000
KH	G	4.71351E-05	.000	.000
KOH	G	0.00000E+00	.000	.000

```
                    KO          G   1.59504E-10   .000    .000
                    K2          G   8.90130E-07   .000    .000
                    K2O2H2      G   4.51224E-05   .000    .001

                    C           s   3.98200E+00  9.997   4.783
                    K           s   5.24693E-03   .013    .021
                    KCN         s   2.06624E-02   .052    .135
                    KOH         sa  1.54748E-02   .039    .087
                    K2CO3       s   1.39663E+00  3.506  19.302

MOLE NUMBER:      39.831 MOLES/KG   GASES WITHOUT H2O: 33.518 MOLES/KG
MOLE NUMBER H2O:   .8932 MOLES/KG   GASES WITH H2O:    34.411 MOLES/KG

      GAS VOLUME WITHOUT H2O AT 25 DEGREE C:    820.0 CC/G

HEAT OF EXPLOSION:                        1372.3 J/G =   328.0 CAL/G
Heat of explosion (water gaseous):        1335.2 J/G =   319.1 CAL/G
```

B Balloon Actuator MATLAB code

```
clear all; clc;

% input parameters

%constants
R = 8.314; % J/(mol*K), Universal gas constant

% atmosphere
Patm = 1.01325*1e5; % Pa, atmospheric pressure
Tatm = 298; % K, atmospheric temperature

% combustion chamber
a = 2.5e-3; % m, membrane radius
hc = 0.75e-3; % m, chamber height
Vc = pi * a^2 * hc; % m^3, chamber volume

% membrane
e0 = 90.e-6; % m, initial membrane thickness
C = [1859;102.2;8.329]*1.e2; % Pa, Yeoh hyperelastic model coefficients
sig0 = 994.2e2; % Pa, intrinsic stess
I1 = @(l,h) 2*l(h).^2+l(h).^(-4); % (-), first tensor invariant
sig = @(l,h) (l(h).^2 - l(h).^(-4)).*( 2*C(1) + 4*C(2)*(I1(l,h)-3) +
6*C(3)*(I1(l,h)-3).^2 ); % Pa, Yeoh model

%------------------------------------------------------------------------%
% State 1 (Initial Condition; instantaneous explosion)
%------------------------------------------------------------------------%

mf = 312e-9; % kg, fuel mass
```

```
Vi = Vc;
Pi = 90.85e5; % Pa, initial pressure (combustion products, from ICT)
kf = 1.3023;  % (-), ratio of specific heats (combustion products, from ICT)

%-------------------------------------------------------------------------%
% State 2 (inflated, hot)
%-------------------------------------------------------------------------%

r = @(h) 0.5*(a^2+h.^2)./h; % m, balloon radius
V = @(h) Vc + pi*h/6.*(3*a^2 + h.^2); % m^3, total volume
%membrane (h<a)
t = @(h) asin(a./r(h)); % rad, theta
l = @(h) t(h).*r(h)/a; % (-), stretch (lambda)
fh = @(h) ( Patm + 2*e0./(r(h).*l(h).^2).*(sig(l,h) - sig0)
- Pi.*( Vi./V(h) ).^kf ); % test equation
[hh,error] = Bisection(fh,eps,a,1.e-6,100); % solve using bisection algorithm
if isnan(hh) == 1 % if bisection does not converge, use h>a
    'balloon radius > opening radius' %#ok<NOPTS>
    t = @(h) pi-asin(a./r(h)); % m, balloon radius
    l = @(h) t(h).*r(h)/a; % (-), stretch (lambda)
    fh = @(h) ( Patm + 2*e0./(r(h).*l(h).^2).*(sig(l,h) - sig0)
     - Pi.*( Vi./V(h) ).^kf );
    [hh,error] = Bisection(fh,a,1,1.e-6,100); % solve using bisection algorithm
end

%-------------------------------------------------------------------------%
% State 3 (inflated, room Temperature)
%-------------------------------------------------------------------------%

%mixture
ngencool = 34.411; % mol/kg, # moles of gas generated (room temperature, from ICT)
nf = mf * ngencool; % mol, number of moles of gas (products)

%membrane (h<a)
t = @(h) asin(a./r(h)); % rad, theta
l = @(h) t(h).*r(h)/a; % (-), stretch (lambda)
fc = @(h) ( Patm + 2*e0./(r(h).*l(h).^2).*(sig(l,h) - sig0)
- nf*R*Tatm./V(h) );
[hc,error] = Bisection(fc,eps,a,1.e-6,100); % solve using bisection algorithm
if isnan(hc) == 1 % if bisection does not converge, use h>a
    'balloon radius > opening radius' %#ok<NOPTS>
    t = @(h) pi-asin(a./r(h)); % rad, theta
```

```
    l = @(h) t(h).*r(h)/a; % (-), stretch (lambda)
    fc = @(h) ( Patm + 2*e0./(r(h).*l(h).^2).*(sig(l,h) - sig0)
     - nf*R*Tatm./V(h) );
    [hc,error] = Bisection(fc,a,1,1.e-6,100); % solve using bisection algorithm
end
```

C Bisection Algorithm

```
function [xs,error] = Bisection(f,a,b,tol,imax)
% This function takes as inputs: a fixed point iteration function, f(x),
% and a lower and upper bound to the fixed point, a and b, and a tolerance,
% tol. The fixed point iteration function is assumed to be input as an
% inline function. This function will calculate and return the fixed point,
% xs, that makes the expression f(xs) = 0 true to within the desired
% tolerance, tol.

error = false;

fa = f(a);
fb = f(b);

if (fa*fb > 0)
    'Bisection: initial guesses do not bound fixed point'
    error = true;
    c = NaN;
    xs = c;
else
    for i = 1:imax   % Performs large, but finite, number of iterations. This
        % is to prevent infinite loops in the event that the
        % method fails to converge.

        c = (a + b)/2;
        fc = f(c);

        if (abs(fc) < tol)
            xs = c;
            break
```

```
        end

        if i == imax
            'Bisection: max. number of iterations reached'
            xs = NaN;
            error = true;
            break
        end

        if (fa*fc < 0)
            b = c;
            fb = fc;
        else
            a = c;
            fa = fc;
        end
    end
end
```

Bibliography

[1] C. Rossi and D. Estève, "Micropyrotechnics, a new technology for making energetic microsystems: review and prospective," *Sensors and Actuators A: Physical*, vol. 120, no. 2, pp. 297 – 310, 2005.

[2] C. Rossi, D. Briand, M. Dumonteuil, T. Camps, P. Q. Pham, and N. F. de Rooij, "Matrix of 10×10 addressed solid propellant microthrusters: review of the technologies," *Sensors and Actuators A: Physical*, vol. 126, no. 1, pp. 241 – 252, 2006.

[3] K. L. Zhang, S. K. Chou, and S. S. Ang, "Development of a solid propellant microthruster with chamber and nozzle etched on a wafer surface," *Journal of Micromechanics and Microengineering*, vol. 14, no. 6, p. 785, 2004.

[4] "Micropyros: development of an emerging technology based on micropyrotechnics. applicative exploration of energetic microsystems," Final Report IST-1999-29047, Project Coordinator: CNRS-LAAS, November 2003.

[5] C. Rossi, B. Larangot, D. Lagrange, and A. Chaalane, "Final characterizations of MEMS-based pyrotechnical microthrusters," *Sensors and Actuators A: Physical*, vol. 121, no. 2, pp. 508 – 514, 2005.

[6] H. Ebisuzaki and K. Takahashi, "Design and testing of multi-pulse MEMS solid rocket," in *Proceedings of the 3rd International Workshop on Micro and Nanotechnology for Power Generation and Energy Conversion Applications*, (Makuhari, Japan), pp. 149 – 152, December 2003.

[7] S. Tanaka, R. Hosokawa, S. ichiro Tokudome, K. Hori, H. Saito, M. Watanabe, and M. Esashi, "MEMS-based solid propellant rocket array thruster," *Transactions of the Japan Society for Aeronautical and Space Sciences*, vol. 46, no. 151, pp. 47–51, 2003.

[8] S. Tanaka, K. Kondo, H. Habu, A. Itoh, M. Watanabe, K. Hori, and M. Esashi, "Test of B/Ti multilayer reactive igniters for a micro solid rocket array thruster," *Sensors and Actuators A: Physical*, vol. 144, no. 2, pp. 361 – 366, 2008.

[9] H. H. DiBiaso, B. A. English, and M. G. Allen, "Solid-phase conductive fuels for chemical microactuators," *Sensors and Actuators A: Physical*, vol. 111, no. 2 – 3, pp. 260 – 266, 2004.

[10] C. Rossi, K. Zhang, D. Esteve, P. Alphonse, P. Tailhades, and C. Vahlas, "Nanoenergetic materials for MEMS: a review," *Journal of Microelectromechanical Systems*, vol. 16, no. 4, pp. 919 –931, 2007.

[11] D. Briand, "Solid propellant and igniting technologies for space micro-propulsion modules," Final Report EPFL Space Center Project # 009/2005, Project Coordinator: IMT, Université de Neuchâtel, January 2008.

[12] C. Rossi, D. Estève, and C. Mingués, "Pyrotechnic actuator: a new generation of Si integrated actuator," *Sensors and Actuators A: Physical*, vol. 74, no. 1 – 3, pp. 211 – 215, 1999.

[13] C. Rossi, D. Estève, P. Temple-Boyer, and G. Delannoy, "Realization, characterization of micro pyrotechnic actuators and FEM modelling of the combustion ignition," *Sensors and Actuators A: Physical*, vol. 70, no. 1 – 2, pp. 141 – 147, 1998.

[14] D. H. Lewis Jr., S. W. Janson, R. B. Cohen, and E. K. Antonsson, "Digital micropropulsion," *Sensors and Actuators A: Physical*, vol. 80, no. 2, pp. 143 – 154, 2000.

[15] C. Rossi, B. Larangot, P.-Q. Pham, D. Briand, N. de Rooij, M. Puig-Vidal, and J. Samitier, "Solid propellant microthrusters on silicon: design, modeling, fabrication, and testing," *Journal of Microelectromechanical Systems*, vol. 15, no. 6, pp. 1805 –1815, 2006.

[16] D. Briand, P. Q. Pham, and N. F. de Rooij, "Reliability of freestanding polysilicon microheaters to be used as igniters in solid propellant microthrusters," *Sensors and Actuators A: Physical*, vol. 135, no. 2, pp. 329 – 336, 2007.

[17] J. Lee, K. Kim, and S. Kwon, "Design, fabrication, and testing of MEMS solid propellant thruster array chip on glass wafer," *Sensors and Actuators A: Physical*, vol. 157, no. 1, pp. 126 – 134, 2010.

[18] D. Teasdale, V. Milanovic, P. Chang, and K. S. J. Pister, "Microrockets for smart dust," *Smart Materials and Structures*, vol. 10, no. 6, p. 1145, 2001.

[19] D. Briand, L. Guillot, U. Bley, S. Danninger, V. Gass, and N. F. de Rooij, "Digital microthrusters with simplified architecture and reliable ignition and combustion," in *Proceedings of the 3rd International Workshop on Micro and Nanotechnology for Power Generation and Energy Conversion Applications*, (Sendai, Japan), November 2008.

[20] P. Pennarun, C. Rossi, D. Estève, and D. Bourrier, "Design, fabrication and characterization of a MEMS safe pyrotechnical igniter integrating arming, disarming and sterilization functions," *Journal of Micromechanics and Microengineering*, vol. 16, no. 1, p. 92, 2006.

[21] P. Pennarun, C. Rossi, D. Estève, and R.-D. Colin, "Single use, robust, MEMS based electro-thermal microswitches for redundancy and system reconfiguration," *Sensors and Actuators A: Physical*, vol. 136, no. 1, pp. 273 – 281, 2007.

[22] H. Pezous, C. Rossi, M. Sanchez, F. Mathieu, X. Dollat, S. Charlot, L. Salvagnac, and V. Conédéra, "Integration of a MEMS based safe arm and fire device," *Sensors and Actuators A: Physical*, vol. 159, no. 2, pp. 157 – 167, 2010.

[23] G. A. A. Rodríguez, S. Suhard, C. Rossi, D. Estève, P. Fau, S. Sabo-Etienne, A. F. Mingotaud, M. Mauzac, and B. Chaudret, "A microactuator based on the decomposition of an energetic material for disposable lab-on-chip applications: fabrication and test," *Journal of Micromechanics and Microengineering*, vol. 19, no. 1, p. 015006, 2009.

[24] C. Rossi, T. D. Conto, D. Estève, and B. Larangot, "Design, fabrication and modelling of MEMS-based microthrusters for space application," *Smart Materials and Structures*, vol. 10, no. 6, p. 1156, 2001.

[25] C. Rossi, S. Orieux, B. Larangot, T. D. Conto, and D. Estève, "Design, fabrication and modeling of solid propellant microrocket-application to micropropulsion," *Sensors and Actuators A: Physical*, vol. 99, no. 1 – 2, pp. 125 – 133, 2002.

[26] A. Chaalane, C. Rossi, and D. Estève, "The formulation and testing of new solid propellant mixture (DB + x % BP) for a new MEMS-based microthruster," *Sensors and Actuators A: Physical*, vol. 138, no. 1, pp. 161 – 166, 2007.

[27] K. Zhang, S. Chou, and S. Ang, "MEMS-based solid propellant microthruster design, simulation, fabrication, and testing," *Journal of Microelectromechanical Systems*, vol. 13, no. 2, pp. 165 – 175, 2004.

[28] K. L. Zhang, S. K. Chou, and S. S. Ang, "Development of a low-temperature co-fired ceramic solid propellant microthruster," *Journal of Micromechanics and Microengineering*, vol. 15, no. 5, p. 944, 2005.

[29] K. Zhang, S. Chou, S. Ang, and X. Tang, "A MEMS-based solid propellant microthruster with Au/Ti igniter," *Sensors and Actuators A: Physical*, vol. 122, no. 1, pp. 113 – 123, 2005.

[30] K. Zhang, S. K. Chou, and S. S. Ang, "Investigation on the ignition of a MEMS solid propellant microthruster before propellant combustion," *Journal of Micromechanics and Microengineering*, vol. 17, no. 2, p. 322, 2007.

[31] D. Briand, P. Dubois, L.-E. Bonjour, L. Guillot, U. Bley, S. Danninger, S. Rosset, H. Shea, and N. F. de Rooij, "Large deformation balloon micro-actuator based on pyrotechnics on chip," in *2008 IEEE 21st International Conference on Micro Electro Mechanical Systems (MEMS 2008)*, pp. 535 –538, jan. 2008.

[32] D. A. de Koninck, D. Briand, L. Guillot, U. Bley, V. Gass, and N. F. de Rooij, "Ignition and combustion behavior in solid propellant microsystems using Joule-effect igniters," *Journal of Microelectromechanical Systems*, vol. 20, no. 6, pp. 1259 –1268, 2011.

[33] D. A. de Koninck, D. Briand, and N. F. de Rooij, "A shadow-mask evaporated pyroMEMS igniter," *Journal of Micromechanics and Microengineering*, vol. 21, no. 10, p. 104013, 2011.

[34] D. A. de Koninck, F. M. Lopez, D. Briand, and N. F. de Rooij, "Foil-level fabrication of inkjet-printed pyroMEMS balloon actuators," in *2012 IEEE 25th International Conference on Micro Electro Mechanical Systems (MEMS 2012)*, pp. 64 –67, 29 2012-feb. 2 2012.

[35] D. W. Youngner, S. T. Lu, E. Choueiri, J. B. Neidert, R. E. Black III, K. J. Graham, D. Fahey, R. Lucus, and X. Zhu, "MEMS mega-pixel micro-thruster arrays for small satellite station-keeping," in *Proceedings of the 14^{th} Annual/USU Conference on Small Satellites*, (Logan, Utah, USA), August 2000.

[36] Y. H. Choi, S. U. Son, and S. S. Lee, "A micropump operating with chemically produced oxygen gas," *Sensors and Actuators A: Physical*, vol. 111, no. 1, pp. 8 – 13, 2004.

[37] C.-C. Hong, S. Murugesan, S. Kim, G. Beaucage, J.-W. Choi, and C. H. Ahn, "A functional on-chip pressure generator using solid chemical propellant for disposable lab-on-a-chip," *Lab Chip*, vol. 3, pp. 281–286, 2003.

[38] A. Norton and M. Minor, "Pneumatic microactuator powered by the deflagration of sodium azide," *Journal of Microelectromechanical Systems*, vol. 15, no. 2, pp. 344 – 354, 2006.

[39] X. Pi, Y. Lin, K. Wei, H. Liu, G. Wang, X. Zheng, Z. Wen, and D. Li, "A novel micro-fabricated thruster for drug release in remote controlled capsule," *Sensors and Actuators A: Physical*, vol. 159, no. 2, pp. 227 – 232, 2010.

[40] O. Vasylkiv and Y. Sakka, "Nanoexplosion synthesis of multimetal oxide ceramic nanopowders," *Nano Letters*, vol. 5, no. 12, pp. 2598–2604, 2005.

[41] O. Vasylkiv, Y. Sakka, and V. V. Skorokhod, "Nano-blast synthesis of nano-size CeO2–Gd2O3 powders," *Journal of the American Ceramic Society*, vol. 89, no. 6, pp. 1822–1826, 2006.

[42] D. S. Steward, "Miniaturization of explosive technology and microdetonics," in *Proceedings of the 21^{st} International Conference of Theoretical and Applied Mechanics (ICTAM04)*, (Varsaw, Poland), August 2004.

[43] D. Jones, P. Lightfoot, R. Fouchard, Q. Kwok, A.-M. Turcotte, and W. Ridley, "Hazard characterization of KDNBF using a variety of different techniques," *Thermochimica Acta*, vol. 384, no. 1 – 2, pp. 57 – 69, 2002.

[44] V. N. Huff, S. Gordon, and V. E. Morell, "General method and thermodynamic tables for computation of equilibrium composition and temperature of chemical compositions," Tech. Rep. NACA-Report 1037, 1951.

[45] F. J. Zeleznik and S. Gordon, "An analytical investigation of three general methods of calculating chemical equilibrium compositions," Tech. Rep. NASA-TN D-473, 1960.

[46] F. J. Zeleznik and S. Gordon, "A general IBM 704 or 7090 computer program for computation of chemical equilibrium compositions, rocket performance, and Chapman-Jouguet detonations," Tech. Rep. NASA-TN D-1454, October 1962.

[47] L. Thiery, E. Gavignet, and B. Cretin, "Two omega method for active thermocouple microscopy," *Review of Scientific Instruments*, vol. 80, no. 3, p. 034901, 2009.

[48] L. Thiery, R. Porcar, and J. Prenel, "Performance limits of microthermocouples as opto-thermal sensors," *Optics Communications*, vol. 107, no. 3 – 4, pp. 309 – 317, 1994.

[49] F. Kreith and M. S. Bohn, *Principles of Heat Transfer*. Brooks/Cole, 6^{th} ed., 2001.

[50] "Borofloat 33 thermal properties." http://www.schott.com/borofloat/english/attribute/thermic/index.html?so=schweiz&lang=german.

[51] "Upilex®-s | polyimide | ube industries, ltd." http://www.ube-scp.jp/en/products/polyimide/poly010.html.

[52] H. S. Carslaw and J. C. Jaeger, *Conduction of Heat in Solids*. Oxford University Press, 2^{nd} ed., 1959.

[53] J. Neter, W. Wasserman, and M. H. Kutner, *Applied Linear Statistical Models*. Richard D. Irwin, Inc., 2^{nd} ed., 1985.

[54] H. W. Lilliefors, "On the Kolmogorov-Smirnov test for normality with mean and variance unknown," *Journal of the American Statistical Association*, vol. 62, no. 318, pp. 399–402, 1967.

[55] I. Simon, N. Bârsan, M. Bauer, and U. Weimar, "Micromachined metal oxide gas sensors: opportunities to improve sensor performance," *Sensors and Actuators B: Chemical*, vol. 73, no. 1, pp. 1 – 26, 2001.

[56] S. Dorbolo, A. Merlen, M. Creyssels, N. Vandewalle, B. Castaing, and E. Falcon, "Effects of electromagnetic waves on the electrical properties of contacts between grains," *EPL (Europhysics Letters)*, vol. 79, no. 5, p. 54001, 2007.

[57] R. Gueye, T. Akiyama, D. Briand, and N. de Rooij, "Development of high temperature platinum TSVs," *Procedia Engineering*, vol. 25, no. 0, pp. 1513 – 1516, 2011.

[58] Y. Xia and G. M. Whitesides, "Soft lithography," *Annual Review of Materials Science*, vol. 28, no. 1, pp. 153–184, 1998.

[59] D. Johnson, A. Voigt, G. Ahrens, and W. Dai, "Thick epoxy resist sheets for MEMS manufacturing and packaging," in *2010 IEEE 23rd International Conference on Micro Electro Mechanical Systems (MEMS 2010)*, pp. 412 –415, jan. 2010.

[60] S. Sawano, K. Naka, A. Werber, H. Zappe, and S. Konishi, "Sealing method of PDMS as elastic material for MEMS," in *2008 IEEE 21st International Conference on Micro Electro Mechanical Systems (MEMS 2008).*, pp. 419 –422, jan. 2008.

[61] O. H. Yeoh, "Some forms of the strain energy function for rubber," *Rubber Chemistry and technology*, vol. 66, no. 5, pp. 754 – 771, 1993.

[62] R. L. Burden and J. D. Faires, *Numerical Analysis*. Brooks/Cole, 7^{th} ed., 2001.

[63] T. Merkel, R. Gupta, B. Turk, and B. Freeman, "Mixed-gas permeation of syngas components in poly(dimethylsiloxane) and poly(1-trimethylsilyl-1-propyne) at elevated temperatures," *Journal of Membrane Science*, vol. 191, no. 1 – 2, pp. 85 – 94, 2001.

[64] G. A. A. Rodríguez, *Conception, simulation et réalisation d'un micro actionneur à base de matériau énergétique pour l'actionnement microfluidique*. PhD thesis, Université Toulouse III—Paul Sabatier, 2008.

[65] G. A. A. Rodríguez, C. Rossi, and K. Zhang, "Multi-physics system modeling of a pneumatic micro actuator," *Sensors and Actuators A: Physical*, vol. 141, no. 2, pp. 489 – 498, 2008.

David de Koninck

Personal Information

Permanent Address: Rue Fontaine-André 6, 2000 Neuchâtel, Switzerland
Phone Numbers:
Mobile: +41.(0)76.265.95.97 • *Office:* +41.(0)32.720.54.42
E-mail: david.dekoninck@efpl.ch
Languages: Fluent in both French and English
Citizenship: Canadian
Available: September 2012

Education

Doctoral degree in Microsystems Engineering **2008-Present**
École Polytechnique Fédérale de Lausanne, Neuchâtel, Switzerland
Supervisor: Prof. Nicolaas F. de Rooij
Areas of Interest: Energy, Fluid mechanics, Thermodynamics
Thesis Title: PyroMEMS: Improved Fabrication Methods and Ignition Reliability

Master's degree in Mechanical Engineering **2006-2008**
McGill University, Montreal, Canada (CGPA: 4.0/4.0)
Co-Supervisors: Prof. Srikar Vengallatore (McGill) and Prof. Luc Fréchette (U Sherbrooke)
Thesis Title: Thermal Conductivity Measurements Using the 3-Omega Technique: Application to Power Generating Microsystems

Bachelor's degree in Mechanical Engineering – Honours Program **2002-2006**
McGill University, Montreal, Canada (CGPA: 3.79/4.0)
Aeronautics Option; Distinction; Dean's Honour List

Work Experience

Teaching assistant
- Heat and Mass Transfer (Undergrad), EPFL, Spring 2010
- Heat Transfer (Undergrad), McGill University, Fall 2007

Air Liquide International Internship Program **July-August 2006**
Centre De Recherche Claude Delorme, Paris, France
- International internship involving over 20 students from 10 different countries
- Task: state-of-the-art review of helium purification technologies to guide future R&D

Research Assistant – Aerospace Composite Materials **May-June 2006**
NRC Aerospace Manufacturing Technology Centre, Montreal, Canada
- Finite element modeling and experimental research in welding of thermoplastic composite materials

Research Assistant – Aerospace Propulsion **Summer 2005**
McGill University, Montreal, Canada
- Performed detonation tube experiments related to the pulsed detonation engine for supersonic flight

David de Koninck

Awards

NSERC – PGS: Postgraduate Scholarship (C$63,000 over 3 years) **2008-2011**
Natural Science and Engineering Research Council of Canada
FQRNT – Bourse de doctorat en recherche (C$60,000 over 3 years)
Fond québécois de la recherche sur la nature et les technologies
- Declined: Cannot hold both FQRNT and NSERC simultaneously

FQRNT – Bourse de maîtrise en recherche (C$30,000 over 2 years) **2006-2008**
NSERC – Undergraduate Student Research Award (C$4,500) **Summer 2005**
Bursary to perform summer research (Undergraduate)
Bell Canada Scholarship (C$10,000 over 4 years) **2002-2006**
Undergraduate scholarship

Technical Skills

Computer skills
- MATLAB, instrument automation (SCPI), LabVIEW.
- CFD++, Ansys, ICEM CFD, Comsol.
- Solid Works, AutoCAD.
- Origin, Adobe Illustrator and Photoshop.

Statistics skills
- Design of Experiments, Analysis of Variance (single, multiple, covariance), Regression analysis, hypothesis testing.

Extracurricular Activities

Student Aerospace Forum Organising Committee **2006-2007**
Largest student aerospace conference in Quebec
- Responsible for promotional tools for the conference, e.g., website, posters, ads
- Trimmed the promotional budget by 50% for a net savings of C$2,000

Let's Talk Science **2006-2008**
Nationwide science outreach program in Canada for children aged 6 to 16
- Gave many classroom presentations and judged numerous science fairs

Formula SAE – McGill University Chapter **2003-2005**
International Student competition to design, build and race a Formula 1 style racing car.
Positions held: Sponsorship Coordinator; Suspension Sub-team

Golden Path Tutoring Program **2003-2006**
Positions held: Vice-President, Communications; Tutor

Mountaineering/Rock Climbing
In the Swiss Alps and Canadian Rockies

David de Koninck

Scientific Publications

D A de Koninck, F Molina Lopez, D Briand, N F de Rooij, Foil-level fabrication of inkjet-printed pyroMEMS balloon actuators, *Proc. MEMS 2012* (Paris, France) January 29-February 2, 2012 (oral presentation).

D A de Koninck, D Briand, L Guillot, U Bley, V Gass, N F de Rooij, Ignition and Combustion Behavior in Solid Propellant Microsystems Using Joule-Effect Igniters, *Journal of MicroElectroMechanical Systems*, vol. 20 (2011), pp. 1259-1268.

D A de Koninck, D Briand, N F de Rooij, A shadow-mask evaporated pyroMEMS igniter, *Journal of Micromechanics and Microengineering*, vol. 21 (2011), 104013 (7pp).

D A de Koninck, D Briand, N F de Rooij, A shadow mask-evaporated topside pyroMEMS igniter, *Proc. PowerMEMS 2010* (Leuven, Belgium) December 1-3, 2010, pp. 43-46 (oral presentation).

D A de Koninck, U Bley, V Gass, D Briand, N F de Rooij, PyroMEMS igniter based on a temperature gradient: concept, fabrication and characterization, *Proc. PowerMEMS 2009* (Washington D.C., USA) December 1-4, 2009, pp. 108-111 (oral presentation).

Invited Presentations

- UCSB, Mechanical Engineering Seminar, Santa Barbara, CA, November 28th, 2011.
- EPFL, LMTS Seminar, Neuchâtel, CH, February 1st, 2008